

Bogolyubov Institute for Theoretical Physics
of the National Academy of Sciences of Ukraine

Qualifying scientific work
as a manuscript

Mykyta Klen

UDC 535.14, 530.145, 535.1

Statistical models and temporal coherence of quantum light in the turbulent atmosphere

A thesis submitted for the degree of Doctor of Philosophy

104–Physics and astronomy
Field of study: 10–Natural sciences

The thesis contains the results of original research. All uses of ideas, results, and texts by other authors are accompanied by references to the relevant source.

(signature, initials, and surname of the candidate)

Supervisor

Dr. habil. Andrii Semenov

Kyiv – 2026

Анотація

Клен М.Д. Статистичні моделі та часова когерентність квантового світла в турбулентній атмосфері.—*Кваліфікаційна наукова праця на правах рукопису. Дисертація на здобуття наукового ступеня доктора філософії за спеціальністю 104—Фізика та астрономія—Інститут теоретичної фізики ім. М.М. Боголюбова Національної академії наук України, Київ, 2026.*

Основою локальних мереж квантового зв'язку є волоконно-оптичні канали, проте вони обмежені експоненційним затуханням сигналу та стаціонарністю інфраструктури. Оптичні канали у вільному просторі пропонують гнучку альтернативу, дозволяючи створювати бездротові з'єднання між наземними станціями, а також з авіаційними платформами, що є недоступним для стаціонарних волоконних мереж. На відміну від контрольованих умов при використанні оптичного волокна, канали у вільному просторі піддаються впливу атмосферної турбулентності. Цей процес спричиняє стохастичні флуктуації показника заломлення та відповідні спотворення променя світла, що проявляється у вигляді блукання променя навколо осі поширення та сцинтиляції (флуктуацій інтенсивності). Відтак, зазначені ефекти суттєво ускладнюють опис таких каналів для квантової комунікації.

Вплив турбулентності на квантовий стан світла у квазімонохроматичній моді моделюється однією випадковою величиною — ефективністю проходження, що визначається відношенням інтенсивності, яка потрапила у апертуру приймача, до загальної інтенсивності променя світла. Таким чином, розподіл імовірності ефективності проходження (РІЕП) є ключовим для характеристики атмосферних квантових каналів у вільному просторі. Попри його фундаментальне значення, при моделюванні РІЕП зберігаються суттєві теоретичні прогалини. По-перше, не визначено чітких критеріїв застосовності наявних у літературі аналітичних моделей РІЕП. По-друге,

сучасні дослідження переважно базуються на описі ансамблю проходжень пучка світла, ігноруючи часові кореляції. Це унеможлиблює динамічну характеристику каналів, необхідну для реалізації практичних квантових протоколів в умовах турбулентності.

Для вирішення цих проблем однією з основних цілей цього дослідження є встановлення меж застосовності наявних аналітичних моделей шляхом їх порівняння з результатами чисельного моделювання. Ми також проводимо валідацію фундаментальних припущень, на яких базуються поточні моделі, з метою оцінки їхньої придатності для різних сценаріїв використання. Крім того, другий компонент цього дослідження присвячений вивченню часової залежності квантових властивостей в умовах атмосферної турбулентності. Зокрема, ми прагнемо кількісно оцінити ступінь стійкості заплутаності та неklasичності до стохастичних флуктуацій, спричинених саме цими умовами.

У цьому дослідженні застосовано чисельний метод фазових екранів, що моделює поширення світла як послідовність тонких фазових модуляторів, розділених ділянками вільного простору. Щоб уникнути статистичних похибок, властивих традиційним методам генерації фазових екранів, ми використовуємо метод розрідженого спектру, який гарантує, що згенеровані фазові екрани суворо відповідають теоретичним виразам. Додатково цей підхід дозволяє генерувати довгі фазові екрани, що дає змогу застосувати гіпотезу “замороженої” турбулентності Тейлора. Цей метод пов’язує часову еволюцію турбулентності з просторовим зміщенням, спричиненим вітром. Ми оцінюємо точність прогнозів наявних аналітичних моделей за допомогою статистики Колмогорова-Смирнова, щоб виміряти, наскільки точно передбачення аналітичних моделей узгоджуються з чисельно змодельованими даними.

В результаті, чисельне моделювання, що охоплює режими від слабкої до сильної турбулентності, продемонструвало, що інтенсивність атмосферної

турбулентності передусім визначає лише дисперсію РІЕП, не змінюючи суттєво форми розподілу. Натомість асиметрія розподілу виявляє високу варіативність та зміну знака залежно від розміру апертури приймача. Зокрема, коли розмір апертури є значно меншим за характерну ширину променя, хвіст розподілу подовжується у напрямку до вищих значень ефективності проходження (позитивна асиметрія); навпаки, збільшення апертури зміщує хвіст у бік нижчих значень ефективності проходження (негативна асиметрія). Проте більшість аналітичних моделей обмежені жорсткою поведінкою асиметрії та не здатні відтворити цей перехід, зумовлений розміром апертури.

Ми провели систематичний аналіз властивостей та обмежень наявних аналітичних моделей. Було встановлено, що відхилення центру променя не можна вважати незалежним від деформації його форми, а гіпотеза гауссового спільного розподілу для логарифмів піввісей променя є хибною. Іншою проблемою є те, що, хоча аналітичні моделі, параметризовані характеристиками променя, досить точно наближають загальну форму РІЕП, чисельне моделювання виявляє систематичне зміщення їхніх передбачень щодо моди розподілу та середнього значення. Ця розбіжність зумовлена неправильною специфікацією моделі, оскільки припущення про ідеалізовану кругову або еліптичну форму променя не дозволяє адекватно описати його реальні складні деформації. Як наслідок, такі моделі вносять систематичні похибки та демонструють гірші показники статистики Колмогорова-Смирнова порівняно з іншими підходами.

Для усунення зміщення через неправильну специфікацію моделі ми впроваджуємо метод узгодження моментів ефективності проходження, який перепараметризує моделі на основі форми променя через перші моменти ефективності проходження. Застосування цієї методики до моделі кругового променя демонструє кращі значення статистики Колмогорова-Смирнова порівняно з іншими фізично обґрунтованими моделями. Наша інша емпірична

модель на основі бета-розподілу демонструє вищу узгодженість із даними у більшості протестованих режимів, оскільки вона краще враховує варіації асиметрії, зумовлені розміром апертури.

Для опису часових кореляцій в атмосферних квантових каналах ми розробили концепцію двочасового РІЕП, яка дозволяє вийти за межі статичних описів ансамблів і характеризувати спільні розподіли ефективності проходження як функцію часового інтервалу між двома імпульсами. На цій основі ми вводимо усереднений за апертурою радіус просторової когерентності, який кількісно визначає зміщення вітру, при якому кореляції ефективності проходження спадають до $\exp(-1)$. Зокрема, визначений радіус просторової когерентності можна апроксимувати лінійною залежністю від розміру апертури приймача. Така формалізація забезпечує статистичний фундамент для кількісної оцінки часових кореляцій в атмосферних квантових каналах та аналізу стійкості квантових властивостей.

Спираючись на концепцію двочасового РІЕП, ми кількісно оцінюємо стійкість квантової заплутаності та неklasичності в атмосферних каналах. Хоча квантова заплутаність між двома імпульсами може зберігатися протягом десятків мілісекунд, ефективність квантової пам'яті залишається критичним фактором, що обмежує практичне використання квантової заплутаності в дискретних змінних у часових інтервалах тривалістю кілька мілісекунд. Крім того, показано, що протоколи адаптивної селекції з використанням яскравих класичних імпульсів для тестування ефективності проходження каналу дозволяють зберігати неklasичність протягом часових інтервалів до десятків мілісекунд між тестовим імпульсом та квантовим станом.

У підсумку зазначимо, що у цій дисертації усунуто неоднозначності щодо розуміння та опису атмосферних квантових каналів. Зокрема, встановлено, що наявні аналітичні моделі часто не здатні коректно врахувати асиметрію розподілу, залежну від розміру апертури. Це зумовлює необхідність

відмови від інтенсивності турбулентності як єдиного критерію вибору моделі. Натомість у цій роботі встановлено, що розмір апертури приймача є визначальним параметром для вибору відповідної моделі.

Хоча модель кругового променя з використанням розробленого методу узгодження моментів ефективності проходження демонструє найкращі результати серед фізично обґрунтованих моделей, необхідність чисельного інтегрування обмежує її широке практичне застосування. Відтак, емпірична модель на основі бета-розподілу є оптимальною для практичного застосування завдяки наявності аналітичного виразу в замкнутій формі та параметризації лише двома моментами ефективності проходження. Ця модель є особливо корисною для аналізу квантових протоколів, у яких сучасні методи часто не враховують флуктуації ефективності проходження, що призводить до систематичного ігнорування випадкової природи каналу та суттєвих помилок в оцінюванні характеристик. Застосування моделі бета-розподілу дозволяє подолати ці обмеження, забезпечуючи коректність аналізу захищеності в тих випадках, де ігнорування стохастичності каналу призводить до хибних результатів.

Підтверджена стійкість квантових кореляцій у реальних часових діапазонах обґрунтовує доцільність застосування методів часового кодування в мережах квантового зв'язку у вільному просторі. Водночас практична реалізація протоколів з використанням квантової заплутаності в дискретних змінних залишається обмеженою ефективністю квантової пам'яті. Це підкреслює, що хоча атмосферні канали забезпечують значні часові вікна для реалізації протоколів, повне розкриття їхнього потенціалу потребує подолання технологічних бар'єрів у зберіганні квантової інформації.

Ключові слова: Квантові канали у вільному просторі, розподіл імовірностей ефективності проходження (РІЕП), часові кореляції в каналах у вільному просторі, часове кодування, двочасовий РІЕП, просторовий

радіус когерентності, метод узгодження моментів ефективності проходження, атмосферна турбулентність, метод фазових екранів, квантова запутаність, протоколи адаптивної селекції, некласичність.

Список публікацій:

- [I] M. Klen and A. A. Semenov, "Numerical simulations of atmospheric quantum channels", [Phys. Rev. A 108, 033718 \(2023\)](#). **(Q1)**
- [II] M. Klen, D. Vasylyev, W. Vogel, and A. A. Semenov, "Time correlations in atmospheric quantum channels", [Phys. Rev. A 109, 033712 \(2024\)](#). **(Q1)**
- [III] I. Pechonkin, M. Klen, and A. A. Semenov, "Circular-beam approximation for quantum channels in a turbulent atmosphere", [Phys. Rev. A 112, 063716 \(2025\)](#). **(Q1)**
- [IV] A. Semenov, M. Klen, and I. Pechonkin, "Quantum Optics in the Turbulent Atmosphere: Fundamental Issues and Applications", in Quantum Technologies for Defence and Security II, edited by V. Fernandez, G. Sorelli, and S. Schwartz (p. 38). [Proc. SPIE 13676, 136760H-13 \(2025\)](#).

Abstract

Klen M.D. Statistical models and temporal coherence of quantum light in the turbulent atmosphere—*Qualifying research work as a manuscript. Thesis submitted for the degree of Doctor of Philosophy in specialty 104–Physics and Astronomy—Bogolyubov Institute for Theoretical Physics of the National Academy of Sciences of Ukraine, Kyiv, 2026.*

Fiber links form the foundation of local quantum communication networks. However, they are constrained by inherent signal attenuation and the rigidity of stationary infrastructure. Free-space optical links offer a scalable alternative for expanding these networks through wireless connections. Furthermore, they enable connections between moving ground-based stations and airborne platforms, which fixed fiber infrastructure cannot establish.

Unlike the controlled environment of optical fibers, free-space links are subject to atmospheric turbulence that induces stochastic fluctuations in the refractive index and distorts the propagating beam. These perturbations manifest as beam wandering from the propagation axis and intensity fluctuations known as scintillation. Consequently, these effects introduce significant complexity in characterizing the channel statistics for free-space quantum communication.

The impact of turbulence on the quantum state of light prepared in a quasi-monochromatic mode can be described by a single random variable—transmittance—defined as the ratio of the intensity captured by the receiving aperture to the total beam intensity. Thus, the probability distribution of transmittance (PDT) is central to the characterization of atmospheric quantum channels. Despite its fundamental role, significant theoretical gaps persist regarding how this variable is modeled and utilized. First, there remains no clear understanding regarding model selection among the various analytical models of the PDT. Second, current literature relies on static ensemble descriptions that neglect time correlations. This approach fails to provide the dynamic characterization required by many

practical quantum protocols in the turbulent atmosphere.

To address these challenges, one of the primary objectives of this research is to establish the range of applicability for existing analytical models by comparing their predictions against numerical simulations. We also validate the underlying assumptions of current models in order to evaluate their suitability for different scenarios. Furthermore, the second component of this study investigates the temporal dependence of quantum properties in atmospheric turbulence. Specifically, we seek to quantify the resilience of entanglement and nonclassicality against stochastic fluctuations induced in these conditions.

This study employs a numerical approach to simulate atmospheric channels based on the phase screen method, modeling the propagation path as a sequence of thin, phase-modulated layers separated by free-space vacuum segments. To address statistical discrepancies inherent in traditional generation techniques, we utilize the sparse spectrum approach that ensures generated phase screens strictly align with theoretical requirements. Additionally, this approach facilitates the generation of extended phase screens, enabling the application of the Taylor frozen turbulence hypothesis. This method links the time-evolution of atmospheric transmittance to wind-driven displacements. We assess the predictive accuracy of existing analytical models against this data using the Kolmogorov-Smirnov statistic to measure how closely the analytical model predictions match the simulated data.

Numerical simulations spanning weak-to-strong turbulence regimes demonstrated that atmospheric turbulence strength primarily governs the variance of the PDT without significantly altering its fundamental shape. Conversely, the skewness—representing the distribution’s asymmetry—exhibits high variability and sign reversals contingent upon the receiving aperture size. Specifically, when the aperture is much smaller than the beam width, the distribution tail extends toward higher transmittance values (positive skewness); in contrast, larger apertures shift the tail toward lower transmittance values (negative skewness). However, most

analytical models are constrained by rigid skewness behaviour and fail to capture this aperture-driven transition.

We systematically analyzed the properties and limitations of existing analytical models. We identified that the beam-center cannot be considered independent of shape deformation, nor does the Gaussian joint distribution hypothesis hold for the logarithms of the beam semi-axes. Another issue is that, although analytical models parameterized by beam shape moments accurately approximate the overall PDT shape, numerical simulations reveal a systematic shift in their predicted mode and mean values. This discrepancy arises due to a model misspecification bias, as idealized circular or elliptical beam shapes cannot fully describe the beam shape deformations. Consequently, such models introduce systematic errors and exhibit inferior Kolmogorov-Smirnov statistics compared to other models.

To eliminate the model misspecification bias, we introduce the transmittance-moments-matching technique, which reparametrizes beam-shape based models in terms of first transmittance moments. The circular beam model using this technique shows better Kolmogorov-Smirnov statistic values compared to other physics-based models. Our other empirical Beta-distribution model shows superior performance across the majority of tested regimes because it better accounts for aperture-driven skewness variations.

To describe time correlations in atmospheric quantum channels, we develop a two-time PDT framework that moves beyond static ensemble descriptions to characterize joint transmittance distributions as a function of the time separation between two pulses. Building on this, we introduce an aperture-averaged spatial coherence radius which quantifies the wind-driven displacement at which transmittance correlations decay to $\exp(-1)$. Specifically, the defined coherence radius exhibits a linear scaling behavior relative to the receiving aperture size. This formalization provides a statistical foundation for quantifying temporal correlations in atmospheric quantum channels and analysing the resilience of quantum properties.

Building upon the two-time PDT, we quantify the resilience of entanglement and nonclassicality in atmospheric channels. While entanglement between two pulses persists for time separations up to tens of milliseconds, quantum memory efficiency currently restricts practical discrete-variable entanglement to several milliseconds. Furthermore, adaptive selection protocols utilizing bright classical pulses to probe channel transmittance are established as a practical tool capable of preserving nonclassicality within tens of millisecond time intervals between the probe pulse and the quantum state.

In conclusion, this thesis resolves ambiguities regarding the understanding and characterization of atmospheric quantum channels. Specifically, existing analytical models often fail to reflect the aperture-dependent asymmetry observed in actual distributions. This necessitates a departure from using turbulence strength as the primary selection criterion, as this is insufficient for accurate modeling. Instead, this work establishes the size of the receiving aperture as the governing parameter for selecting the appropriate model.

While the circular-beam model with the developed transmittance-moments-matching approach demonstrates superior performance among physics-based models, its reliance on numerical integration limits broad application. Consequently, the empirical Beta-distribution model emerges as the superior choice for practical implementation, providing a closed-form analytical expression parameterized by only two moments. This capability is particularly vital for quantum protocol analysis, where current methods often rely on constant-transmittance approximations that systematically ignore the random nature of atmospheric channels and introduce significant estimation errors. Utilizing the Beta-distribution model directly addresses this limitation, effectively eliminating potential loopholes in performance analysis by demonstrating robust validity across the majority of parameter regimes.

The analyzed resilience of quantum correlations over practical temporal

windows renders time-bin encoding strategies feasible for free-space quantum networking. However, the practical realization of discrete variable entanglement protocols remains constrained by quantum memory efficiency. This highlights that while atmospheric channels support practical timescales, unlocking their full potential requires addressing storage limitations inherent in current quantum hardware.

Keywords: Free-space quantum channels, probability distribution of transmittance (PDT), temporal correlations in free-space channels, time-bin encoding, two-time PDT, spatial coherence radius, transmittance-moment matching, atmospheric turbulence, phase-screen method, strong fluctuation regime, quantum entanglement, adaptive selection protocols, nonclassicality.

List of publications:

- [I] M. Klen and A. A. Semenov, "Numerical simulations of atmospheric quantum channels", [Phys. Rev. A 108, 033718 \(2023\)](#). (Q1)
- [II] M. Klen, D. Vasylyev, W. Vogel, and A. A. Semenov, "Time correlations in atmospheric quantum channels", [Phys. Rev. A 109, 033712 \(2024\)](#). (Q1)
- [III] I. Pechonkin, M. Klen, and A. A. Semenov, "Circular-beam approximation for quantum channels in a turbulent atmosphere", [Phys. Rev. A 112, 063716 \(2025\)](#). (Q1)
- [IV] A. Semenov, M. Klen, and I. Pechonkin, "Quantum Optics in the Turbulent Atmosphere: Fundamental Issues and Applications", in *Quantum Technologies for Defence and Security II*, edited by V. Fernandez, G. Sorelli, and S. Schwartz (p. 38). [Proc. SPIE 13676, 136760H-13 \(2025\)](#).

Table of Contents

АНОТАЦІЯ	1
Abstract	7
Introduction	14
1 Background	23
1.1 Quantum Optics	23
1.2 Quantum light in atmosphere	25
1.2.1 Experimental contributions	25
1.2.2 Foundation of classical theory of light in atmosphere	26
1.2.3 Probability density function of the irradiance	27
1.2.4 Probability density function of photocounting	28
1.3 Quantum channels in turbulent atmosphere	29
1.3.1 Analytical models of PDT	30
1.4 Numerical simulation framework	32
1.4.1 Preliminaries on random functions theory	32
1.4.2 Theory of turbulent atmosphere	36
1.4.3 Light beam propagation in inhomogeneous media	41
1.4.4 Phase screens method	46
1.4.5 Verification	56
2 Validation of analytical models	59
2.1 Results and discussion	61
2.1.1 Weak channel	61
2.1.2 Moderate channel	65
2.1.3 Strong channel	68
2.1.4 Summary	70
3 Statistical properties of the beam shape parameters	74
3.1 Distribution of the beam-centroid position	74

3.1.1	Weak turbulence channel	75
3.1.2	Moderate turbulence channel	76
3.1.3	Strong turbulence channel	77
3.2	Quantifying the contribution of beam wandering to the PDT . . .	78
3.3	Beam-wandering and beam-shape correlations	81
3.4	Distribution of the beam semi-axes	85
4	Moment matching for the Circular-beam model	89
4.1	Introduction	89
4.2	The model	90
4.3	Validation	94
4.4	Summary	96
5	Time correlations in Atmospheric Quantum Channels	98
5.1	Two-time PDT	98
5.2	Results	102
5.2.1	Two-time PDT	102
5.2.2	Spatial coherence radius	104
5.2.3	Conditional PDT	106
5.3	Summary	107
6	Applications	109
6.1	Gaussian entanglement between pulses	110
6.2	Discrete-variable entanglement between pulses	115
6.3	Threshold-based selection for nonclassical states	120
6.3.1	Amplitude-squeezed coherent state with adaptive selection	121
6.4	Summary	124
	Conclusions	126
	Bibliography	129
	Appendix A. List of publications, conferences and scientific meetings	142

Introduction

Relevance and motivation. Free-space quantum channels are a core element of long distance quantum communication. Optical fibers form the backbone of local and regional networks. Global scale communication, however, requires satellite-to-ground links, where propagation occurs predominantly in vacuum with near zero absorption. Several other quantum communication tasks also rely on free-space propagation, including links with moving platforms and mobile ground stations. In all such scenarios, atmospheric propagation is unavoidable at least over part of the link.

Atmospheric turbulence constitutes a dominant obstacle in these channels. Its effect arises from stochastic fluctuations of the atmospheric refractive index, which induce random variations of the received optical signal. The statistical properties of the optical field amplitude after atmospheric propagation have been studied extensively. Well established concepts describe beam wandering, beam spreading, scintillation, and speckle formation. These descriptions capture the spatial structure of the optical field at the receiver plane but do not directly address the quantities most relevant for quantum communication.

For practical quantum communication, the relevant quantity is the channel transmittance. It is defined as the optical intensity integrated over the receiver aperture and normalized to the emitted intensity. Transmittance is the central random variable that determines the quantum state of a quasi-monochromatic light mode after propagation through the atmosphere. Therefore, an accurate characterization of the PDT is required for the description of quantum-state propagation in free space.

Despite its importance, transmittance has received less systematic treatment than field amplitude statistics. Existing analytical models of the PDT are derived either from field statistics at a fixed spatial point or from phenomenological descriptions of first order beam shape parameters at the aperture plane. However, the applicability range of these models remains unclear. Several distributions have

been validated by fitting experimental data, but this approach does not establish clear criteria for model selection. Without a clear understanding of their domain of validity, the predictive power of these models is limited.

A further conceptual gap arises from the implicit assumption of statistical independence between pulses in the standard PDT framework. The PDT provides an ensemble description of a single propagation event and treats successive pulses independently. This assumption holds only when the time separation between pulses exceeds the atmospheric correlation time. In modern high repetition rate quantum communication systems, consecutive pulses propagate through strongly correlated turbulence. In this regime, temporal correlations become significant and must be explicitly accounted for. Addressing this limitation is essential for realistic modeling of high rate atmospheric quantum channels.

Research purpose and objectives. The purpose of this work is to establish a comprehensive framework for the accurate characterization of atmospheric quantum channels by advancing the modeling of transmittance statistics and temporal correlations in order to determine the quantum properties of light propagating through a turbulent atmosphere. To achieve this purpose, the following objectives are formulated:

- Develop a robust numerical model of atmospheric quantum channels that enables accurate spatial and temporal sampling of channel transmittance.
- Systematically validate existing analytical PDT models over a wide range of turbulence regimes, including weak, moderate, and strong turbulence, and identify their domains of applicability.
- Investigate the statistical properties of beam-shape parameters in order to test the unverified assumptions underlying physically motivated models.
- Based on the results of the preceding analyses, develop improved analytical models of atmospheric quantum channels.

- Analyze and quantify temporal correlations of transmittance fluctuations.
- Evaluate quantum properties in turbulent media under realistic conditions, including continuous-variable and discrete-variable entanglement between temporally separated pulses, as well as the efficiency of adaptive real time selection techniques for preserving optical nonclassicality.

Research methods. An analytical description of atmospheric quantum channels is complicated by the complexity of the underlying theoretical framework. Closed form treatments rely on strong assumptions and do not capture the full statistical variability induced by turbulence. In this work, the analysis is performed using numerical simulations. The numerical framework is built around the sparse-spectrum approach of the phase-screen method applied with the modified von Kármán turbulence spectrum.

Standard numerical approaches based on fast Fourier transforms with subharmonic corrections suffer from low frequency undersampling and rigid grid constraints. These effects lead to biased channel statistics and distorted transmittance distributions. The sparse-spectrum model avoids these limitations through random sampling of spectral components within a logarithmic spectral domain. This approach eliminates the limitations of a fixed grid, produces correct low frequency behavior, and provides an accurate representation of turbulence.

One of the objectives of this study is to determine the applicability range of analytical channel models. For this purpose, the Kolmogorov-Smirnov statistic is used to quantify the statistical distance between model cumulative distributions and empirical distributions obtained from simulations. This comparative analysis allows for an identification of where the analytical models fail to capture the variability induced by atmospheric turbulence.

The temporal dynamics are modeled using Taylor’s frozen turbulence hypothesis, which assumes that refractive index fluctuations are transported by

transverse wind while remaining structurally unchanged. By combining this hypothesis with a sparse-spectrum approach, we can generate arbitrarily long phase screens to simulate the temporal evolution of the channel. This enables the consistent simulation of successive optical pulses as they propagate through the turbulent channel.

The numerical framework is applied to analyze the survival of quantum correlations and nonclassicality in the turbulent atmosphere. For continuous variable states, Gaussian entanglement is certified using the Simon inseparability criterion. Discrete variable entanglement is quantified by the Bell parameter in the Clauser-Horne-Shimony-Holt formulation. Nonclassical photon statistics are characterized by the Mandel Q-parameter for ideal photodetection. For the arrays of click on-off detectors, the Binomial Q parameter is used with the convex-geometry approach in regimes where standard photocounting criteria become inconclusive. Collectively, these metrics allow for a direct assessment of entanglement and nonclassical features in atmospheric quantum channels.

Scientific novelty of the results.

- *Systematic validation of analytical PDT models* was performed by benchmarking them against the results of numerical simulations. Results show that common assumptions, such as the validity of the lognormal model in strong turbulence and the validity of the beam-wandering model in weak turbulence, are incomplete.

- *Receiver aperture as the dominant parameter shaping transmittance* was demonstrated by analyzing the ratio between the aperture radius and the beam size. Small apertures yield PDTs skewed positively near zero, while larger apertures produce negative skewness. These findings highlight the importance of accurately predicting the third moment of transmittance and explain why models with positive skew, such as the truncated lognormal, perform better for small apertures, whereas

beam-shape based models capture the negative skew for large apertures.

- *Misspecification bias in physically motivated models* arises when models are parametrized using beam-shape moments rather than transmittance moments. In this case, the resulting PDT exhibits a pronounced shift relative to numerical data, which can compromise quantum protocols that depend on the precise mean and variance of transmittance.

- *Validation of statistical assumptions in beam-shape models* shows that while beam-centroid displacement is accurately Gaussian, it is not independent of beam deformations, particularly under strong turbulence. Logarithms of beam semi-axes are not jointly Gaussian as assumed in the elliptic-beam model, exhibiting strong suppression along the diagonal. These results indicate that more advanced statistical descriptions are required for precise transmittance distribution modelling.

- *Transmittance-moment matching method for beam-shape models* is introduced to eliminate the model misspecification bias. The parameters of the beam-shape models are expressed through transmittance moments rather than beam-shape parameters. This method preserves physical interpretability while ensuring consistency with the key statistical characteristics of the quantum channel. The resulting analytical model outperforms all previous beam-shape based approaches.

- *Two-Time PDT framework* generalizes the channel description from static ensemble averages by introducing the joint transmittance distribution at two times. This captures temporal correlations between pulses in high-repetition-rate systems and enables analysis of time-bin encoded protocols.

- *Introduction of aperture-averaged spatial coherence radius ρ_0* defines the wind-driven displacement at which transmittance correlations decay to e^{-1} . It scales approximately linearly with the aperture radius, quantifying temporal coherence and guiding optimal pulse separation or repetition rates for quantum protocols.

- *Quantification of temporal resources in atmospheric channels for quantum protocols* demonstrates that entanglement can be preserved over millisecond

timescales. The main limiting factor for discrete-variable entanglement is quantum memory; under ideal memory conditions, preservation extends to tens of milliseconds. Adaptive selection using bright classical pulses is analyzed under realistic constraints, providing quantitative bounds for exploiting temporal correlations to maintain nonclassicality. These results indicate substantial potential to enlarge the effective Hilbert-space dimensionality.

Practical significance. A central difficulty in current practice is the absence of clear criteria for selecting analytical models of the PDT in a given scenario. Here, we resolve this ambiguity by establishing a correspondence between the ratio of the receiver aperture radius to the averaged beam radius and the analytical models that perform accurately in the corresponding regime. For instance, small apertures lead to truncated lognormal statistics, while larger apertures produce negatively skewed distributions consistent with beam shape based models. This criterion allows for the systematic selection of models and replaces previous flawed selection heuristics.

The empirical analytical model based on the Beta distribution provides a flexible, closed-form approach to PDT modeling. By utilizing only two moments of transmittance for parameterization, it reproduces the main classes of observed transmittance statistics and demonstrates robust validity across the majority of parameter regimes. Its parameters can be efficiently estimated from numerical or experimental data, making the model suitable for real-time evaluation of quantum protocols under realistic atmospheric conditions.

Existing descriptions of atmospheric quantum channels treat quantum pulses as statistically independent ensembles. This assumption breaks down in modern systems operating at high-repetition rate, where successive pulses propagate through strongly correlated turbulence. This thesis introduces the two-time PDT to explicitly describe the joint statistics of two consecutive pulses. We also introduce the aperture-averaged spatial coherence radius which provides a practical criterion

for choosing pulse repetition rates that either exploit or suppress correlation effects, depending on the protocol objective. This extension represents a necessary step from idealized single pulse models toward realistic high rate quantum communication.

Numerical simulations show that atmospheric turbulence allows the preservation of entanglement over time scales of several milliseconds. With further development of quantum memories, storage times of tens of milliseconds are expected for discrete variable entanglement. Taken together, these results demonstrate the feasibility of correlation aware strategies, including adaptive selection techniques, for preserving nonclassicality in realistic atmospheric channels.

Statement of authorship.¹ The research presented in the papers [I] and [II] was primarily conducted by the candidate. The scientific advisor, A. A. Semenov, provided the core conceptual ideas, research direction, and supervisory control throughout the project. The co-authors—specifically D. Vasylyev and W. Vogel—provided assistance through enlightening discussions that helped refine the theoretical results and the interpretation of simulated data.

In the paper [III] the author’s individual contributions to the research included providing the numerical framework utilized for beam shape distribution analysis and performing the extensive model validation. Additionally, I proposed the moment matching technique to eliminate the model-misspecification bias found in previous models. In the paper [IV] the author’s individual contribution consisted of conducting numerical modeling, analyzing the obtained data, and preparing representative visualization materials, which constituted the basis of the presented materials.

¹Throughout this thesis, author’s own publications are cited using Roman numerals (see the list on page 142), while all other references are cited using Arabic numerals and listed in the bibliography list (page 129).

List of publications.

- [I] M. Klen and A. A. Semenov, "Numerical simulations of atmospheric quantum channels", [Phys. Rev. A 108, 033718 \(2023\)](#). (Q1)
- [II] M. Klen, D. Vasylyev, W. Vogel, and A. A. Semenov, "Time correlations in atmospheric quantum channels", [Phys. Rev. A 109, 033712 \(2024\)](#). (Q1)
- [III] I. Pechonkin, M. Klen, and A. A. Semenov, "Circular-beam approximation for quantum channels in a turbulent atmosphere", [Phys. Rev. A 112, 063716 \(2025\)](#). (Q1)
- [IV] A. Semenov, M. Klen, and I. Pechonkin, "Quantum Optics in the Turbulent Atmosphere: Fundamental Issues and Applications", in Quantum Technologies for Defence and Security II, edited by V. Fernandez, G. Sorelli, and S. Schwartz (p. 38). [Proc. SPIE 13676, 136760H-13 \(2025\)](#).

Conferences and scientific meetings. The thesis results were presented at seminars of the Bogolyubov Institute for Theoretical Physics of the National Academy of Sciences of Ukraine, as well as at Ukrainian and international conferences, in particular:

1. M. Klen and A. A. Semenov, "Free-space quantum channels: Numerical simulations", US-Ukraine Quantum Forum 2023, August 28-31, 2023
2. M. Klen, "Quantum light in atmospheric turbulence", 25th Symposium on photonics and optics SPO 2024, Kyiv, (Ukraine), November 8, 2024
3. M. Klen, "Numerical simulations in free-space quantum channels", Poster session at Quantum 2025: From Foundations of Quantum Mechanics to Quantum Information and Quantum Metrology & Sensing, Turin, (Italy), May 18-24, 2025
4. A. Semenov, M. Klen, I. Pechonkin, "Quantum optics in the turbulent atmosphere: fundamental issues and applications": invited talk at the SPIE Sensors+Imaging Meeting. Quantum Technologies for Defense and Security II. Madrid, Spain. September 15–18, 2025.

Structure and scope of the thesis. The thesis consists of an introduction, six chapters, conclusions, and a list of references (136 references). The total volume of the work is 142 pages, including 88 equations, 9 tables and 31 figures.

Connection with research programs and grants. The thesis was completed at the Bogolyubov Institute for Theoretical Physics of the National Academy of Sciences of Ukraine. It is related to the following academic programs, topics, and grants:

1. Research program of the Division of Physics and Astronomy of the National Academy of Sciences of Ukraine “Noise-inducing dynamics and correlations in nonequilibrium systems”, Project No. 0120U101347.
2. Research program of the Division of Physics and Astronomy of the National Academy of Sciences of Ukraine “Stochastic processes in condensed media, biological systems and radiation fields”, Project No. 0125U000031.
3. Project of National Research Foundation of Ukraine No. 2020.02/0111, “Nonclassical and hybrid correlations of quantum systems under realistic conditions”.
4. Project of National Research Foundation of Ukraine No. 2023.03/0165 “Quantum correlations of electromagnetic radiation”.
5. Project Simons Foundation International SFI-PD-Ukraine-00014573, PI LB.

1 Background

While classical optics provides a framework for electromagnetic wave propagation, it fails to capture the quantized and nonclassical properties of light. Quantum optics offers the theoretical framework for understanding features such as squeezing, entanglement, and high-order coherence. However, most quantum optical studies assume deterministic homogeneous propagation conditions. In reality, atmospheric turbulence introduces random fluctuations that degrade coherence and entanglement, turning a deterministic quantum channel into a stochastic one. Incorporating atmospheric turbulence into this framework introduces additional challenges due to the random, time-dependent nature of the propagation channel.

1.1 Quantum Optics

Classical optics, built on Maxwell's equations, describes light as a deterministic, smooth electromagnetic wave [1, 2]. It explains reflection, interference, diffraction, and polarization with remarkable success. But in the first half of the 20th century, it remained unclear whether light was truly a wave or a collection of quanta. While theoretical developments anticipated the photon concept, no experiment could prove its necessity [3]. The photoelectric effect, often referred to as evidence of photons, can also be described within a semiclassical framework: a continuous electromagnetic field interacting with quantized matter [4]. Taylor's double-slit experiment with extremely weak light, performed in 1909 [5], was later used as evidence in the debate over whether light behaves as a wave or as discrete quanta [6].

This uncertainty persisted until 1976, when Kimble, Dagenais, and Mandel developed [7] a theory describing the two-time intensity correlations of light emitted by a two-level atom, and then observed the photon antibunching effect experimentally in 1977 [8]. This phenomenon cannot be explained by any classical electromagnetic

field and confirms the quantum nature of light. Later on, many other quantum features of light were demonstrated [9]. The observation of squeezed states, which demonstrated variance below vacuum noise in one quadrature, was reported by Slusher et al. in 1985 [10]. An illustrative counter-intuitive example of multi-photon interference, the Hong-Ou-Mandel effect, was demonstrated by Hong et al. in 1987 [11]. Furthermore, numerous experimental tests of Bell inequalities using entangled photons have been performed in various configurations [12–16], highlighting the nonclassical correlations of light.

Despite the later development of experimental studies, the theoretical framework of quantum optics had already been well established much earlier. Foundational contributions were made by Glauber [17], Mandel [18], and other pioneers, who developed the groundwork for understanding the quantum properties of light long before many of the mentioned experiments were conducted. In the early 1960s, R. Glauber and E. C. G. Sudarshan introduced the idea of representing quantum states of a light mode $\hat{\rho}$ as a linear expansion over coherent states [19, 20]

$$\hat{\rho} = \int P(\alpha) |\alpha\rangle\langle\alpha| d^2\alpha, \quad (1.1)$$

where $|\alpha\rangle$ are coherent states—eigenvectors of the annihilation operator—which form an overcomplete basis of the Hilbert space [21], $d^2\alpha = d\text{Re}\alpha d\text{Im}\alpha$ and $P(\alpha)$ is the Glauber-Sudarshan P-function, a quasiprobability distribution over phase space. If $P(\alpha)$ is a non-negative function, the quantum state can be interpreted as a classical mixture of coherent fields; otherwise, the state exhibits nonclassical features [22, 23]. This idea is a part of the broader phase-space formalism of quantum mechanics [24], which has become the mainstream framework used today to describe quantum states of light.

1.2 Quantum light in atmosphere

The study of quantum light propagation through the atmosphere was initially motivated by the task of secure quantum communication, particularly Quantum Key Distribution (QKD). Unlike classical encryption, QKD security does not rely on computational hardness but on fundamental quantum laws forbidding perfect cloning of quantum states [25]. Photons are natural candidates for quantum communication [26] because they interact weakly with the environment, can be transmitted over long distances, and support multiple encoding degrees of freedom—polarization, phase, time-bin [27], or orbital angular momentum [28]. However, the description of light propagation through the atmosphere becomes complicated due to random fluctuations of the refractive index, which cause turbulence-induced effects such as beam wandering, wavefront distortion, and intensity scintillation [29–31].

1.2.1 *Experimental contributions*

Pioneering experimental efforts soon followed. Buttler et al. demonstrated the first outdoor QKD over a 1 km free-space link, proving that quantum states of light could survive real atmospheric conditions [32]. Shortly after, Hughes et al. extended this to a 1.6 km urban channel, showing that the combined effects of turbulence and background light could be effectively mitigated [33]. Entanglement-based experiments pushed the boundaries further. In 2007, Ursin et al. successfully distributed entangled photons over a 144 km free-space channel between the Canary Islands, demonstrating that quantum entanglement could be preserved over unprecedented long distances [34]. In 2008-2009, experiments involving Earth-based and satellite stations, for both uplinks and downlinks, enabled the analysis of the feasibility of various QKD protocols [35, 36]. The launch of the Micius satellite in 2016 enabled quantum communication between cities via satellite, linking ground stations in Beijing (China) and Graz (Austria), separated by 7600 km on Earth [37].

This demonstrated that long-distance quantum links can be maintained through the atmosphere despite turbulence, absorption, and background light, opening the way toward a global quantum network [38].

1.2.2 Foundation of classical theory of light in atmosphere

The theory of quantum light propagation in the atmosphere is based on classical studies of light propagation through turbulent media. The theoretical roots lie in the statistical theory of turbulence formulated by A. N. Kolmogorov (1941) [39]. Kolmogorov introduced a model for energy transfer in incompressible turbulent flows, where energy cascades from large to small scales. In the inertial range, this leads to the $\kappa^{-11/3}$ power spectrum of refractive-index fluctuations.

In the early theoretical treatments of wave propagation through random media, the Born approximation was first employed to describe single scattering events, assuming weak refractive-index fluctuations and negligible multiple scattering effects [31]. Later, Tatarskii, building on the Rytov approximation, introduced the second-order perturbation term [29], and presented a comprehensive theory of wave propagation in a turbulent atmosphere, rigorously connecting the statistical properties of refractive-index fluctuations with the resulting effects on optical waves [40]. This method is widely used for analyzing the statistical properties of optical fields propagating through a turbulent atmosphere, allowing one to compute quantities such as log-amplitude and phase variance functions, intensity and phase correlations, and structure functions. Nevertheless, this formulation remains valid only under weak turbulence conditions [31].

Further developments aimed at extending the range of validity beyond weak turbulence have employed alternative frameworks such as the parabolic equation method and extended Rytov theory [31], the phase approximation of the Huygens-Kirchhoff method [41], and the photon distribution function approach [42]. In contemporary studies, many approaches are based on the extended

Huygens-Fresnel principle [43]. However, it has been pointed out that commonly used variations of this method do not provide significant improvements over traditional methods [44].

An alternative and widely used approach for simulating wave propagation through turbulence is the phase-screen method [45–47]. In this technique, the turbulent medium is modeled as a series of discrete, statistically independent layers that impose random phase distortions on the wavefront, allowing efficient numerical computation of amplitude and phase fluctuations over long propagation distances. The theoretical description and implementation details of this method will be discussed in [Section 1.4.4](#).

1.2.3 Probability density function of the irradiance

Of particular interest is the probability density function of the irradiance. It provides a statistical description of the intensity fluctuations, or scintillations. In weak fluctuation regimes, assuming a Gaussian refractive-index field and using the Born approximation with first-order perturbation theory, the irradiance is described by the modified Rician distribution [48, 49]. However, experimental studies by Parry and Pusey [50] showed that the theoretical moments predicted by this model were systematically lower than measured values, even under weak turbulence conditions. Within the first-order Rytov approximation, the irradiance fluctuations are well described by the lognormal distribution [40, 49]. This model generally agrees well with observations for short propagation paths or weak turbulence, but fails to capture the statistics of irradiance under strong turbulence, indicating the need for more sophisticated models in such regimes.

While the irradiance fluctuations are well described by the lognormal distribution in weak turbulence, experiments show that under very strong turbulence, the distribution tends toward a negative exponential. To account for strong scintillations, several models have been proposed [31]. The K-distribution [51]

is based on a modulation process in which the irradiance follows a conditional negative exponential modulated by a gamma-distributed process, providing good agreement with experimental data. The lognormal-Rician distribution models the irradiance as Rician, modulated by a lognormal distribution, and has been shown to better fit experimental observations [52], although it does not have a closed-form expression. The Gamma-Gamma distribution [53] generalizes the K-distribution, with parameters that can be related to atmospheric conditions through models for large-scale and small-scale scintillations, and it offers a closed-form expression for the cumulative distribution function. Despite their empirical success in describing irradiance fluctuations in strong turbulence, these models remain phenomenological rather than being derived from first principles.

1.2.4 Probability density function of photocounting

In the studies discussed above, the optical intensity is typically high, resulting in a continuous photocurrent. However, when the intensity is on the order of individual photons and the detection time interval is short, the detector registers random discrete pulses. The quantity of interest in this regime is the probability density function of photocounts [9]. In 1970, it was proposed to modulate the photocounting statistics with the previously discussed lognormal distribution of the mean photon count [54]. While this approach can be useful in certain specific cases [55], the infinite tail of the lognormal distribution implies unphysical photon amplification, making it unsuitable as a general model and requiring further study to establish a description of atmospheric turbulence effects on quantum states. It is worth noting that in 2003, a similar problem was addressed in the context of radio-signal propagation with limited available power [56], where the Ricean distribution was effectively attenuated at values approaching the maximum power.

1.3 Quantum channels in turbulent atmosphere

In the work of Semenov and Vogel (2009) [57], a more general problem of quantum state of light transformation after propagation through a turbulent atmosphere was considered. They showed that a light beam distorted by atmospheric turbulence, when passing through a finite aperture, can be modeled as a linear-loss quantum channel. The channel is characterized by an effective transmittance $\eta \in [0, 1]$. This quantity represents the fraction of the total beam intensity that passes through the aperture.

While linear-loss channels can be specified in the density-operator formalism, a particularly elegant and tractable representation is obtained when quantum states are described in the Glauber-Sudarshan P -function representation (see Eq. (1.1)) [20, 58]. Then, the input-output relation for linear-loss channels can be expressed as

$$P_{\text{out}}(\alpha) = \frac{1}{\eta} P_{\text{in}} \left(\frac{\alpha}{\sqrt{\eta}} \right). \quad (1.2)$$

However, in the atmospheric case, the effective transmittance η is not a fixed constant. Since the refractive index $n(\mathbf{r}, t)$ is a random field, every realization of turbulence corresponds to a different value of η . Consequently, the atmospheric quantum channel is a statistical mixture of lossy channels, described by averaging over all possible transmittance values

$$P_{\text{out}}(\alpha) = \int_0^1 d\eta \mathcal{P}(\eta) \frac{1}{\eta} P_{\text{in}} \left(\frac{\alpha}{\sqrt{\eta}} \right), \quad (1.3)$$

where $\mathcal{P}(\eta)$ is the probability density of transmittance (PDT). The PDT encodes the statistics of turbulence and depends on multiple parameters: the source beam properties (e.g., waist size, wavelength), the atmospheric channel (e.g., turbulence strength, path length, model), and the aperture geometry. The probability density of

transmittance (PDT) is the primary defining characteristic of atmospheric quantum channels, as it fully captures the stochastic effects of turbulence on the output quantum state.

The input-output relation [Eq. \(1.3\)](#) holds for both classical and quantum fields since the PDT $\mathcal{P}(\eta)$ is identical in both regimes. This correspondence is evident when considering an input coherent state $|\alpha_0\rangle$, characterized by the P -function $\delta^{(2)}(\alpha - \alpha_0)$, which results in an output state represented as a statistical mixture of attenuated coherent states. Consequently, the task of determining the PDT for an atmospheric quantum channel is equivalent to solving the corresponding classical stochastic propagation problem.

Direct experimental reconstruction of the PDT is possible with classical intensity measurements at the receiver side with a photodiode. However, experimental studies of PDT properties are generally complicated. Measurements must be carried out under uncontrolled atmospheric conditions, which complicates the study, and temporal fluctuations further hinder precise characterization. These difficulties highlight the importance of studying atmospheric quantum channels in a controlled and well-characterized way.

1.3.1 Analytical models of PDT

Several analytical models of the PDT were developed between 2009 and 2018 to describe the statistical properties of atmospheric quantum channels. These models are typically formulated in terms of parameters derived from the field correlation function. The first group consists of models defined by transmittance moments, such as average transmittance and transmittance variance.

The truncated lognormal distribution model [\[57\]](#) is based on the lognormal model of irradiance (see [Section 1.2.3](#)). Since the lognormal distribution has an infinite bound but the PDT requires values between 0 and 1, an additional truncation condition is introduced at $\eta = 1$. Despite being derived under the

Rytov approximation in classical optics, this model was reported to yield reasonable agreement under strong turbulence conditions [59, 60].

Alternatively, an empirical approach based on the Beta distribution [61] was introduced in our work [I]. In this model, the PDT is defined using the first two transmittance moments as

$$\mathcal{P}(\eta; \langle \eta \rangle, \langle \eta^2 \rangle) = \frac{1}{B(a, b)} \eta^{a-1} (1 - \eta)^{b-1}, \quad (1.4)$$

where $B(a, b)$ is the Beta function and the parameters a and b are expressed through the first two moments as

$$a = \frac{\langle \eta \rangle - \langle \eta^2 \rangle}{\langle \eta^2 \rangle - \langle \eta \rangle^2} \langle \eta \rangle \quad \text{and} \quad b = \frac{\langle \eta \rangle - \langle \eta^2 \rangle}{\langle \eta^2 \rangle - \langle \eta \rangle^2} (1 - \langle \eta \rangle). \quad (1.5)$$

This model is particularly convenient because it has a natural support on the interval $[0, 1]$ and provides a simple analytical expression that closely resembles numerically obtained distributions across a wide range of turbulence conditions.

The second group comprises models defined by beam-spot parameters at the aperture plane, such as the mean beam-spot radius, the variance of the beam-centroid position, and higher moments. The beam-wandering model [62] accounts for the random deflection of the beam centroid from the propagation axis while neglecting beam-shape deformation. It assumes a normally distributed beam-centroid position in the aperture plane, resulting in a log-negative Weibull distribution for the PDT. The model depends only on the beam-shape parameters, and it is assumed to be applicable under weak turbulence conditions.

The elliptical-beam model [60] extends the beam-wandering approach by incorporating elliptical shape distortions, thereby capturing additional contributions to the cumulative beam decomposition of the intensity at the aperture plane. This added complexity requires numerical evaluation of the model parameters. This

model was also proposed for weak or weak-to-moderate turbulence [60, 63].

Finally, the total probability law model [63] separates the effects of beam wandering and beam-shape distortion. It assumes that the shape distortion can be described by a truncated lognormal distribution. The advantage of this model is that it provides accurate values of the mean transmittance; however, the model parameters must be determined numerically.

In conclusion, various models exist based on both phenomenological approaches and physically grounded formulations. However, the further development of purely analytical, physically justified models is limited by the difficulty of expressing their parameters in closed analytical form. In addition, all analytical models are formulated in terms of field correlation functions, which themselves involve significant approximations. It also remains an open question under which conditions each model should be applied.

1.4 Numerical simulation framework

1.4.1 Preliminaries on random functions theory

When studying light propagation through random media, it is necessary to introduce a minimal framework for random functions. In our problem, randomness enters through spatial variations of the refractive index, which in turn induces randomness in most derived quantities such as beam properties at the aperture plane and the transmittance values. By treating these quantities as random functions, we can systematically describe their statistical properties, characterize correlations, study ergodicity property, the Markov property, etc [9, 31, 64].

We consider a function ξ of two parameters

$$\xi : T \times \Omega \rightarrow \xi(t, \omega), \quad (1.6)$$

where $t \in T$ is a domain parameter (e.g., time or space) and $\omega \in \Omega$ is an outcome. This representation admits two standard viewpoints. If we fix the outcome ω , the function $\xi^{(\omega)}(t)$ is a deterministic function, called a sample path (or realization) of the random function. Examples of two sample paths as functions of t are shown in Fig. 1.1. For a fixed domain parameter t , we obtain a random variable ξ_t . Thus, the random function can equivalently be viewed as a family of random variables $\{\xi_t\}_{t \in T}$ indexed by $t \in T$.

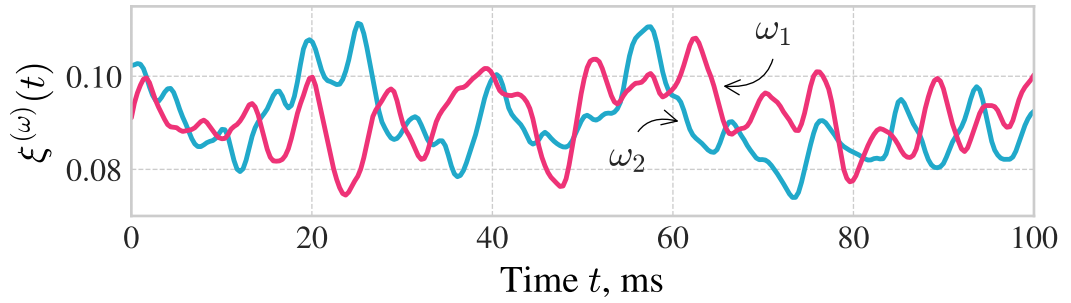


Figure 1.1 – Examples of two sample paths of the random function $\xi(t, \omega)$. In this context, the random function represents atmospheric channel transmittance η . The pink line corresponds to the realization $\xi^{(\omega_1)}(t)$, while the blue line corresponds to $\xi^{(\omega_2)}(t)$. Each path illustrates the deterministic evolution of the channel transmittance over time t for a fixed outcome ω .

A random function can be defined by specifying all its distribution functions of the form [65]

$$\begin{aligned}
 F_t(x) &= \mathbb{P}[\xi_t < x], \quad \forall t \in T \\
 F_{t_1, t_2}(x_1, x_2) &= \mathbb{P}[\xi_{t_1} < x_1, \xi_{t_2} < x_2], \quad \forall t_1, t_2 \\
 &\dots \\
 F_{t_1, \dots, t_n}(x_1, \dots, x_n) &= \mathbb{P}[\xi_{t_1} < x_1, \dots, \xi_{t_n} < x_n], \quad \forall t_i, i \in [1 \dots n], \forall n.
 \end{aligned} \tag{1.7}$$

Another convenient way to specify a random function is using an analytic formula containing parameters which are random variables. We will call time-indexed random functions random processes, and random fields random functions indexed

by multidimensional (2D or 3D) spatial variables.

Stationary random functions. In physics, a common class of random functions consists of stationary random functions. A random function is stationary if all of its finite-dimensional distribution functions (see Eq. (1.7)) are invariant under parameter shifts

$$F_{t_1+\tau, \dots, t_n+\tau}(x_1, \dots, x_n) = F_{t_1, \dots, t_n}(x_1, \dots, x_n), \quad \forall t_i, i \in [1 \dots n], \forall n. \quad (1.8)$$

This simplifies the analysis such as all functions $F_t(x) \forall t \in T$ are identical, hence we need only one $F_{t_0}(x)$; and instead of considering $F_{t_1, t_2}(x_1, x_2) \forall t_1, t_2$ we need only the family of joint distributions indexed by the time difference $\tau = t_2 - t_1$, and so forth.

We can characterize random functions using moments. The first moment $\mu(t) = \mathbb{E} \xi_t = \int_{-\infty}^{\infty} x dF_t(x)$ is the mean value. For a stationary random function it is constant, $\mu = \mu(t)$, which means that it is often useful to redefine our random process with a new random process $\xi_t - \mu$. The second moment yields the correlation function, which provides a more detailed characterization of the random function

$$B(t_1, t_2) = \mathbb{E} \xi_{t_1} \overline{\xi_{t_2}} = \int_{-\infty}^{\infty} \int_{-\infty}^{\infty} x_1 x_2 dF_{t_1, t_2}(x_1, x_2). \quad (1.9)$$

For a stationary random function it depends only on the time difference $\mathbb{E} \xi_t \overline{\xi_{t+\tau}} = B(\tau)$.

While the correlation function characterizes how similar the values are at a given separation, it is sometimes useful to consider how different they are, which can be done using the structure function

$$D(t_1, t_2) = \mathbb{E} |\xi_{t_1} - \xi_{t_2}|^2 = \int_{-\infty}^{\infty} \int_{-\infty}^{\infty} |x_1 - x_2|^2 dF_{t_1, t_2}(x_1, x_2). \quad (1.10)$$

The structure function is a powerful tool in the theory of random functions with stationary increments [39], but in the case of stationary functions it also depends only on the time difference τ and relates to the correlation function as $D(\tau) = 2 (B(0) - \text{Re } B(\tau))$. In turbulent atmosphere science it is also common to characterize random fields using the complimentary to correlation function power spectral density function $\Phi(k)$, defined as a Fourier transform [66, 67]

$$\Phi(\lambda) = \frac{1}{2\pi} \int e^{-i\lambda\tau} B(\tau) d\tau. \quad (1.11)$$

In one of the following subsections we will explicitly present several models for a refractive-index random field using the power spectral density function formalism.

Spectral representation. As in the case of regular functions, it can be useful to represent random functions in the form of Fourier transform. It has been shown that any stationary random function can be arbitrarily closely represented on some interval $-T < t < T$ as a linear combination of a finite number of independent harmonic oscillators of the form $\xi_k e^{i\lambda_k t}$, where ξ_k are complex random variables with zero mean and λ_k are real constants. In the limit we obtain the spectral representation theorem (Cramér-Karhunen), which states that any stationary process $\xi(t)$ can be represented in the form of a Fourier-Stieltjes integral

$$\xi(t) = \int_{-\infty}^{\infty} e^{i\lambda t} dZ(\lambda), \quad (1.12)$$

where $dZ(\lambda)$ is a random increment that associates a random variable with each interval $[\lambda, \lambda + d\lambda]$, satisfying the properties

$$\mathbb{E} [dZ(\lambda)] = 0, \quad \mathbb{E} [dZ(\lambda_1) \overline{dZ(\lambda_2)}] = 0, \quad \mathbb{E} [|dZ(\lambda)|^2] = \Phi(\lambda) d\lambda, \quad (1.13)$$

where $\lambda_1 \neq \lambda_2$, and $\Phi(\lambda)$ power spectral density function of the process (assuming it is absolutely continuous).

1.4.2 *Theory of turbulent atmosphere*

Turbulence is widely recognized as one of the most complex and challenging phenomena in nature. The complexity is rooted in the Navier-Stokes equations, which results in the non-linear, multi-scale, and intrinsically chaotic behavior of the system, making precise prediction impossible over extended periods [68, 69]. Thus, atmospheric studies mostly rely on statistical descriptions [39] and the main object for description is the velocity random field.

Energy cascade model of turbulence. There are various sources that create turbulence, such as wind shear, thermal convection, buoyancy effects, and obstacles, but the statistical properties of the resulting flow tend to show similar universal behavior. We assume that the turbulent atmosphere is stationary, homogeneous, and isotropic. Stationarity implies that the statistical properties of the flow do not change over time. Homogeneity means that no particular location in space is special. Isotropy requires that no direction is privileged. This assumption forms a workable starting point for studying the statistical properties of turbulence.

Let us consider the structure function of the velocity field—the ensemble average over turbulent atmospheric realizations of the square of longitudinal velocity difference at two points in space,

$$D_v(r) = \langle |v(x) - v(x + r)|^2 \rangle \equiv v_r^2. \quad (1.14)$$

Since we assume homogeneous and isotropic turbulence, the statistics of fluctuations do not depend on the direction. We can define two time scales: the “inertial” time $T_I \sim r/v_r$ at which the structure of velocity difference deforms, and the “viscous”

time $T_\nu \sim r^2/\nu$ at which the structure of velocity difference is smoothed by viscosity [70]. Here ν is the kinematic viscosity (momentum diffusivity). The ratio of these two time scales defines the Reynolds number $\mathcal{R}_r = T_\nu/T_I = v_r r/\nu$. When $\mathcal{R}_r \gg 1$, the viscous time is much longer than the inertial time, thus the structure of velocity difference deforms into other (smaller) structures before its energy dissipates by viscosity. For $\mathcal{R}_r < 1$ the structures dissipate their energy rapidly due to viscosity.

It is widely used in the literature to associate these structures with turbulent eddies of diameter r and linear velocity difference v_r . Then, inertial time corresponds to the time it takes for an eddy to complete one rotation. Although turbulent eddies are not well defined, they can be valuable for illustrating the intuition about turbulence dynamics.

We can define two characteristic lengths that play an important role in turbulent atmosphere theory. The outer scale of turbulence L_0 can be considered as the typical size of the largest eddies or characteristic size of the system, such as the altitude of laser beam propagation [71], with typical values of $L_0 \approx 20\text{m} - 100\text{m}$ [72]. The inner scale of turbulence l_0 can be considered as the scale at which $\mathcal{R}_{l_0} \approx 1$, with typical values of $l_0 \approx 1\text{mm} - 1\text{cm}$. The interval of scales between l_0 and L_0 is referred to as the inertial range.

Structure function of the velocity field. In the 1940s Kolmogorov assumed [39] that energy enters the turbulent system at large scales L_0 , cascades through inertial range scales without energy loss, and finally dissipates at the l_0 scale due to viscosity. This mechanism is referred to as the energy cascade model of turbulence. In this case, the energy flux from one scale to another per unit mass, defined as the kinetic energy divided by the deformation time, must be a constant

$$\varepsilon \sim \frac{v_r^2}{T_I} = \frac{v_r^3}{r} = \text{const.} \quad (1.15)$$

The dimensional analysis implies that the structure function (see Eq. (1.14)) must be proportional to

$$D_v(r) \sim (\varepsilon r)^{2/3} \equiv C_v^2 r^{2/3}, \quad l_0 \ll r \ll L_0, \quad (1.16)$$

where C_v^2 is the velocity structure constant (units of $\text{m}^4/3\text{s}^{-2}$).

Structure function of the index of refraction. The refractive index n is the primary parameter of the medium that affects light propagation. It, in turn, depends on temperature, pressure, humidity, and other atmospheric variables. The dominant contribution arises from temperature fluctuations, since temperature relaxes much more slowly than the other parameters [73]. In the inertial range of turbulence, the advective transport strongly dominates over diffusion, hence temperature behaves as a passive scalar transported by the turbulent velocity field. Consequently, the structure functions of the refractive index, temperature, and velocity fields exhibit the same scaling behavior $D_n(r) \sim D_T(r) \sim D_v(r)$, and therefore

$$D_n(r) = C_n^2 r^{2/3}, \quad l_0 \ll r \ll L_0, \quad (1.17)$$

where C_n^2 is the refractive-index structure constant, which primarily determines the strength of the turbulence.

It is also very common to define the Kolmogorov turbulence model with the power spectral density function (see Eq. (1.11)) as

$$\Phi(\kappa) = 0.033 C_n^2 \kappa^{-11/3} \quad 2\pi/L_0 \ll \kappa \ll 2\pi/l_0, \quad (1.18)$$

where $\kappa = 2\pi/l$ is the spatial frequency and C_n^2 is the refractive index structure constant. Near ground level, C_n^2 ranges from around $10^{-17} \text{ m}^{-2/3}$ (weak turbulence)

to $10^{-13} \text{ m}^{-2/3}$ (strong turbulence) [31].

The Kolmogorov power-law spectrum model, because of its simple expression, is mostly used in analytical calculations. However, the $-11/3$ power introduces some challenges when used under integrals over κ . Another problem with this model arises when we take a look at the low-wavenumber region. We can see that this model yields an infinite value of power density as $L_0 \rightarrow \infty$, which is sometimes used to simplify calculations. Such unphysical conditions can be fixed by introducing models that behave identically in the inertial region but smoothly fall off in the energy and viscous ranges. One such model is the modified von Kármán model, which introduces a decay of the power spectral density at the l_0 and L_0 scales

$$\Phi_n(\kappa) = 0.033 C_n^2 \frac{\exp(-\kappa^2/\kappa_m^2)}{(\kappa^2 + \kappa_0^2)^{11/6}}, \quad (1.19)$$

where $\kappa_0 = 2\pi/L_0$ and $\kappa_m = 5.92/l_0$ represent the outer and inner scale cutoffs, respectively.

It is worth emphasizing that when this turbulence theory was first proposed, it consisted entirely of theoretical predictions. Its experimental confirmation came nearly a decade later and showed the first clear validation of the theory. After some time, more sophisticated numerical and analytical approaches based directly on the Navier-Stokes equations were conducted [74]. These studies validated the $-5/3$ power-law dependence of the energy spectrum in the inertial subrange. However, they also revealed additional fine structures, such as a small bump in the high-frequency (viscous) range of the spectrum [75]. But overall, while the refined models introduced deeper physical insights, they largely supported the fundamental scaling laws established by Kolmogorov and the modified von Kármán spectrum.

Figure 1.2 summarizes the model of atmospheric turbulence. It depicts the energy flow across various scales. The process begins at large scales of energy injection and moves through the inertial range, where turbulent motion is the

predominant mechanism. Finally, the energy reaches the region where it is dissipated by viscosity.

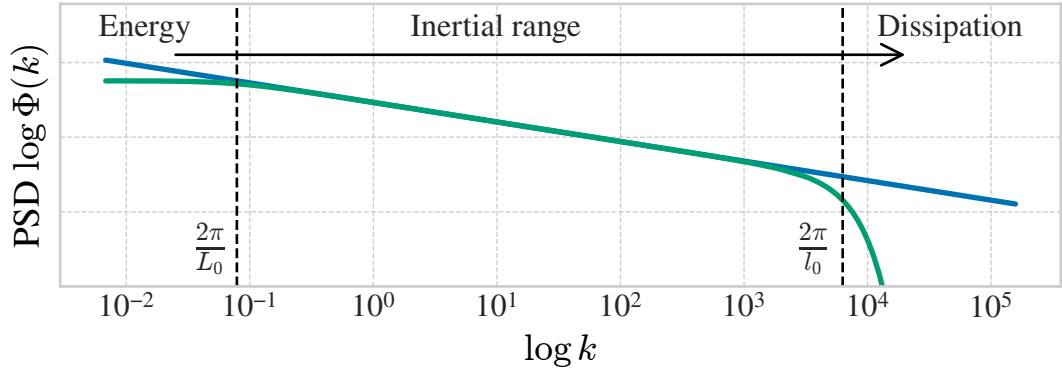


Figure 1.2 – Power spectral density of atmospheric turbulence models. The blue line represents the Kolmogorov model, while the green line depicts the Modified von Kármán model, highlighting how the latter accounts for the inner and outer scales (l_0 and L_0).

Frozen turbulence hypothesis. The Kolmogorov model, along with its modifications such as the von Kármán spectrum, provides a strong theoretical basis for understanding the ensemble-averaged statistics of turbulence. However, these models do not directly address the temporal statistics of the turbulent field. This lack of a temporal description is critical for several reasons. It is required for studying the temporal properties of the impact of the turbulent atmosphere on phenomena such as light propagation. For experimental atmospheric studies, most atmospheric experiments rely on a small number of fixed in space sensors to record fluctuations over time because this setup is significantly easier to realize in practice than true spatial sampling. The answer to the question of how to compare temporal data with spatial statistics was provided by G. I. Taylor in 1937 through the Frozen Turbulence Hypothesis [76].

The hypothesis is based on the difference between two atmospheric time scales. The first is the advection time, which can be defined as the duration required

for the mean wind of speed v to carry a turbulent structure of size r across the observation point, given by $T_v = r/v$. The second is the mentioned in [Section 1.4.2](#) inertial time $T_I \sim r/v_r$. The typical value for mean wind speed is $v \sim 5\text{--}20\text{ m/s}$ under moderate to strong wind conditions, while $v_r \sim 0.1\text{--}2\text{ m/s}$ represents the root-mean-square velocity fluctuation. Then, in cases where the advection time is much smaller than the inertial time $T_v/T_I = v_r/v \ll 1$, we can assume that the refractive index field is effectively frozen and evolves in time by moving with a constant wind speed $\mathbf{v} : |\mathbf{v}| = v$ as a whole

$$n(\mathbf{r}, t) = n(\mathbf{r} - \mathbf{v}t, 0). \quad (1.20)$$

The intuition behind this can be supported by looking at clouds, which seem to keep their shape for a long time while drifting steadily with the wind. This phenomenon is known as the Taylor frozen turbulence hypothesis.

The Taylor frozen turbulence hypothesis is subject to several restrictions. As in the general Kolmogorov model of turbulence, it assumes that the turbulence is roughly homogeneous and isotropic. A key requirement of the hypothesis is that the advection time is much smaller than the inertial (or evolution) time of the turbulent structures, ensuring that changes in the turbulence during transport are negligible. The hypothesis also assumes a constant wind speed in both magnitude and direction; near obstacles, the ground, or in the presence of gusts, deviations from this assumption may occur. Despite these limitations, the frozen turbulence approximation is widely used in practice and provides a useful framework for modeling time-dependent turbulent fields.

1.4.3 *Light beam propagation in inhomogeneous media*

To obtain the transmittance of the atmospheric quantum channel, we must solve the classical problem of light propagation through stochastic isotropic media.

This process involves characterizing how random fluctuations in the medium alter the beam's power distribution. To that end, this section defines the fundamental equations governing the evolution of the complex field amplitude and the resulting intensity at the aperture plane.

Paraxial wave equation in stochastic media. The propagation of electromagnetic fields in the atmosphere is described by the scalar wave equation [77, 78]. Separating temporal and spatial variables yields the Helmholtz equation

$$\nabla^2 E + k^2 n^2(\mathbf{r}, z) E = 0, \quad (1.21)$$

where ∇^2 is the Laplacian operator, k is the vacuum wave number and E is the complex spatial amplitude. For Gaussian beams propagating along the z -axis over long distances, the paraxial approximation becomes valid [78]. We express the complex amplitude in terms of a slowly varying complex envelope as $E(\mathbf{r}; z) = u(\mathbf{r}; z)e^{ikz}$. Under the paraxial approximation the envelope $u(\mathbf{r}; z)$ is a slowly varying function of z , satisfying the condition $\left| \frac{\partial^2 u}{\partial z^2} \right| \ll \left| k \frac{\partial u}{\partial z} \right|$. We also assume that $\delta n(\mathbf{r}, z)^2 \approx 0$, where $\delta n(\mathbf{r}, z) = n(\mathbf{r}, z) - 1$ represents the refractive index perturbation. By neglecting second-order terms in the refractive index perturbation $\delta n^2 \approx 0$, where $\delta n(\mathbf{r}, z) = n(\mathbf{r}, z) - 1$, the equation reduces to the paraxial scalar wave equation in a medium with spatially varying refractive index

$$\boxed{2ik \frac{\partial u(\mathbf{r}; z)}{\partial z} + \Delta_{\mathbf{r}} u(\mathbf{r}; z) + 2k^2 \delta n(\mathbf{r}, z) u(\mathbf{r}; z) = 0}, \quad (1.22)$$

where $\Delta_{\mathbf{r}}$ represents the transverse Laplacian operator.

Gaussian beam source. In this work, we restrict the analysis to the Gaussian beam mode at the transmitter plane [78]. Gaussian modes provide an accurate

approximation of the output of most laser sources used in free space optical communication. Because of this, they are widely adopted in theoretical modeling and experimental studies of atmospheric optical channels. The boundary condition at the transmitter plane $z = 0$ is given by the Gaussian beam [31]

$$u(\mathbf{r}; 0) = \sqrt{\frac{2}{\pi W_0^2}} \exp \left[-\frac{\mathbf{r}^2}{W_0^2} - \frac{ik}{2F_0} \mathbf{r}^2 \right], \quad (1.23)$$

where W_0 is the beam waist radius and F_0 is the radius of curvature of the wavefront. For collimated beams, $F_0 \rightarrow \infty$, while for focused beams, F_0 takes finite values.

Vacuum propagation. For the case $\delta n = 0$ (homogeneous medium), the solution becomes straightforward. The Fresnel diffraction integral [79] describes the field evolution

$$u(x, y, z) = \frac{e^{ikz}}{i\lambda z} \iint_{-\infty}^{\infty} u(x', y', 0) e^{i\frac{k}{2z}[(x-x')^2 + (y-y')^2]} dx' dy'. \quad (1.24)$$

This integral represents a convolution with the propagation kernel, based on the Huygens-Fresnel principle where each wavefront point acts as a source of secondary spherical wavelets. In the spatial frequency domain, this convolution becomes multiplication with the transfer function $H(f_x, f_y, z) = e^{ikz} e^{-i\pi\lambda z(f_x^2 + f_y^2)}$, known as the angular spectrum method [79]. This formulation enables efficient numerical implementation using Fast Fourier Transform algorithms.

Transmittance of channel. To simulate the PDT, we must first calculate the transmittance value at the aperture plane $z = z_{\text{ap}}$ for various channel realizations. This is achieved by integrating the squared magnitude of the optical field over the

entire receiving aperture \mathcal{A} as follows

$$\eta = \int_{\mathcal{A}} d^2\mathbf{r} |u(\mathbf{r}; z_{\text{ap}})|^2. \quad (1.25)$$

Specifically, the integration domain \mathcal{A} represents the circular region of the pupil with radius R_{ap} , and $d^2\mathbf{r} = dx dy$.

Statistical properties of a light beam in turbulence. In the absence of refractive index fluctuations, a Gaussian beam (see [Eq. \(1.23\)](#)) propagating in free space keeps its deterministic Gaussian profile at the aperture plane, as it represents the exact solution of the paraxial wave equation [78]. When the beam travels through a turbulent atmosphere, random changes in the refractive index make the optical field at the aperture plane a stochastic quantity. To efficiently compress the vast amount of information required to describe the optical field distorted by turbulence, it is convenient to characterize the random fluctuations of the complex amplitude in terms of its second- and fourth-order correlation functions [31]

$$\begin{aligned} \Gamma_2(\mathbf{r}; z) &= \langle |u(\mathbf{r}; z_{\text{ap}})|^2 \rangle, \\ \Gamma_4(\mathbf{r}_1, \mathbf{r}_2; z_{\text{ap}}) &= \langle |u(\mathbf{r}_1; z_{\text{ap}})|^2 |u(\mathbf{r}_2; z_{\text{ap}})|^2 \rangle, \end{aligned} \quad (1.26)$$

where $\langle \cdot \rangle$ denotes ensemble averaging over turbulence realizations.

These correlation functions enable the calculation of several statistical quantities that are essential for parametrizing analytical models of atmospheric channels. The average transmittance of the atmospheric channel, according to [Eq. \(1.25\)](#), is given by

$$\langle \eta \rangle = \left\langle \int_{\mathcal{A}} d^2\mathbf{r} |u(\mathbf{r}, z_{\text{ap}})|^2 \right\rangle = \int_{\mathcal{A}} d^2\mathbf{r} \Gamma_2(\mathbf{r}, z_{\text{ap}}) \quad (1.27)$$

and can be seen as the primary characteristic of channel effectiveness. The second moment of the transmittance

$$\begin{aligned}\langle \eta^2 \rangle &= \left\langle \int_{\mathcal{A}} d^2 \mathbf{r}_1 |u(\mathbf{r}_1, z_{\text{ap}})|^2 \int_{\mathcal{A}} d^2 \mathbf{r}_2 |u(\mathbf{r}_2, z_{\text{ap}})|^2 \right\rangle = \\ &= \int_{\mathcal{A}} \int_{\mathcal{A}} d^2 \mathbf{r}_1 d^2 \mathbf{r}_2 \Gamma_4(\mathbf{r}_1, \mathbf{r}_2, z_{\text{ap}})\end{aligned}\quad (1.28)$$

requires the fourth-order correlation function and characterizes the variability of the atmospheric channel transmittance.

Let us consider the statistical properties of the beam-spot at the aperture plane [31]. The simplest property is the beam centroid, which is defined for a single realization of turbulent atmosphere as

$$x_0 = \int_{\mathbb{R}^2} d^2 \mathbf{r} x |u(\mathbf{r}, z_{\text{ap}})|^2. \quad (1.29)$$

While it is obvious that under the assumption of isotropic turbulence (see [Section 1.4.2](#)) the average value of the beam centroid $\langle x_0 \rangle = 0$, it remains an open question whether its distribution is Gaussian. In particular, for strong turbulence the distribution can deviate, for example by exhibiting heavy tails. The second moment is referred to as the long-term beam-spot radius. It is defined as

$$W_{\text{LT}}^2 = 4 \int_{\mathbb{R}^2} d^2 \mathbf{r} x^2 \Gamma_2(\mathbf{r}, z_{\text{ap}}) \quad (1.30)$$

and represents the effective spatial extent of the beam after propagation through turbulence, incorporating both diffraction and spreading due to turbulence effects. The variance of the beam-centroid coordinate, often referred to as beam wandering, characterizes the random displacement of the beam centroid

$$\sigma_{\text{BW}}^2 = \langle x_0^2 \rangle = \int_{\mathbb{R}^4} d^2 \mathbf{r}_1 d^2 \mathbf{r}_2 x_1 x_2 \Gamma_4(\mathbf{r}_1, \mathbf{r}_2, z_{\text{ap}}). \quad (1.31)$$

Complementary to these two quantities is the squared beam-spot radius, which is also referred to as the short-term beam-spot radius, defined as

$$S = 4 \int_{\mathbb{R}^2} d^2\mathbf{r} (x - x_0)^2 \Gamma_2(\mathbf{r}, z_{\text{ap}}) = W_{\text{LT}}^2 - 4\sigma_{\text{BW}}^2, \quad (1.32)$$

which characterizes the average instantaneous width of the beam, excluding the contribution from beam wandering.

1.4.4 Phase screens method

Analytical approaches to wave propagation in random media rely on many restrictive assumptions [44], which limit their applicability to weak and sometimes moderate turbulence. Moreover, the ensemble averaging inherent to these analytical treatments provides only statistical quantities of the optical field, such as mean intensity, correlation functions, or the scintillation index. Consequently, this leaves us without access to individual realizations of beam spots and their spatial dynamics.

The phase-screen method [45, 80, 81] is one of the standard numerical techniques for modeling wave propagation through a randomly inhomogeneous medium such as atmospheric turbulence. The main idea is to represent the effect of turbulence along the propagation path as a sequence of thin phase-modulating layers separated by free-space propagation intervals. Each screen imposes a random phase distortion corresponding to the integrated refractive-index fluctuations over a short segment of the path, while free-space propagation between screens accounts for diffraction and interference effects.

Symmetric split-step operator. To formalize this idea, we rewrite the paraxial wave equation (see Eq. (1.22)) in the form of the first-order differential

equation with an operator on the right-hand side

$$\frac{\partial u(\mathbf{r}; z)}{\partial z} = \left[\underbrace{\frac{i}{2k} \Delta_{\mathbf{r}}}_{H_d} + \underbrace{ik \delta n(\mathbf{r}, z)}_{H_t(z)} \right] u(\mathbf{r}; z) \equiv H(z) u(\mathbf{r}; z), \quad (1.33)$$

where H_d corresponds to the contribution from diffraction, $H_t(z)$ corresponds to the contribution from turbulence, $H(z) = H_d + H_t(z)$. In general, since these operators do not commute, $H_d H_t \neq H_t H_d$. The solution to this type of equation can be formally written in the operator form

$$u(\mathbf{r}; z) = \tau \exp \left[\int_0^z H(z') dz' \right] u(\mathbf{r}; 0), \quad (1.34)$$

where τ denotes the space-ordering operator, introduced by analogy with the Dyson series, as

$$\begin{aligned} \tau \exp \left[\int_0^z H(z') dz' \right] &= 1 + \int_0^z H(z') dz' + \int_0^z H(z') dz' \int_0^{z'} H(z'') dz'' + \\ &+ \int_0^z H(z') dz' \int_0^{z'} H(z'') dz'' \int_0^{z''} H(z''') dz''' + \dots, \end{aligned} \quad (1.35)$$

where $z > z' > z'' > z''' > \dots$. We expand it to the second order in z

$$\begin{aligned} \tau \exp \left[\int_0^z H(z') dz' \right] &= 1 + H_d z + \int_0^z H_t(z') dz' + \\ &+ \frac{1}{2} H_d^2 z^2 + H_d \int_0^z dz' \int_0^{z'} H_t(z'') dz'' + \\ &+ \int_0^z H_t(z') H_d z' dz' + \int_0^z H_t(z') dz' \int_0^{z'} H_t(z'') dz'' + O(z^3). \end{aligned} \quad (1.36)$$

Let us consider the following ansatz (with regular exponentials) and expand it to the second order

$$\begin{aligned}
& \exp\left(\frac{1}{2}H_d z\right) \exp\left(\int_0^z H_t(z') dz'\right) \exp\left(\frac{1}{2}H_d z\right) = \\
& = 1 + H_d z + \int_0^z H_t(z') dz' + \frac{1}{2}H_d^2 z^2 + \frac{1}{2}\left[H_d z \int_0^z H_t(z') dz' + \right. \\
& \left. + z \int_0^z H_t(z') H_d dz' + 2 \int_0^z H_t(z') dz' \int_0^{z'} H_t(z'') dz''\right] + O(z^3).
\end{aligned} \tag{1.37}$$

Comparing it with the previous expression, we can write

$$\begin{aligned}
\tau \exp\left[\int_0^z H(z') dz'\right] &= \exp\left(\frac{1}{2}H_d z\right) \exp\left(\int_0^z H_t(z') dz'\right) \exp\left(\frac{1}{2}H_d z\right) + \\
&+ H_d \int_0^z dz' \int_0^{z'} H_t(z'') dz'' + \int_0^z H_t(z') H_d z' dz' - \\
&- \frac{1}{2}H_d z \int_0^z H_t(z') dz' - z \int_0^z H_t(z') H_d dz' + O(z^3).
\end{aligned} \tag{1.38}$$

Then, if the turbulence term can be represented as a Taylor series in z as $H_t(z) = H_t(0) + H'_t(0)z + H''_t(0)z^2 + \dots$, then all the integral terms vanish (at the 0-th order of the H_t series) or become of order $O(z^3)$. Finally, we can write

$$\boxed{u(\mathbf{r}; z) \approx \underbrace{\exp\left(\frac{z}{2} \frac{i}{2k} \Delta_{\mathbf{r}}\right)}_{\text{vacuum prop. on } z/2} \exp\left(\underbrace{ik \int_0^z \delta n(\mathbf{r}, z') dz'}_{\phi(\mathbf{r}) - \text{phase screen}}\right) \underbrace{\exp\left(\frac{z}{2} \frac{i}{2k} \Delta_{\mathbf{r}}\right)}_{\text{vacuum prop. on } z/2} u(\mathbf{r}; 0).} \tag{1.39}$$

That means that for light beam propagation in a turbulent atmosphere, we can decouple the diffraction impact and the turbulence impact to second order of accuracy by z . As a result, the light field amplitude of the beam at distance z can be obtained by propagating the initial field $u(\mathbf{r}; 0)$ as in vacuum over half the total distance, applying

the integrated phase perturbation induced by index of refraction perturbation and propagating this perturbed field again in vacuum over a distance $z/2$.

The accumulated phase delay caused by refractive-index fluctuations within a segment of propagation distance z is referred to as the phase screen $\phi(\mathbf{r})$

$$\boxed{\phi(\mathbf{r}) = k \int_0^z \delta n(\mathbf{r}, z') dz'}. \quad (1.40)$$

It is easy to see that $\langle \phi(\mathbf{r}) \rangle = 0$ and $\phi(\mathbf{r})$ is a stationary random field in the 2D space of $\mathbf{r} = (x, y)$. To define the power spectral function Φ_ϕ , let us consider the correlation function

$$B_\phi(\mathbf{r} = \mathbf{r}_2 - \mathbf{r}_1) = k^2 \int_0^z dz_1 \int_0^z dz_2 \langle \delta n(\mathbf{r}_1, z_1) \delta n(\mathbf{r}_2, z_2) \rangle. \quad (1.41)$$

Considering the case when the phase-screen thickness z is much greater than the longitudinal correlation length of the refractive-index fluctuations, we can assume that correlations along the propagation direction are averaged out. This allows us to apply the Markov approximation [45]

$$\langle \delta n(\mathbf{r}_1, z_1) \delta n(\mathbf{r}_2, z_2) \rangle \simeq \delta(z_1 - z_2) \int_{-\infty}^{\infty} dz' B_n(\mathbf{r}_2 - \mathbf{r}_1, z'). \quad (1.42)$$

Rewriting both correlation functions in terms of spectral density functions and integrating the delta function, we obtain

$$\iint d^2\boldsymbol{\kappa} \Phi_\phi(\boldsymbol{\kappa}) e^{-i\boldsymbol{\kappa}\mathbf{r}} = k^2 \int_0^z dz_1 2\pi \iint d^2\boldsymbol{\kappa} \Phi_n(\boldsymbol{\kappa}, \kappa_z = 0) e^{-i\boldsymbol{\kappa}\mathbf{r}}, \quad (1.43)$$

which means that the spectral density function of the phase screen is defined as

follows

$$\boxed{\Phi_\phi(\boldsymbol{\kappa}) = 2\pi k^2 z \Phi_n(\boldsymbol{\kappa}, \kappa_z = 0)}. \quad (1.44)$$

Since refractive-index fluctuations can be assumed to be a Gaussian random field [40], and the phase screen ϕ is a linear map of this field (see Eq. (1.40)), the phase screen itself is Gaussian. In this case, the power spectral density function Φ_ϕ fully characterizes the phase screen.

Multiple phase screens. The split-step operator enables an approximation of the output field that is accurate up to second order in the propagation distance, which improves upon the linear accuracy obtained from a direct exponential splitting. However, when the field is propagated over the full distance L in a single step, the truncation error scales as $\mathcal{O}(L^3)$. This limits the accuracy of the approximation for extended paths.

This accuracy can be improved by partitioning the propagation distance into M sub-intervals of length $\Delta z = L/M$ and applying the split-step operator to each slab. Because both the free-space propagation operator and the phase-modulation operator are unitary, they preserve the field norm, and numerical errors therefore accumulate additively rather than multiplicatively. Consequently, the global error scales as $\mathcal{O}(M\Delta z^3) = \mathcal{O}(L^3/M^2)$. This quadratic reduction of the error as the number of phase screens M increases enables the multi-screen approach to more accurately approximate the continuous integration of turbulent fluctuations along the propagation path.

Basic method of phase-screen generation. For the numerical generation of phase screens, it is common to employ the Fourier-Stieltjes decomposition (see Eq. (1.12)). This simplifies the problem because, instead of directly sampling

spatially correlated random variables, we need to sample independent random variables corresponding to spectral modes. In this section, we describe the widely used method for phase-screen generation [46] utilized in classical optics in a turbulent atmosphere and discuss its limitations.

The approach originates from the necessity to employ the Fast Fourier Transform (FFT) [82]—a highly optimized algorithm for computing Fourier transforms—in order to accelerate the numerical transformation of spectral mode samples into spatial variables. This imposes a constraint that the spatial coordinates and the spectral modes must be defined on a rectangular grid of size $N \times N$ as

$$\mathbf{r}_{nm} = (n\Delta x, m\Delta x) \quad n = -\frac{N}{2}, \dots, \frac{N}{2} - 1, \quad m = -\frac{N}{2}, \dots, \frac{N}{2} - 1, \quad (1.45)$$

where L is the spatial size of the phase screen, $\Delta x = L/N$ is the spatial grid sampling spacing, and

$$\boldsymbol{\kappa}_{pq} = (p\Delta\kappa, q\Delta\kappa) \quad p = -\frac{N}{2}, \dots, \frac{N}{2} - 1, \quad q = -\frac{N}{2}, \dots, \frac{N}{2} - 1, \quad (1.46)$$

where $\Delta\kappa = \frac{2\pi}{L}$ is the spectral grid sampling spacing. The phase screen is then approximated as

$$\phi(\mathbf{r}_{nm}) \approx \sum_{p=-N/2}^{N/2-1} \sum_{q=-N/2}^{N/2-1} a_{pq} e^{i\boldsymbol{\kappa}_{pq} \cdot \mathbf{r}_{nm}}, \quad (1.47)$$

where the spectral coefficients a_{pq} are sampled as independent zero-mean complex Gaussian random variables $a_{pq} \sim \mathcal{CN}(0, \Phi_\phi(\boldsymbol{\kappa}_{pq})(\Delta\kappa)^2)$ and must satisfy the Hermitian symmetry property $a_{pq}^* = a_{-p-q}$ in order to produce a real-valued phase screen.

The parameters of the grid L and N must be chosen carefully as they determine the minimal and maximal spatial frequencies that can be represented. According

to the Nyquist-Shannon sampling theorem [83], the highest spatial frequency that can be resolved is $\kappa_{\text{Nyquist}} = N\Delta\kappa/2$. This imposes the limitation that the spatial sampling step $\Delta x = L/N \lesssim l_0/2$, where l_0 is the inner scale of the turbulence (see Section 1.4.2). On the other hand, the lowest spectral component of interest is of the order of $2\pi/L_0$, where L_0 is the outer scale of the turbulence. This leads to the requirement $\Delta\kappa \lesssim 2\pi/L_0$, which is practically impossible to satisfy with current computational resources. For example, for the typical values $l_0 \sim 3\text{mm}$ and $L_0 \sim 80\text{m}$, the required grid parameters are $L = 80\text{m}$ and $N \sim 5 \times 10^4$. Consequently, in practical simulations the grid size L is usually chosen to be several times larger than the beam diameter in order to avoid boundary effects and ensure that the wavefront distortions are fully contained within the computational window. The grid resolution N is then selected as a compromise between accurately representing small-scale fluctuations and maintaining a feasible computational cost. The accuracy of the chosen parameters can be verified by comparing the simulated phase structure function $D_\phi(\rho)$ (see Eq. (1.10)) with its theoretical form. This comparison reveals that the method often exhibits a known undersampling effect at lower frequencies (larger spatial distances). We will provide a detailed analysis and verification of this phenomenon in Section 1.4.5. Thus, this method requires certain corrections to be suitable for practical use.

Subharmonic method. There are a number of approaches that attempt to improve sampling in the low-frequency domain. One approach to compensate for missing low-frequency components in generated phase screens is the subharmonic method, as described by Lane et al. [84]. This method introduces additional low-frequency components by explicitly adding random Fourier modes in the undersampled spectral region $[-\Delta\kappa, \Delta\kappa]^2$. Typically, the corresponding low-frequency phase screen is very small, e.g., 3×3 points. The resulting low-frequency phase screen is added to the main phase screen.

To further increase the effective screen size, the same procedure can be applied recursively to the low-frequency screen in the region $[-\Delta\kappa/3, \Delta\kappa/3]^2$. This introduces additional large-scale components corresponding to a larger spatial period. Repeating this procedure d times yields a phase screen with an effective size of $3^d L$, progressively capturing increasingly larger turbulence scales.

While the subharmonic correction method drastically improves the representation of low-frequency statistics compared to the basic method, the resulting structure function is not close enough to the theoretical one for practical orders of subharmonics (see [Section 1.4.5](#)). Moreover, using a fixed rectangular grid for spectral modes introduces biased statistics, which does not match the continuous nature of atmospheric turbulence spectra. These factors, combined with the significant improvements in computational performance over recent decades, have motivated the development of new methods that move beyond the basic method of phase-screen generation.

There is also an alternative class of methods utilizing Zernike polynomial expansions to represent large-scale wavefront distortions [85, 86]. Since Zernike modes correspond directly to classical optical aberrations such as tip, tilt, and focus, they are naturally suited for augmenting the low-frequency content of FFT-generated screens. A recent approach [bachmann2025] provides a systematic framework for hybrid Zernike-FFT phase screen generation. This approach moves beyond empirical blending, providing a hybrid method to achieve a closer match to the theoretical structure functions.

Sparse-spectrum method. The sparse-spectrum method, introduced by Charnotskii in 2013 [87], moves away from the Fast Fourier Transform method for phase-screen generation, thus allowing arbitrary spectral components. Moreover, for each realization of a phase screen, these spectral components are randomly chosen. With proper sampling of spectral modes and their amplitudes, this method perfectly

reproduces the required structure function of the phase screen.

Similar to the basic method, a phase screen $\phi(\mathbf{r})$ is represented as a sum of a finite number of independent harmonic oscillators

$$\phi(\mathbf{r}) = \text{Re} \sum_{n=1}^N a_n e^{i\boldsymbol{\kappa}_n \mathbf{r}}, \quad (1.48)$$

where the spectral coefficients a_n are sampled as zero-mean independent complex Gaussian random variables with $\langle |a_n|^2 \rangle = s_n$, and $\boldsymbol{\kappa}_n$ are random variables with probability distribution $p_n(\boldsymbol{\kappa})$. The real part is taken because of the relaxation of the Hermitian symmetry restriction on the a_n coefficients.

Comparing the structure function of the phase screen generated with [Eq. \(1.48\)](#) and the targeted

$$\begin{aligned} D_\phi(\boldsymbol{\rho}) &= \left\langle (\phi(\mathbf{r} + \boldsymbol{\rho}) - \phi(\mathbf{r}))^2 \right\rangle_{\{a_n, \boldsymbol{\kappa}_n\}} = \\ &= \iint d^2\boldsymbol{\kappa} \sum_{n=1}^N s_n p_n(\boldsymbol{\kappa}) (1 - \cos(\boldsymbol{\kappa} \mathbf{r})) \equiv 2 \iint d^2\boldsymbol{\kappa} \Phi_\phi(\boldsymbol{\kappa}) (1 - \cos(\boldsymbol{\kappa} \mathbf{r})) \end{aligned} \quad (1.49)$$

leads to the following constraint

$$\sum_{n=1}^N s_n p_n(\boldsymbol{\kappa}) = 2\Phi_\phi(\boldsymbol{\kappa}). \quad (1.50)$$

Satisfying this single constraint yields the target spectral density, allowing for an arbitrary selection of $\boldsymbol{\kappa}_n$ distributions. For example, this generalization reduces to the basic phase-screen method when $p_n(\boldsymbol{\kappa})$ are delta functions at the nodes of the rectangular grid. Considering the rotational symmetry of $\Phi_\phi(\boldsymbol{\kappa})$ and its logarithmic scale, it looks natural to sample the modes uniformly in logarithmic, rotationally symmetric coordinates. In addition, for such a log-uniform partitioning,

it was shown that a statistic higher than the structure function—the two-point fourth moment—corresponds to the desired Gaussian statistics [88].

To simplify computation, let us split the spectral space into N non-overlapping rings and assign the distribution domain of each $\kappa_n, n = 1 \dots N$ to a single ring $K_{n-1} < \kappa < K_n$, where

$$K_n = K_{\min} \exp \left[\frac{n}{N} \ln \left(\frac{K_{\max}}{K_{\min}} \right) \right]. \quad (1.51)$$

K_{\min} and K_{\max} are the spectral range bounds. Typical values are $K_{\min} = \kappa_0$ and $K_{\max} = 2\kappa_m$ (see [Section 1.4.2](#)). With such a non-overlapping partition, we integrate [Eq. \(1.50\)](#) for each ring and obtain that

$$s_n = 4\pi \int_{K_{n-1}}^{K_n} d\kappa \kappa \Phi_\phi(\kappa) \quad (1.52)$$

where $p_n(\kappa) = 2\Phi_\phi(\kappa)s_n^{-1}$. To simplify computation, we can approximate the distributions of κ_n with uniform distributions on the corresponding rings. This means that for each realization of the phase screen, we sample κ_n as follows

$$|\kappa_n| = \sqrt{K_{n-1}^2 + \xi_n(K_n^2 - K_{n-1}^2)}, \quad (1.53)$$

where $\xi_n \in [0, 1]$ are uniform i.i.d. random variables, and the polar angles are uniform i.i.d random variables on $[0, 2\pi]$.

As a result, the sparse-spectrum method provides an approach to generate phase screens with an unbiased structure function in general, and with minimal discrepancy compared to the approximation of uniform sampling on rings, as will be verified in [Section 1.4.5](#). Despite the direct summation of modes instead of a Fast Fourier transform, the computational performance is comparable to the basic method because of the smaller number of modes. Because of random sampling of

modes, it is even possible to achieve an unbiased structure function with $N = 1$. But for better high-order statistics [88], the typical value is $N \sim 500$, compared to the value of $\sim 500^2$ for the basic method.

Another key advantage of this approach is the independence between the spatial grid and the choice of spectral modes. In the basic method, one parameter determines the other, which restricts the size of generated phase screens to only a few meters. In contrast, the sparse-spectrum method enables the generation of arbitrarily long phase screens while preserving the correct statistical properties. This, in turn, makes it possible to investigate time-dependent effects in the propagation of quantum light through a turbulent atmosphere.

1.4.5 Verification

Physical validity of the results requires verification of the numerical framework. In split-step propagation with phase screens, the dominant source of error is commonly attributed to the phase-screen generation itself. The central concern is whether the generated phase screens reproduce the prescribed turbulence statistics over the relevant spatial scales.

In our work, this issue is addressed by using the sparse-spectrum technique. Figure 1.3 compares the phase structure function (see Eq. (1.10)) obtained from phase screens generated by pure FFT, by the commonly used subharmonics method, and by the sparse-spectrum method (see Section 1.4.4) against the theoretical structure function of the modified von Kármán spectrum (see Eq. (1.19)). The sparse-spectrum phase screens exhibit quantitative agreement with the theoretical structure function across the full spatial range. Such agreement persists even for longer phase screens where the structure function approaches saturation. It is evident that the quality of the agreement depends on the choice of the low-frequency and high-frequency cutoffs K_{\min} and K_{\max} . The heuristic proposed in the original sparse-spectrum formulation [87] to set $K_{\min} = 1/(15L_0)$ and $K_{\max} = 2/\ell_0$ provides adequate accuracy across

the range of realistic turbulence conditions considered here.

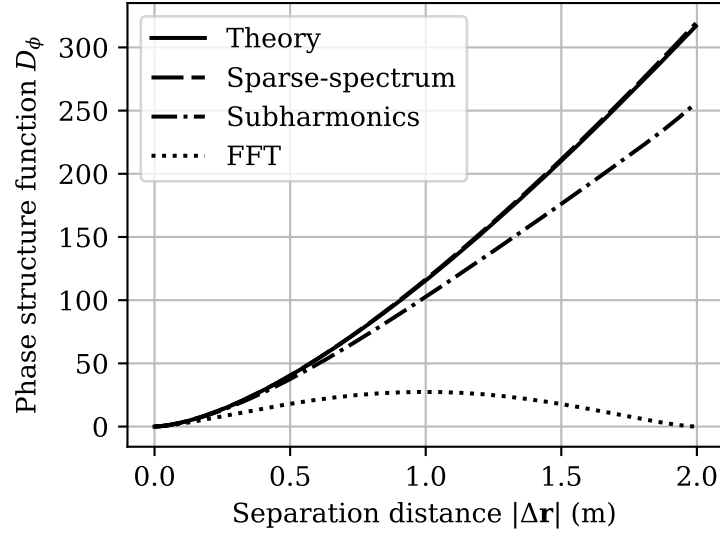


Figure 1.3 – Comparison of phase structure functions for phase screens generated by FFT, subharmonics method with six subharmonics, and sparse-spectrum methods against the theoretical structure function with modified von Kármán spectrum.

Once the phase-screen generation is validated, the simulation geometry must be chosen consistently for the particular propagation channel. Finer spatial and longitudinal resolutions generally improve accuracy, but they are constrained by computational cost. Consequently, all simulations are preceded by a convergence analysis. The dependence of the quantities of interest on transverse grid resolution, longitudinal discretization with phase screens, and sampling size is analyzed until the results reach a stable plateau. The corresponding parameters are then fixed at values beyond which further refinement produces no measurable change.

For weak and strong turbulence regimes where analytical expressions exist, additional verification is performed. Beam shape parameters such as W_{LT} (see Eq. (1.30)) and S_{BW} (see Eq. (1.31)) are compared against analytical predictions [31]. In particular, the limit $C_n^2 = 0$ is examined, where the numerical model must recover free-space propagation. Furthermore, basic physical consistency is enforced. Total intensity is conserved during propagation, and aliasing is excluded by ensuring that the beam footprint remains well within the computational grid at all propagation distances, thereby preventing wrap-around at the grid boundaries.

There also exist several practical conditions and heuristics that constrain the discretization. The transverse grid spacing must satisfy the Nyquist condition $\Delta x < \ell_0/2$ to resolve the inner scale of turbulence. The transverse grid size is chosen sufficiently large to prevent aliasing of the diffracting field. The longitudinal discretization, determined by the number of phase screens, is chosen such that the Rytov parameter associated with the interscreen distance does not exceed 0.1 [45, 47]. The interscreen distance must also exceed the outer scale of turbulence L_0 to satisfy the Markov approximation introduced in Eq. (1.42).

For all channels studied in this work, these verification steps are carried out. The practical conditions and heuristics are satisfied with a substantial margin. Convergence of the method is verified by increasing the number of phase screens until the beam statistics and the PDT statistics reach a stable plateau. This behavior indicates that discretization errors are minimal and that the numerical propagation faithfully represents the theoretical description of wave propagation through atmospheric turbulence.

2 Validation of analytical models

The reliability of any free-space quantum protocol analysis depends on the accuracy of the PDT. Any inaccuracies in the PDT modelling inevitably lead to inaccurate estimations of the quantum states at the receiver. Consequently, rigorous validation of these models is essential to ensure that predictions of models provide accurate results. This section addresses these challenges by providing a comparative analysis of the analytical PDT against numerical simulations, presenting the results published in our work [\[I\]](#).

Several analytical models of the PDT have been proposed (see [Section 1.3.1](#)). The earliest approach adopts statistical models of optical intensity fluctuations from classical optics. Since the transmittance is bounded by unity, events exceeding one must be discarded. This leads to the truncated lognormal model. A second class of models is based on a phenomenological description of the beam in the receiver aperture plane. The beam centroid is assumed to undergo two-dimensional Gaussian wandering. Under a fixed-size circular beam approximation, this yields the beam-wandering model. By introducing additional assumptions on elliptical-beam deformation, the elliptical-beam model provides an improved description of atmospheric quantum channels. A later model assumes statistical independence between beam wandering and beam shape deformations. These effects are combined to construct the total probability PDT model.

There remains significant uncertainty regarding the physical regimes in which these models are applicable. The lognormal distribution of the optical field is derived within the weak turbulence Rytov approximation. Nevertheless, the truncated lognormal models has been reported to fit experimental data obtained under strong turbulence conditions [\[59\]](#). Beam wandering is a pronounced feature of light propagation through weak turbulence and the beam-wandering model is therefore commonly associated with this regime. The elliptical-beam model is reported to reproduce experimental data under weak to moderate turbulence. This

turbulence-based classification is incomplete, which motivates a more systematic analysis of model applicability.

In this section, numerical simulations of atmospheric channels are performed for three different turbulence conditions, which are characterized by the value of the Rytov parameter $\sigma_R^2 = 1.23 C_n^2 k^{7/6} z_{\text{ap}}^{11/6}$. The results are used to validate existing analytical models and to identify their ranges of applicability. Model comparison is carried out using the Kolmogorov-Smirnov (KS) statistic [89], defined as

$$D_M = \sup_{\eta} |F_M(\eta) - F(\eta)|, \quad (2.1)$$

where $F(\eta)$ is the cumulative distribution function of the analytical model and $F_M(\eta)$ denotes the empirical distribution function obtained from simulation

$$F_M(\eta) = \frac{1}{M} \sum_{i=1}^M \theta(\eta - \eta_i), \quad (2.2)$$

where M is the sample size, $\theta(\eta)$ is the Heaviside step function. The goal is to determine which model performs best in a given scenario rather than to perform formal hypothesis testing. The Kolmogorov-Smirnov statistic therefore provides a simple and sufficient metric. It directly quantifies discrepancies between cumulative distributions, which is especially relevant for tasks where tail probabilities such as exceedance $1 - F(\eta)$ determine system performance [62].

Existing analytical models are typically parametrized by quantities derived from second- and fourth-order field correlation functions Γ_2 and Γ_4 (see [Section 1.4.3](#)) in the aperture plane. In particular, the first and second moments of the transmittance $\langle \eta \rangle$ and $\langle \eta^2 \rangle$ can be obtained from the field correlation functions and can be easily estimated from experimental data. Beam shape parameters such as long-term beam-spot radius, short-term beam-spot radius, beam-wandering variance, and beam size fluctuations require more involved measurements but remain

experimentally accessible.

In theoretical analyses, deriving the correlation functions in terms of channel parameters such as the refractive index structure constant, inner and outer scales, and propagation distance requires restrictive approximations that become impractical in moderate to strong turbulence. This leads to additional error in the PDT when it is inferred from the channel parameters. To isolate the performance of the PDT models from these analytical approximations, this work estimates all model parameters directly from phase-screen simulations. This approach provides unbiased parameter estimation and enables the validation of analytical models independently of external parameter errors.

2.1 Results and discussion

2.1.1 Weak channel

We consider a weak turbulence channel with Rytov parameter $\sigma_R^2 = 0.2$. Physical and numerical parameters are listed in [Table 2.1](#). Two initial beam curvatures are examined. The first case uses $F_0 = +\infty$ and corresponds to a collimated beam. The second case uses $F_0 = z_{\text{ap}}$ and corresponds to a geometrically focused beam that minimizes the beam radius at the aperture plane in the absence of turbulence [31].

Table 2.1 – Weak turbulence channel parameters ($\sigma_R^2 = 0.2$).

Physical Parameter	Symbol	Value	Numerical Setting	Value
Channel length	z_{ap}	1 km	Phase screens	10
Structure constant	C_n^2	5×10^{-15}	Grid size	512×512
Inner scale	ℓ_0	1 mm	Spatial step	0.3 mm
Outer scale	L_0	80 m	Spectral rings	1024
Wavelength	λ	809 nm	Interscreen Rytov parameter	3×10^{-3}
Beam radius	W_0	2 cm	Sample size	10^5

Collimated beam. For the collimated beam with $F_0 = +\infty$, the Kolmogorov-Smirnov statistics comparing analytical models to the numerical PDT are shown in Fig. 2.1. The vertical axis is plotted on a logarithmic scale, such that equal visual separations correspond to order-of-magnitude differences in the actual KS distance. Despite their direct physical motivation, the beam-wandering and elliptical-beam models exhibit the poorest agreement with the numerical distributions across most aperture sizes. The elliptical-beam model nevertheless displays pronounced minima of the KS statistic when the aperture radius slightly exceeds the long-term beam radius.

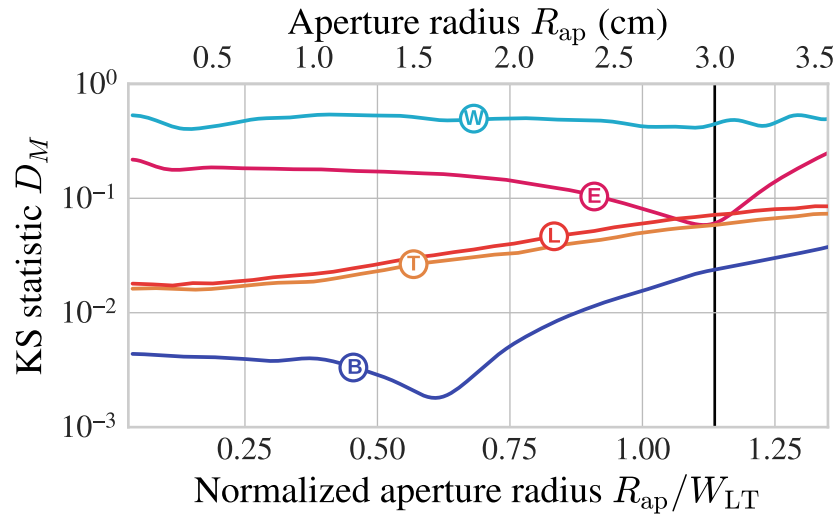


Figure 2.1 – Kolmogorov-Smirnov (KS) statistic D_M as a function of the aperture radius for a collimated beam $F_0 = \infty$ in a weak turbulence channel ($\sigma_R^2 = 0.2$). The performance of the beam-wandering (W), elliptical-beam (E), truncated lognormal (L), total probability (T), and Beta distribution (B) models are compared against numerical simulation data. The vertical line indicates the aperture radius ($R_{ap} = 3$ cm) where the elliptical-beam model achieves its minimum KS distance.

The truncated lognormal model reproduces the numerical transmittance distribution reasonably well. Its accuracy degrades as the aperture radius increases because the numerical distribution changes its skewness from positive to negative values, while the truncated lognormal distribution remains positively skewed for any choice of parameters. The total probability model performs nearly identically to the

underlying lognormal distribution in this regime, which contradicts the interpretation that beam wandering plays a dominant role in shaping transmittance statistics under weak turbulence.

Among all considered models, the Beta distribution yields the best overall agreement. Its KS statistic reaches a minimum near $\langle \eta \rangle \approx 0.5$, where the numerical PDT is close to symmetric. This behavior is consistent with the flexibility of the Beta distribution in interpolating between positively and negatively skewed shapes.

At the aperture corresponding to the KS minimum of the elliptical-beam model, the mode of this analytical distribution coincides with the mode of the numerical distribution, as shown in Fig. 2.2. This aperture is indicated by the vertical line in Fig. 2.1. For other aperture sizes, the elliptical-beam model exhibits biased values of both the mode and the mean transmittance $\langle \eta \rangle$.

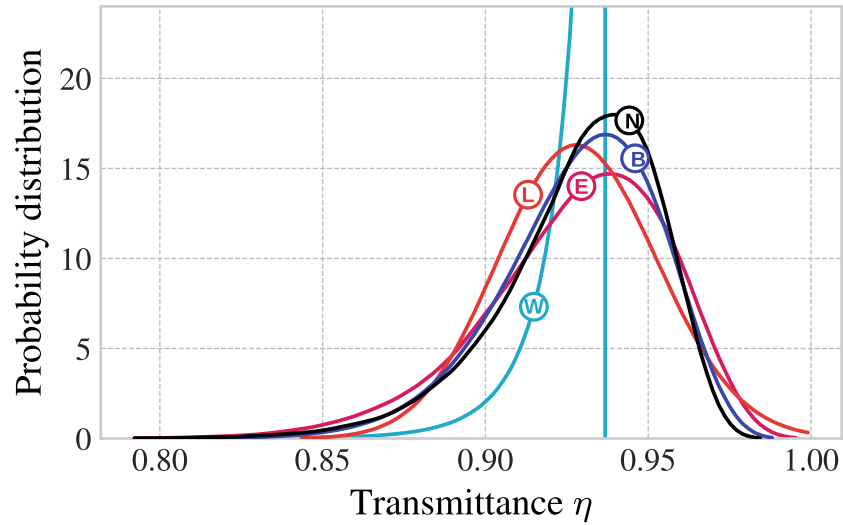


Figure 2.2 – PDT for a collimated beam $F_0 = \infty$ in a weak turbulence channel ($\sigma_R^2 = 0.2$) with an aperture radius of $R_{ap} = 3$ cm. The numerical simulation (N) is compared with the beam-wandering (W), truncated lognormal (L), elliptical-beam (E), and Beta distribution (B) models.

The beam-wandering model assumes a fixed circular beam profile, which implies that the transmittance cannot exceed that of a perfectly coaxial beam. This constraint manifests as a sharp cutoff of the right tail of the distribution and prevents the model from reproducing the high transmittance events observed numerically.

Overall, under weak turbulence the transmittance fluctuations remain small, and for $0 \ll \langle \eta \rangle \ll 1$ the numerical distributions approach a quasi-Gaussian shape.

Focused beam. For the focused configuration with $F_0 = z_{\text{ap}}$, the KS statistics are shown in Fig. 2.3. All analytical models demonstrate systematically poorer agreement with numerical probability distributions compared to the collimated case. This deterioration should not be interpreted as reduced channel performance. A focused beam produces a smaller spot at the aperture plane and therefore achieves a higher average transmittance for the same aperture radius, which improves link efficiency. The larger KS values instead indicate that existing analytical models do not adequately capture the more complex field statistics.

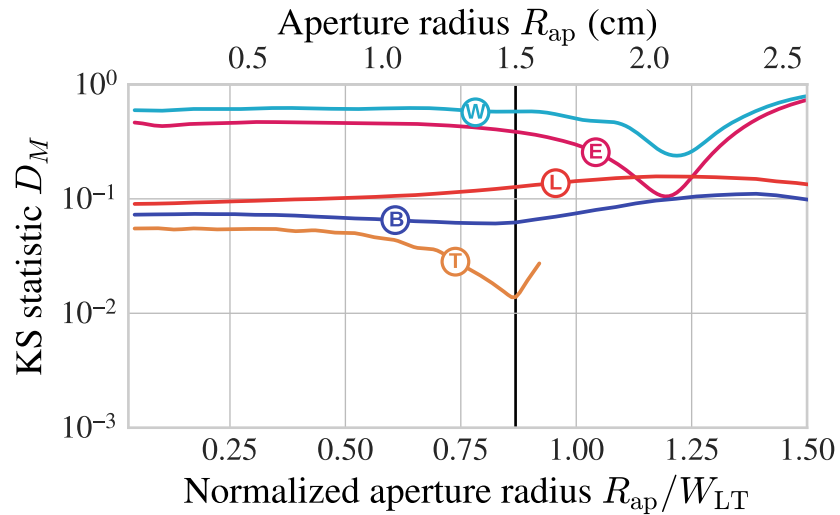


Figure 2.3 – Kolmogorov-Smirnov (KS) statistic D_M as a function of the aperture radius for a focused beam ($F_0 = z_{\text{ap}}$) in a weak turbulence channel ($\sigma_R^2 = 0.2$). The performance of the beam-wandering (W), elliptical-beam (E), truncated lognormal (L), total probability (T), and Beta distribution (B) models are compared against numerical simulation data. The vertical line indicates the aperture radius ($R_{\text{ap}} = 1.5$ cm) where the total probability model achieves its minimum KS distance.

Among all considered models, the total probability model provides the best overall agreement for small and moderate aperture radii. However, when the aperture radius satisfies $R_{\text{ap}} \gtrsim W_{\text{LT}}$, the model is no longer defined. In this domain, the Beta

distribution yields the smallest KS distance among the remaining models.

The numerical and analytical PDTs corresponding to the minima of the total probability model are shown in Fig. 2.4. The truncated lognormal distribution exhibits an incorrect skewness and an unphysical finite probability density at $\eta = 1$, which arises from the imposed truncation. The elliptical-beam model again shows biased estimates of both the mode and the mean transmittance.

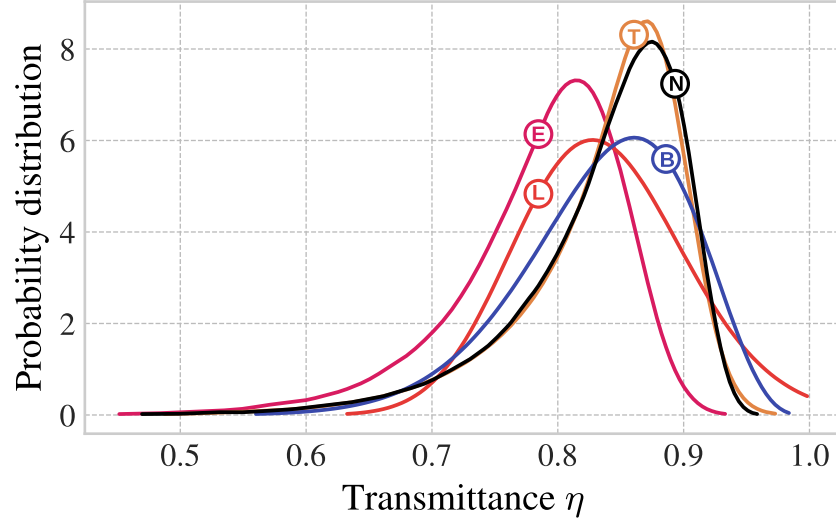


Figure 2.4 – PDT for a focused beam ($F_0 = z_{\text{ap}}$) with an aperture radius of $R_{\text{ap}} = 1.5$ cm in a weak turbulence channel ($\sigma_R^2 = 0.2$). The numerical simulation (N) is compared with the truncated lognormal (L), elliptical-beam (E), total probability (T) and Beta distribution (B) models.

The Beta distribution, while matching the first two moments by construction, underestimates higher-order moments such as skewness and kurtosis. In the focused beam weak turbulence regime, the total probability approach provides the closest overall agreement with the numerical results. However, when the total probability model is not applicable, the Beta distribution yields the best agreement among the remaining analytical models.

2.1.2 Moderate channel

We next consider a moderate turbulence channel with Rytov parameter $\sigma_R^2 = 1.5$. This regime corresponds to realistic atmospheric conditions for the horizontal

atmospheric channel in Erlangen, Germany [90, 91]. The physical and numerical parameters used in the simulations are summarized in Table 2.2.

Table 2.2 – Moderate turbulence channel parameters ($\sigma_R^2 = 1.5$).

Physical Parameter	Symbol	Value	Numerical Setting	Value
Channel length	z_{ap}	1.6 km	Phase screens	10
Structure constant	C_n^2	1.5×10^{-14}	Grid size	512×512
Inner scale	ℓ_0	1 mm	Spatial step	0.4 mm
Outer scale	L_0	80 m	Spectral rings	1024
Wavelength	λ	809 nm	Interscreen Rytov parameter	2.2×10^{-2}
Beam radius	W_0	2 cm	Sample size	10^5

Collimated Beam. For the collimated configuration with $F_0 = +\infty$, the Kolmogorov-Smirnov statistics comparing analytical models to numerical transmittance distributions are shown in Fig. 2.5. The overall behavior is qualitatively similar to the weak turbulence case. For small aperture radii, the Beta distribution provides the best agreement with the numerical PDT. As the aperture increases, its performance gradually degrades.

As seen in the left panel of Fig. 2.6, the Beta model accurately reproduces the overall shape of the numerical distribution in this regime. In contrast, the truncated lognormal model produces a systematically narrower distribution, despite being parametrized using the first two moments. This bias arises because truncation alters the effective moments of the distribution, while the fitted parameters correspond to the underlying untruncated lognormal. An additional contribution may come from mismatched higher-order statistics, in particular the kurtosis.

At aperture radii $R_{\text{ap}} \approx W_{\text{LT}}$, the total probability model outperforms all other approaches as seen in Fig. 2.5 and the right panel of Fig. 2.6. In this range, the modes of the beam-wandering and elliptical-beam models coincide with the mode of the numerical distribution, which leads to pronounced minima of the KS statistic for these models. The Beta distribution, although accurate in mean and variance, underestimates the kurtosis in this regime, which limits its performance compared

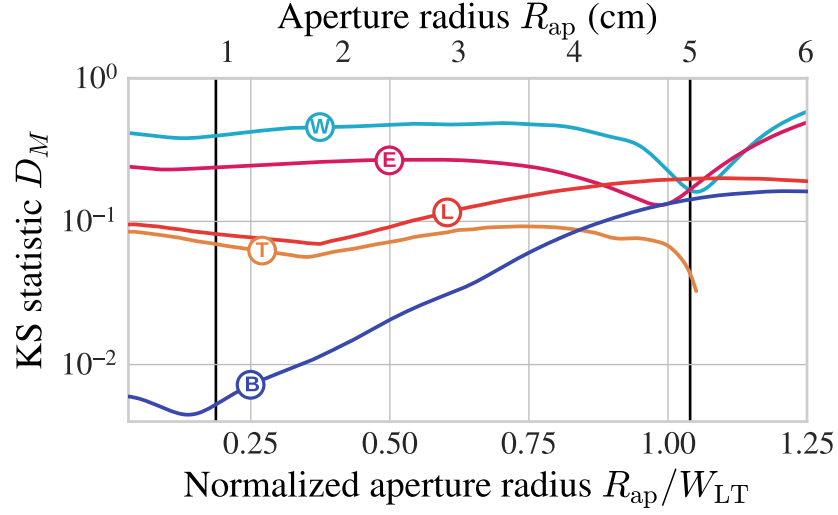


Figure 2.5 – Kolmogorov-Smirnov statistic D_M as a function of the aperture radius for a collimated beam ($F_0 = \infty$) in a moderate turbulence channel ($\sigma_R^2 = 1.5$). The performance of the beam-wandering (W), elliptical-beam (E), truncated lognormal (L), total probability (T), and Beta distribution (B) models are compared against numerical simulation data.

to the total probability model.

Focused Beam. For the focused configuration with $F_0 = z_{\text{ap}}$, the KS statistics are shown in Fig. 2.7. As in the weak turbulence channel, focusing leads to systematically poorer agreement between analytical models and numerical results compared to the collimated case. The Beta distribution again provides the best overall performance across most aperture sizes. Near $R_{\text{ap}} \approx W_{\text{LT}}$, the total probability model slightly outperforms the Beta distribution. At apertures where the modes of the beam-wandering and elliptical-beam models coincide with the numerical mode, these models temporarily achieve their best agreement.

The underlying reason for the generally worse performance of all analytical models is illustrated in Fig. 2.8. In this regime, the numerical probability distribution develops a strongly non-Gaussian plateau, with an extended interval of η over which the probability density remains approximately constant. Such a feature cannot be captured by any of the considered analytical models, all of which predict

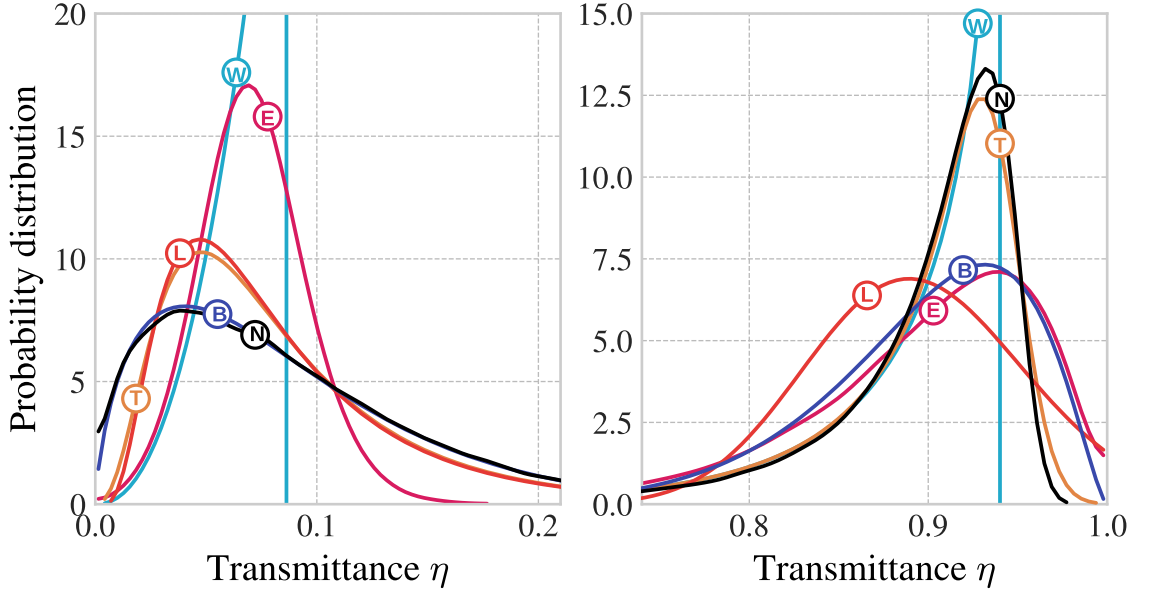


Figure 2.6 – PDT for a collimated beam in moderate turbulence at an aperture radius of $R_{\text{ap}} = 0.9$ cm (left panel) and $R_{\text{ap}} = 5$ cm (right panel). The beam-wandering (W), elliptical-beam (E), truncated lognormal (L), total probability (T), and Beta distribution (B) models and numerical simulation results (N).

smooth unimodal distributions with decaying tails. Overall, the agreement between analytical models and numerical results is worse in this regime than in the strong turbulence channel analyzed in the following section.

2.1.3 Strong channel

As the propagation distance increases, the difference between the spot sizes of a geometrically focused beam with $F_0 = z_{\text{ap}}$ and a collimated beam with $F_0 = +\infty$ becomes negligible at the aperture plane. Consequently, only the collimated configuration is considered in the strong turbulence regime. We analyze a strong turbulence channel characterized by the Rytov parameter $\sigma_R^2 = 33.3$. The corresponding physical and numerical parameters are listed in [Table 2.3](#).

The Kolmogorov-Smirnov statistics comparing analytical models to numerical transmittance distributions are shown in [Fig. 2.9](#). Even in this strong turbulence regime, the overall behavior resembles that observed in the previously considered regimes. However, this regime does reveal one particular feature.

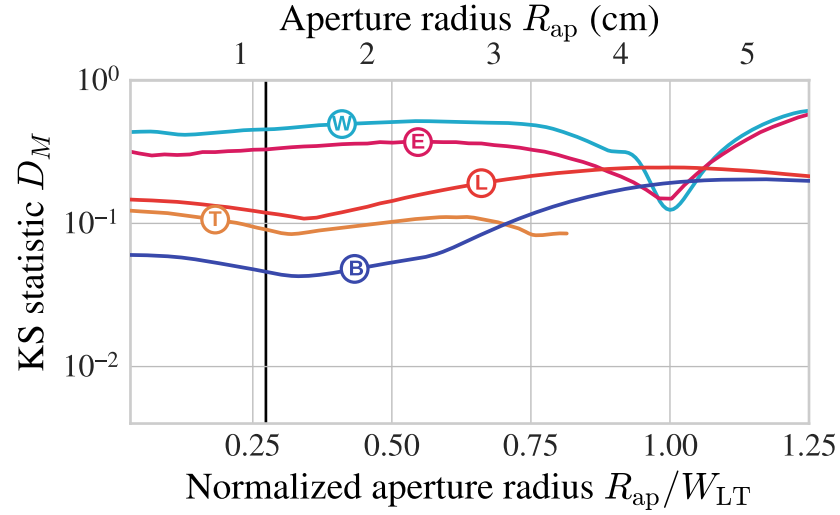


Figure 2.7 – Kolmogorov-Smirnov statistic D_M as a function of the aperture radius for a focused beam ($F_0 = z_{\text{ap}}$) in a moderate turbulence channel ($\sigma_R^2 = 1.5$). The performance of the beam-wandering (W), elliptical-beam (E), truncated lognormal (L), total probability (T), and Beta distribution (B) models are compared against numerical simulation data.

Table 2.3 – Strong turbulence channel parameters ($\sigma_R^2 = 33.3$).

Physical Parameter	Symbol	Value	Numerical Setting	Value
Channel length	z_{ap}	50 km	Phase screens	30
Structure constant	C_n^2	6×10^{-16}	Grid size	4096×4096
Inner scale	ℓ_0	1 mm	Spatial step	1 mm
Outer scale	L_0	80 m	Spectral rings	1024
Wavelength	λ	808 nm	Interscreen Rytov parameter	6.5×10^{-2}
Beam radius	W_0	6 cm	Sample size	10^5

The main qualitative difference appears at very small apertures $R_{\text{ap}} \lesssim 0.1W_{\text{LT}}$. In this range, the truncated lognormal model exhibits better agreement with the numerical results. This finding is illustrated in [Fig. 2.10](#).

As the ratio $R_{\text{ap}}/W_{\text{LT}} \rightarrow 0$, the aperture can be treated as point-like relative to both the overall beam size and the characteristic scintillation scale of the optical field. The transmittance distribution then approaches the probability distribution of irradiance at a point, rather than an aperture-averaged quantity. Point irradiance statistics in atmospheric turbulence have been studied extensively in classical atmospheric optics and are discussed in [Section 1.2.3](#). In this context, the lognormal

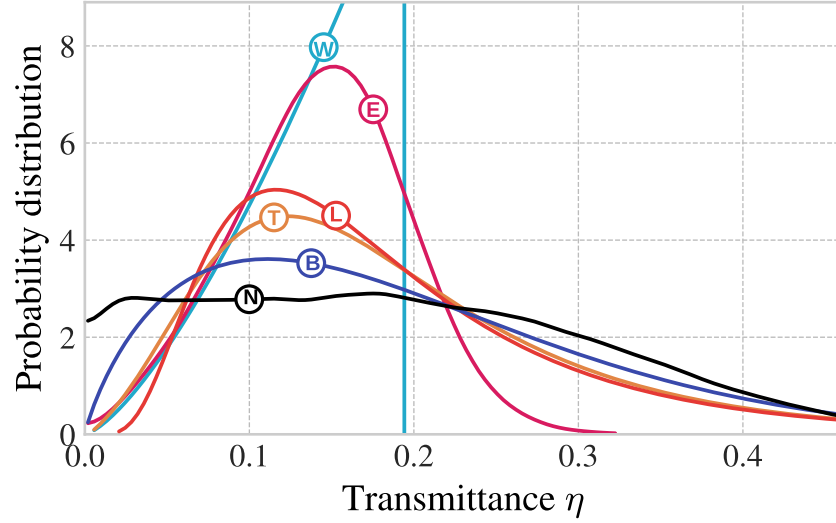


Figure 2.8 – PDT for a focused beam ($F_0 = z_{\text{ap}}$) with an aperture radius of $R_{\text{ap}} = 1.2$ cm in a moderate turbulence channel ($\sigma_R^2 = 1.5$). The numerical simulation (N) is compared with the truncated lognormal (L), beam-wandering (W), elliptical-beam (E), total probability (T) and Beta distribution (B) models.

distribution is a standard model, which explains the relatively good performance of the truncated lognormal model for very small apertures. For strong turbulence, other irradiance models such as the negative exponential, K-distribution, lognormal-Rician, or Gamma-Gamma distributions, as reviewed in [Section 1.2.3](#), may provide a more accurate description of PDT for the range of very small apertures.

2.1.4 Summary

For both weak turbulence channels and the moderate-turbulence collimated beam channel, the numerically obtained PDTs exhibit bell-like, unimodal, and relatively narrow distributions with noticeable asymmetry near the boundaries of the support, $\eta \in [0, 1]$. For the moderate-turbulence focused beam and strong turbulence channels, a similar overall tendency is observed, though the distributions become broader and tend toward a flattened shape. This feature indicates an increased spread of transmittance values caused by the more complex spatial structure of the beam.

The first important observation is that the physically motivated models (the beam-wandering model and the elliptical-beam model), which are defined in terms

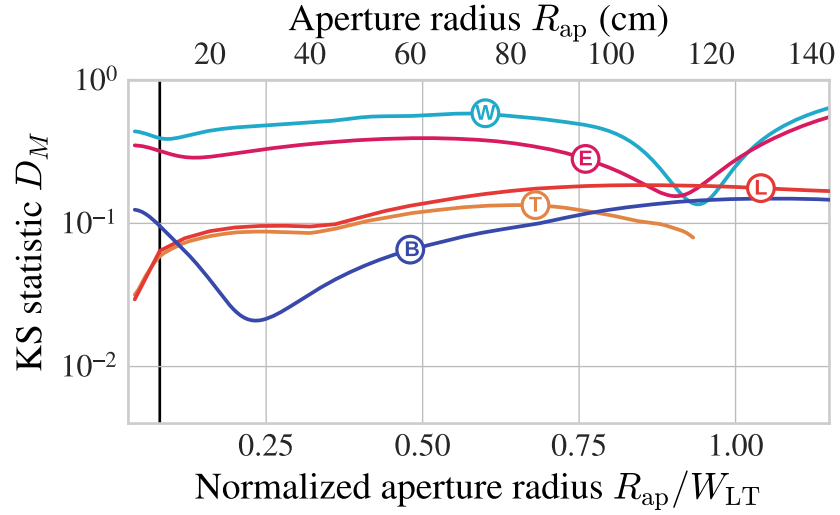


Figure 2.9 – Kolmogorov-Smirnov (KS) statistic D_M as a function of the aperture radius for a collimated beam $F_0 = \infty$ in a strong turbulence channel ($\sigma_R^2 = 33.3$). The performance of the beam-wandering (W), elliptical-beam (E), truncated lognormal (L), total probability (T), and Beta distribution (B) models are compared against numerical simulation data.

of the statistics of the beam-shape parameters, exhibit biased transmittance moments. This discrepancy arises because idealized circular or elliptical beam shapes fail to account for complex beam deformations. In some cases, these models reproduce the overall shape of the numerical PDT quite well (see Fig. 2.4), although their peaks are shifted relative to the numerical result. The best agreement in terms of the KS statistic is obtained when the peaks of the analytical and numerical PDTs coincide, as illustrated in Fig. 2.5. Thus, because of the inability to fully account for all orders of the beam shape decomposition, it is more appropriate to parameterize analytical models in terms of transmittance moments rather than beam shape statistics.

The second important observation concerns the dominant role of the aperture size in determining the applicability of different PDT models. The KS statistics show that the models' relative performance is similar across different turbulence strengths. In contrast, variations in the aperture radius cause significant changes in the KS statistic, indicating a strong dependence of model accuracy on the aperture parameter.

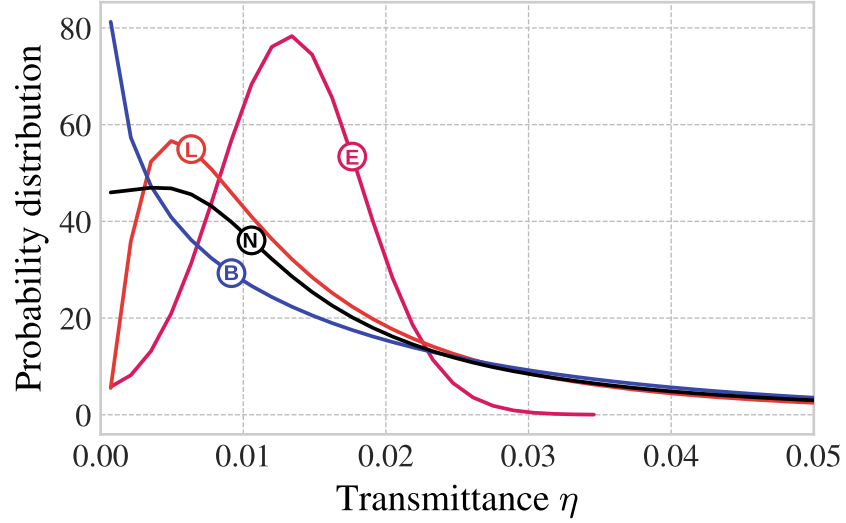


Figure 2.10 – PDT for a collimated beam $F_0 = \infty$ in a strong turbulence channel ($\sigma_R^2 = 33.3$) with an aperture radius of $R_{\text{ap}} = 10$ cm. The numerical simulation (N) is compared with the truncated lognormal (L), elliptical-beam (E), and Beta distribution (B) models.

Physically, increasing the turbulence strength primarily leads to a broader PDT (i.e., increased variance), which is captured reasonably well by all the analytical models. However, changing the aperture size mainly affects the skewness of the numerical PDT, and many analytical models fail to reproduce this asymmetry accurately. In particular, the lognormal model always yields positively skewed distributions, whereas the beam-wandering model consistently produces negatively skewed ones. The elliptical-beam model generally yields negative skewness, with only a minor positive skew for small apertures, which remains insufficient to reproduce the numerical PDT. Among the considered models, the total probability model and the Beta model most successfully reproduce the skewness of the numerical PDT.

Overall, across the entire parameter space examined, the analytical PDT models exhibit distinct strengths and weaknesses, which can be summarized as follows. The empirical Beta model generally exhibits the best performance according to the KS statistics, thanks to its naturally bounded support $\eta \in [0, 1]$ and its ability to reproduce the skewness near the boundary points. The lognormal model shows

decent performance, but it is generally inferior to the Beta model. An exception occurs for small apertures under strong turbulence, when the numerical PDT is broad and highly skewed. In this regime, the estimated parameters of the Beta model may result in an L-shaped form, and the lognormal model can outperform the Beta model.

The total probability model, which combines the positively skewed lognormal and negatively skewed beam-wandering models, performs similarly to the base lognormal model for small apertures. However, when the aperture size becomes comparable to the average beam spot width ($R_{\text{ap}} \lesssim W_{\text{LT}}$), the model captures the high kurtosis of the numerical PDT, allowing it to outperform other models in some narrow parameter ranges. The physically grounded beam-wandering and elliptical-beam models are strongly affected by bias in the first transmittance moments (mean and variance). This is the reason why they perform well when their parameters are fitted using least-squares methods (see [Section 1.3.1](#)), but poorly when the beam shape parameters are estimated directly from numerical simulations. However, when the peaks of the analytical and numerical PDTs are aligned, these models can outperform all others.

3 Statistical properties of the beam shape parameters

This analysis is based on results originally established in our work [1], specifically focusing on the statistical behavior of optical beam-shape parameters after propagation through a turbulent atmosphere. They form the core set of assumptions underlying physically motivated analytical models such as the beam-wandering model, the elliptical-beam model, and the total-probability framework. These assumptions include: the distribution of the beam-centroid position, the statistical independence between the beam-centroid position and the beam-spot shape, and the Gaussian statistics of the beam semiaxes. However, these assumptions are accepted without strong empirical support. This introduces a potential source of systematic inaccuracy. Therefore, it is essential to examine and validate these assumptions through numerical simulations.

3.1 Distribution of the beam-centroid position

Beam wandering is the most prominent effect experienced by a light beam propagating through a turbulent atmosphere. It arises primarily from large-scale turbulent eddies, which cause the entire beam spot to shift away from the propagation axis. This phenomenon is explicitly included in all three analytical models discussed above, where the beam-centroid displacement is assumed to follow a two-dimensional Gaussian distribution.

Empirical evidence supporting this Gaussian assumption is limited, as the number of realizations is generally small; see, e.g. Ref. [92]. Consequently, it does not allow confident estimation of higher-order moments, such as skewness or kurtosis, and it does not cover a wide range of turbulence strengths. To address this, we perform a systematic numerical study across several turbulence strengths.

Given the isotropy of turbulence, the distribution of the beam centroid

is radially symmetric. Consequently, it is sufficient to consider only a single-dimensional projection along the x -axis—the beam-centroid coordinate x_0 , defined as Eq. (1.29). To verify whether the distribution is Gaussian, we generate $5 \cdot 10^5$ realizations of beam propagation, compute the corresponding values of x_0 according to Eq. (1.29), and estimate the higher-order moments—the skewness and excess kurtosis [93]. These higher-order moments provide a quantitative measure of deviations from the Gaussian assumption: skewness captures asymmetry in the distribution, while excess kurtosis reflects the presence of heavy tails or peakedness. To systematically evaluate the effect of turbulence strength, we perform this analysis across a range of atmospheric conditions, spanning weak to strong turbulence. The same three types of propagation channels considered in Section 2 will be used to maintain consistency with previous analyses.

3.1.1 Weak turbulence channel

We begin with the weak-turbulence channel of propagation length $L = 1\text{km}$, characterized by a Rytov variance $\sigma_R^2 = 0.2$. The full set of channel parameters is listed in Table 2.1. For this channel, the distribution of the beam-centroid coordinate x_0 was estimated using a kernel density method for both the collimated and focused cases. The resulting probability density functions are shown in Fig. 3.1.

We estimated and plot a Gaussian probability density function for comparison. The simulated distribution exhibits an almost perfect match with this fitted curve. The numerical values of skewness and excess kurtosis, listed in Table 3.1, confirm this observation.

Table 3.1 – Results for skewness and excess kurtosis for weak channels.

Weak channel	Skewness	Excess kurtosis
Collimated $F = \infty$	0.0058	0.014
Focused $F = z_{\text{ap}}$	−0.0043	−0.0038

The skewness and excess kurtosis are effectively zero. These results indicate

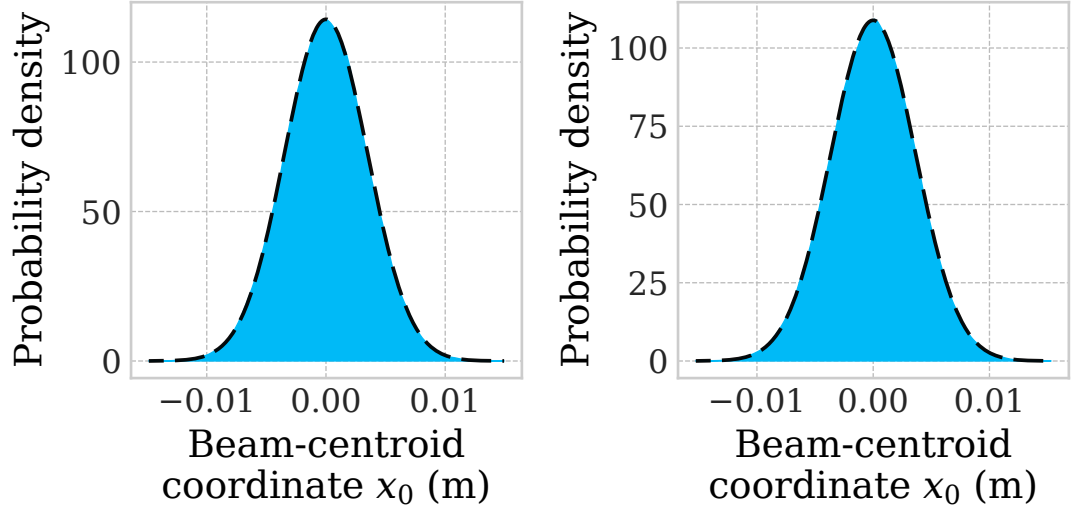


Figure 3.1 – Probability density function of the beam-centroid coordinate x_0 for a collimated and focused beam after propagation through a weak-turbulence channel ($\sigma_R^2 = 0.2$). The shaded areas represent the distributions estimated from $5 \cdot 10^5$ numerical realizations using kernel density estimation, while the dashed lines indicate the theoretical Gaussian distribution.

that, under weak turbulence, the beam-centroid displacement can be reliably modeled as a two-dimensional Gaussian random variable for both collimated and focused beams. This directly supports the standard assumption used in analytical models for the weak-turbulence regime.

3.1.2 Moderate turbulence channel

We next consider a stronger turbulence condition with propagation length $L = 1.6\text{km}$ and Rytov variance $\sigma_R^2 = 1.5$. The full set of channel parameters is given in [Table 2.2](#). The kernel-estimated probability density functions of the beam-centroid coordinate x_0 for both the collimated and focused beams are shown in [Fig. 3.2](#).

Both distributions remain very close to the Gaussian reference. In the focused case, the peak appears slightly asymmetric by visual inspection. However, the estimated skewness reported in [Table 3.2](#) is essentially zero, indicating that this deviation can be considered as statistical noise. In both cases, the skewness and

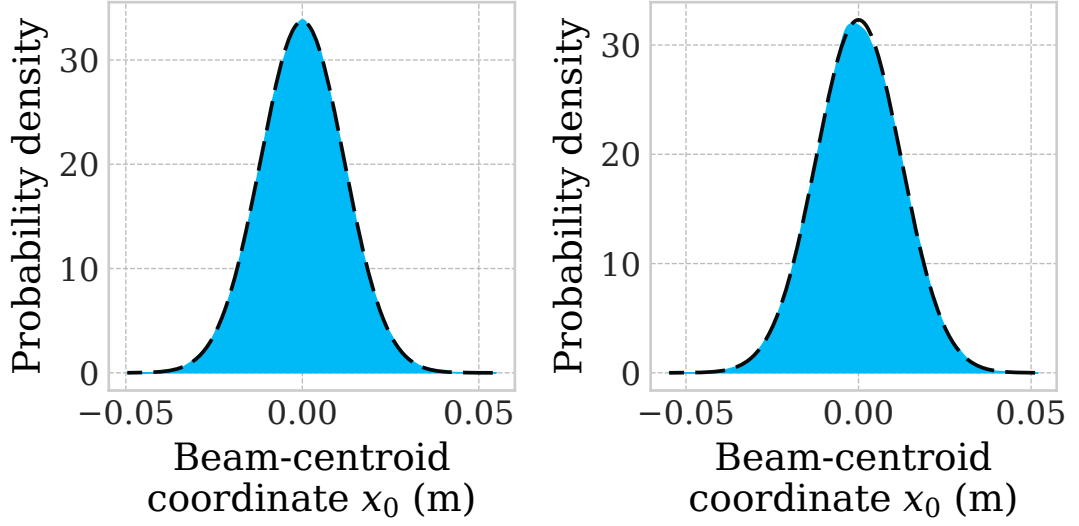


Figure 3.2 – Probability density function of the beam-centroid coordinate x_0 for a collimated and focused beam after propagation through a moderate-turbulence channel ($\sigma_R^2 = 1.5$). The shaded areas represent the distributions estimated from $5 \cdot 10^5$ numerical realizations using kernel density estimation, while the dashed lines indicate the theoretical Gaussian distribution.

excess kurtosis remain very small. Thus, even at moderate turbulence strength, the beam-centroid position continues to be well described by a two-dimensional Gaussian random variable.

Table 3.2 – Results for skewness and excess kurtosis for moderate channels.

Moderate channel	Skewness	Excess kurtosis
Collimated $F = \infty$	0.0172	−0.0046
Focused $F = z_{\text{ap}}$	−0.003	−0.0279

3.1.3 Strong turbulence channel

Finally, we consider the strong-turbulence channel with propagation length $L = 50\text{km}$ and Rytov variance $\sigma_R^2 = 33.3$. The full set of channel parameters is given in [Table 2.3](#). The kernel-estimated probability density function of the beam-centroid coordinate x_0 is shown in [Fig. 3.3](#).

The distribution remains approximately Gaussian. However, in this regime, a noticeable deviation appears near the peak of the distribution. This is reflected in

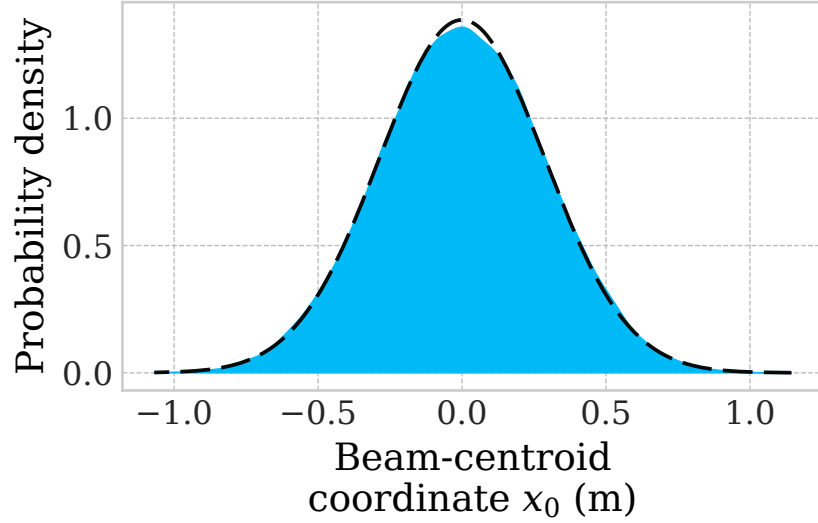


Figure 3.3 – Probability density function of the beam-centroid coordinate x_0 for a collimated beam after propagation through a strong-turbulence channel ($\sigma_R^2 = 33.3$). The shaded area represents the distributions estimated from $5 \cdot 10^5$ numerical realizations using kernel density estimation, while the dashed line indicates the theoretical Gaussian distribution.

the negative excess kurtosis (see [Table 3.3](#)).

Table 3.3 – Results for skewness and excess kurtosis for strong channel.

Strong channel	Skewness	Excess kurtosis
Collimated $F = \infty$	0.0008	−0.1064

The skewness is essentially zero, but the negative excess kurtosis indicates a slight platykurtic shape. This confirms a mild departure from Gaussianity at very strong turbulence conditions. However, the deviation is still modest, such that for most analytical purposes the Gaussian assumption remains sufficiently accurate even in this regime.

3.2 Quantifying the contribution of beam wandering to the PDT

Beam wandering is one of the dominant low-order turbulence-induced perturbations of an optical beam. It appears together with large-scale beam-shape

deformation and small-scale scintillation. This subsection investigates how beam wandering alone contributes to the transmittance.

Identifying regimes where beam wandering is the main driver of transmittance variability clarifies when analytical models that include this effect are more applicable and when more complex models are required. In addition, in practical free-space experiments, adaptive-optics systems are often used to mitigate random centroid displacement [94]. When the correlation between wandering and transmittance is high, such techniques can offer substantial performance improvements, emphasizing the practical relevance of this analysis for adaptive-optics applications.

To quantify the contribution of beam wandering, we compute the Pearson correlation coefficient between the centroid displacement r_0 and the transmittance η , defined as

$$S(r_0, \eta) = \frac{\langle \Delta r_0 \Delta \eta \rangle}{\sqrt{\langle \Delta r_0^2 \rangle \langle \Delta \eta^2 \rangle}}. \quad (3.1)$$

For every atmospheric channel listed in [Section 2](#) and for each aperture radius, we perform $5 \cdot 10^5$ independent beam-propagation simulations, compute $r_0 = \sqrt{x_0^2 + y_0^2}$, where x_0 is defined as [Eq. \(1.29\)](#) and y_0 is defined in the same way, evaluate transmittance η according to [Eq. \(1.25\)](#), and estimate $S(r_0, \eta)$ [Eq. \(3.1\)](#). The dependence of the correlation on the aperture radius is shown in [Fig. 3.4](#). Across all atmospheric channels, the correlation between centroid displacement and transmittance is negative, reflecting the obvious fact that larger beam wandering reduces received power. The magnitude of this correlation strongly depends on the ratio between the aperture radius and the long-term beam radius $R_{\text{ap}}/W_{\text{LT}}$.

For aperture radii much larger than W_{LT} , almost the full beam enters the receiver aperture regardless of its displacement. The correlation in this case is close to zero. For aperture radii much smaller than W_{LT} , the beam is strongly clipped even without wandering. Variations in the centroid position change the already-strong

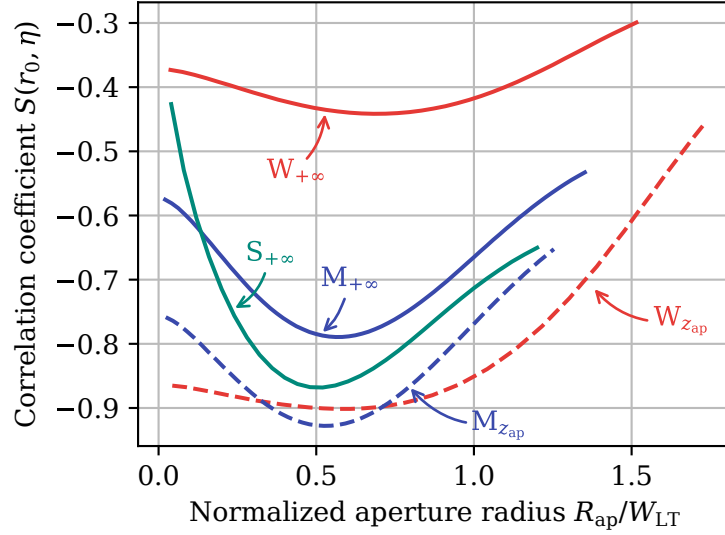


Figure 3.4 – Pearson correlation coefficient $S(r_0, \eta)$ between the beam-centroid displacement r_0 and transmittance η as a function of the normalized aperture radius $R_{\text{ap}}/W_{\text{LT}}$. The plots compare collimated ($F_0 = +\infty$) and focused ($F_0 = z_{\text{ap}}$) beams across weak (W), moderate (M), and strong (S) turbulence regimes.

clipping only slightly, consequently, the correlation remains small. The strongest correlation appears in the intermediate regime when $R_{\text{ap}} \lesssim W_{\text{LT}}$. Here, the aperture captures the central part of the beam, and centroid motion produces large changes in the overlap of the field intensity and the aperture. The minimum typically occurs around $R_{\text{ap}} \approx 0.5W_{\text{LT}}$.

A clear trend also appears when comparing channels with initial curvature $F_0 = z_{\text{ap}}$ and $F_0 = +\infty$. Channels with geometrically focused beams show larger correlations. A plausible interpretation is that focused beams exhibit smaller spreading fluctuations, meaning that transmittance fluctuations come less from beam-size changes and more from centroid displacement. With spreading variation suppressed, wandering has a comparatively stronger impact on the received power, which increases the correlation. This also explains why the total-probability model performs particularly well for the corresponding weak channel (see [Section 2.1.1](#)) and for the moderate channel in the region $R_{\text{ap}} \lesssim W_{\text{LT}}$ (see [Section 2.1.2](#)).

It is commonly accepted that in weak turbulence the beam is mainly affected by wandering, while in stronger turbulence small-scale distortions and speckles

dominate the beam structure [31]. Based on these observations, it is often assumed in the literature that models based on the beam-wandering effect should perform better in weak turbulence [60, 62], whereas in strong turbulence the lognormal model is expected to be more appropriate [63], as it represents the limiting statistics of multiplicative small-scale distortions. Moreover, fitting these analytical models to experimental data sets for a weak-turbulence channel in Erlangen [60, 91] and for a strong-turbulence channel on the Canary Islands [59] has been interpreted as supporting this picture, although this agreement appears to be accidental and results from the particular aperture size used in those experiments (see Section 2).

However, as seen in Fig. 3.4, the correlation between centroid displacement and transmittance for the weak-turbulence channel with $F_0 = +\infty$ is lower than for all other channels. In general, the maximal correlation between centroid displacement and transmittance increases with turbulence strength. This demonstrates that this previously mentioned practice of extrapolating statistical observations about the beam shape directly to the statistics of the transmittance is not justified.

3.3 Beam-wandering and beam-shape correlations

A fundamental assumption of the total-probability model is that beam wandering and beam-shape fluctuations are statistically independent. Validating this assumption is crucial for understanding the interplay between beam-centroid wandering and beam-shape distortions. It is also important for assessing the validity of analytical models that account for these effects.

We address this question using two complementary approaches. The first approach is a natural extension of the analysis presented in the previous subsection, with one key modification. As before, for each of the $5 \cdot 10^5$ simulated realizations we calculate the centroid displacement r_0 . However, instead of measuring the

transmittance η , we shift the receiver aperture to the instantaneous centroid position and evaluate the resulting transmittance, denoted η_{r_0} . This procedure emulates an ideal beam-tracking system that fully compensates for beam wandering. By analyzing the correlation between r_0 and η_{r_0} with the Pearson correlation coefficient

$$S(r_0, \eta_{r_0}) = \frac{\langle \Delta r_0 \Delta \eta_{r_0} \rangle}{\sqrt{\langle \Delta r_0^2 \rangle \langle \Delta \eta_{r_0}^2 \rangle}} \quad (3.2)$$

we isolate the statistical relationship between centroid motion and the residual beam-shape fluctuations, independent of the displacement effect. The results are summarized in Fig. 3.5. For the majority of atmospheric channels and aperture radii, the correlations are very weak, indicating that beam centroid displacements and higher-order beam-shape fluctuations are largely independent. Slightly higher correlations are observed in the strong-turbulence channel for small aperture radii, where realizations with larger centroid displacements r_0 tend to produce smaller transmittance values compared to realizations with r_0 near the optical axis.

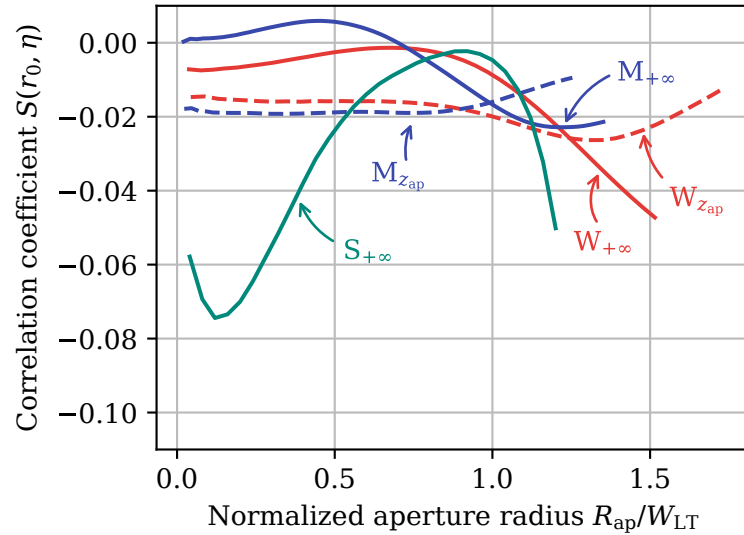


Figure 3.5 – Pearson correlation coefficient $S(r_0, \eta_{r_0})$ between the beam-centroid displacement r_0 and the tracked transmittance η_{r_0} (where the aperture is centered on the instantaneous beam centroid). The results cover weak (W), moderate (M), and strong (S) turbulence channels for both collimated ($F_0 = +\infty$) and focused ($F_0 = z_{ap}$) beams.

In the second approach, we focus on the statistical relationship between the beam centroid displacement r_0 and the instantaneous beam width. Unlike the first approach, which evaluates correlations through the measured transmittance and therefore includes aperture effects, this method directly characterizes the intrinsic properties of the beam itself, independent of any receiver geometry. However, in this approach, small-scale random intensity fluctuations, such as speckles, are effectively excluded, such that the correlation reflects only the large-scale beam spreading. To properly account for the symmetry of the system, the beam width is defined along the direction of the centroid displacement vector \mathbf{r}_0 , denoted W_r (see example in Fig. 3.6).

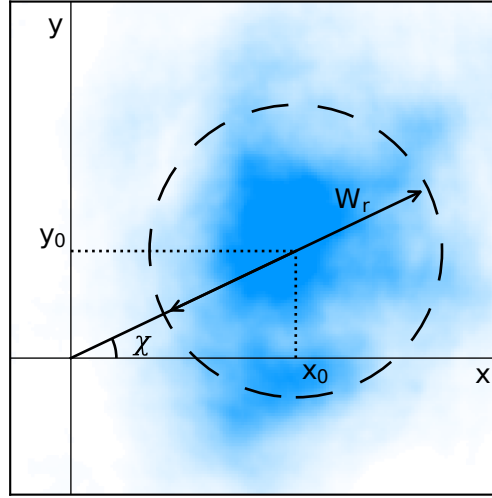


Figure 3.6 – Representative realization of an instantaneous beam intensity profile illustrating the coordinate rotation used for width measurement. The vector \mathbf{r}_0 indicates the displacement of the beam centroid from the optical axis. The coordinate system is rotated by angle χ to align the x_r axis with the wandering direction, allowing for the direct measurement of the beam width W_r along the axis of displacement.

For this analysis, we use the same $5 \cdot 10^5$ simulated realizations of the atmospheric channels. For each realization, the beam centroid displacement is represented by the vector $\mathbf{r}_0 = (x_0, y_0)^T$. The coordinate system is subsequently rotated by the angle $\chi = \arctan(y_0/x_0)$, yielding a new frame (x_r, y_r) in which the x_r axis is aligned with the direction of the beam-centroid displacement vector \mathbf{r}_0 . In this rotated frame, the beam width W_r along the x_r axis is measured for

each realization. The Pearson correlation coefficient between the magnitude of the centroid displacement r_0 and the corresponding beam width W_r along the x_r axis is estimated as

$$S(r_0, W_r) = \frac{\langle \Delta r_0 \Delta W_r \rangle}{\sqrt{\langle \Delta r_0^2 \rangle \langle \Delta W_r^2 \rangle}}. \quad (3.3)$$

The resulting correlation values for all atmospheric channels are summarized in [Table 3.4](#).

Table 3.4 – Pearson correlation coefficient $S(r_0, W_r)$ between beam centroid displacement and beam width in the rotated frame.

Channel	$F_0 = +\infty$	$F_0 = z_{\text{ap}}$
Weak	0.016	0.039
Moderate	0.08	0.15
Strong	0.32	

Overall, the correlations are small in the weak and moderate channels, indicating that beam-wandering and large-scale spreading remain largely independent in these regimes. A noticeable increase appears only for the strong-turbulence channel, indicating that, on average, beams become wider when their centroids deviate further from the propagation axis. The strength of this effect grows with increasing turbulence. These results complement the conclusions of the first approach: when turbulence is weak or moderate, centroid motion can be treated as effectively independent of beam-shape variations. Only under strong turbulence a measurable dependence arises, but even then, its impact on the transmittance remains modest.

3.4 Distribution of the beam semi-axes

In this section, we move beyond the analysis of beam wandering and beam spreading and examine the statistical behavior of the semi-axes of the elliptical Gaussian approximation of the beam shape. This effect is a central element of the elliptical-beam model (see [Section 1.3.1](#)), which explicitly includes the influence of random fluctuations of the semi-axes $W_{1,2}$. In this model, the logarithms of the squared semi-axes are assumed to follow a bivariate Gaussian distribution. However, the validity of this assumption is not established.

To test the validity of the Gaussian assumption, we generate $5 \cdot 10^5$ independent realizations of beam propagation described in [Section 2](#). For every realization, we first compute the elements of the spot-shape matrix

$$\mathbf{S} = \begin{pmatrix} S_{xx} & S_{xy} \\ S_{xy} & S_{yy} \end{pmatrix}, \quad (3.4)$$

using the definition given in [Eq. \(1.32\)](#). This matrix describes the second-order moments of the beam intensity and determines both the orientation and the magnitudes of the semi-axes. We then compute the eigenvalues of \mathbf{S} as

$$W_{\pm}^2 = \frac{1}{2} \left(S_{xx} + S_{yy} \pm \sqrt{(S_{xx} - S_{yy})^2 + 4S_{xy}^2} \right), \quad (3.5)$$

which give the squared semi-axes of the ellipse aligned with the principal axes.

Next, we assign the ordered pair W_1^2, W_2^2 according to the orientation of the ellipse in the transverse plane. If $S_{xy} > 0$, then the principal axis corresponding to W_+^2 has a positive slope, and we take $W_1^2 = W_+^2$ and $W_2^2 = W_-^2$. If $S_{xy} \leq 0$, the orientation is reversed, and we set $W_1^2 = W_-^2$ and $W_2^2 = W_+^2$. Finally, for each

realization, we compute the logarithmic variables

$$\Theta_{1,2} = \ln(W_{1,2}^2/W_0^2), \quad (3.6)$$

which are the quantities assumed to follow the bivariate Gaussian distribution in the elliptical-beam model.

The scatter plot of the obtained pairs (Θ_1, Θ_2) is shown in Fig. 3.7. To compare the empirical distribution with the bivariate Gaussian approximation, we compute the sample mean vector $\langle \Theta_i \rangle$ and the sample covariance matrix $\Sigma_{ij} = \langle \Delta \Theta_i \Delta \Theta_j \rangle$, and plot the corresponding covariance ellipse, defined by

$$\sum_{i,j=1}^2 (\Theta_i - \langle \Theta_i \rangle) \Sigma_{ij}^{-1} (\Theta_j - \langle \Theta_j \rangle) = 4, \quad (3.7)$$

which represents the two-sigma contour expected under the Gaussian assumption.

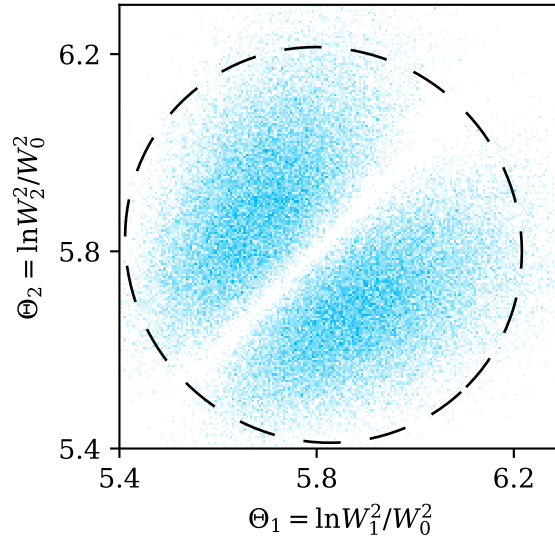


Figure 3.7 – Scatter plot of the log-transformed squared semi-axes (Θ_1, Θ_2) . The result is compared to the covariance ellipse (dashed line).

Visual inspection of the scatter plot and the corresponding covariance ellipse shows clear deviations from the bivariate Gaussian model. The dominant feature is a strong suppression of points along the diagonal $\Theta_1 = \Theta_2$. Apart from this

suppression along the diagonal, there is also a noticeable deviation between the overall shape of the data and the covariance ellipse. At the same time, the covariance ellipse is nearly circular, indicating that the linear correlation between Θ_1 and Θ_2 is weak.

To quantify these discrepancies from Gaussianity, we rotate the coordinate system in a way that the transformed data becomes symmetric around $\Theta_{(s)} = 0$. The transformed variables are defined as

$$\begin{aligned}\Theta_{(s)} &= (\Theta_1 - \Theta_2)/\sqrt{2} \\ \Theta_{(a)} &= (\Theta_1 + \Theta_2)/\sqrt{2}.\end{aligned}\tag{3.8}$$

The variable $\Theta_{(s)}$ is proportional to the logarithm of the ratio of the squared semi-axes and thus captures their relative deformation. The variable $\Theta_{(a)}$ is proportional to the logarithm of the product $W_1^2 W_2^2$, and therefore characterizes the overall beam area expansion. For each turbulence regime, we compute the skewness and the excess kurtosis of both $\Theta_{(s)}$ and $\Theta_{(a)}$. These statistics quantify the degree of non-Gaussianity, with the results summarized in [Table 3.5](#).

Table 3.5 – Higher-order moments of the transformed beam-shape variables $\Theta_{(s)}$ and $\Theta_{(a)}$ for different turbulence channels.

Channel	F_0	Skewness		Excess kurtosis	
		$\Theta_{(s)}$	$\Theta_{(a)}$	$\Theta_{(s)}$	$\Theta_{(a)}$
Weak	z_{ap}	-0.6×10^{-3}	0.25	-0.85	0.23
	∞	-10×10^{-3}	-0.1	-1	-0.006
Moderate	z_{ap}	9.8×10^{-3}	0.25	-0.81	0.12
	∞	-3.7×10^{-3}	0.15	-0.99	-0.11
Strong	∞	-9×10^{-3}	0.32	-0.77	0.25

The distribution of $\Theta_{(s)}$ is highly symmetric, yet it is clearly platykurtic. This behavior directly reflects the strong suppression of probability density at $\Theta_{(s)} = 0$ (equivalently, $\Theta_1 = \Theta_2$), which is the dominant non-Gaussian feature of the data.

In contrast, the distribution of $\Theta_{(a)}$ is notably asymmetric, but its excess kurtosis is closer to zero. Taken together, these observations show that the joint distribution of Θ_1 and Θ_2 cannot be adequately described by a bivariate Gaussian model, indicating that a deeper analysis of the statistical properties of \mathbf{S} is necessary. Understanding the behavior of the \mathbf{S} eigenvalues can be further advanced through methods and insights from random matrix theory.

4 Moment matching for the Circular-beam model

4.1 Introduction

In [Section 2](#), we demonstrated that models based on statistics of beam parameters, such as the beam-wandering model and the elliptical-beam model, exhibit misspecification bias. This bias affects the first two moments of the transmittance distribution, $\langle \eta \rangle$ and $\langle \eta^2 \rangle$. As a consequence, these models show poor agreement with numerical simulations. Since many quantum protocols in turbulent atmospheres, including those that will be analysed in [Section 6](#), rely directly on the transmittance moments, this bias leads to degraded protocol performance.

In this section, we address this problem by introducing a moment matching procedure for such models, which was introduced in our work [\[III\]](#). The goal is to enforce agreement with the transmittance moments while maintaining a physically interpretable model description. Physically based models are specified in terms of low-order statistics of the beam shape, which are summarised in [Table 4.1](#). These include the mean and variance of the beam centroid position and the mean and variance of an effective beam size parameter S .

Table 4.1 – Summary of beam shape statistics used for physically based model parameterisation.

	on average	variability
beam position	$\langle x_0 \rangle = 0$	$\langle x_0^2 \rangle$
beam size	$\langle S \rangle$	$\langle S^2 \rangle$

The beam-wandering model $\mathcal{P}_{\text{BW}}(\eta \mid \langle x_0^2 \rangle, \langle S \rangle)$ is a two-parameter model. It assumes a circular beam with fixed size $\langle S \rangle$ and neglects higher-order beam size fluctuations. The elliptical-beam model extends this description to four parameters. In addition to the beam position variability $\langle x_0^2 \rangle$, it accounts for fluctuations of the beam semiaxes $W_{1,2}$ (see [Section 3.4](#)) and their correlations. While the beam-wandering model admits a fully analytical expression for the PDT,

the elliptical-beam model requires Monte Carlo sampling to evaluate the PDT.

The complexity of the elliptical-beam model makes a direct reparametrisation in terms of transmittance moments impractical. In addition, the number of model parameters would require more than two transmittance moments for a physically meaningful reparametrisation. For this reason, we consider an intermediate case with three effective parameters, referred to as the Circular-beam model, introduced in Ref. [III]. This model bridges the beam-wandering and elliptical-beam descriptions. It remains analytically tractable while incorporating beam size variability. We further introduce a moment matching procedure that enforces agreement with selected transmittance moments.

Even though the proposed approach does not explicitly model beam ellipticity, which enters at higher order in the beam shape description, it enforces consistency with low-order transmittance moments. As a result of transmittance matching, the effective beam size moments $\langle S \rangle$ and $\langle S^2 \rangle$ become biased. They absorb contributions from higher-order beam deformations and scintillation effects that are not explicitly included. This approach remains simple and analytically tractable, and it is shown to improve protocol performance.

4.2 The model

The PDT of the Circular-beam model is defined as a compound distribution that extends the beam-wandering model by treating the beam size S as a random variable

$$\mathcal{P}(\eta \mid \langle x_0^2 \rangle, \langle \eta \rangle, \langle \eta^2 \rangle) = \int_0^\infty dS \mathcal{P}_{\text{BW}}(\eta \mid \langle x_0^2 \rangle, S) P(S \mid \mu, \sigma), \quad (4.1)$$

where $\mathcal{P}_{\text{BW}}(\eta \mid \langle x_0^2 \rangle, S)$ is the beam-wandering PDT [62], which describes transmittance fluctuations caused solely by the random displacement of a Gaussian beam with fixed width S , where the displacement variance is characterized by $\langle x_0^2 \rangle$. The fluctuations of the beam size S are incorporated through the distribution $P(S \mid \mu, \sigma)$. Its parameters $\mu = \mu(\langle \eta \rangle, \langle \eta^2 \rangle)$ and $\sigma = \sigma(\langle \eta \rangle, \langle \eta^2 \rangle)$ are fixed by enforcing the prescribed moments $\langle \eta \rangle$ and $\langle \eta^2 \rangle$. As a result, the transmittance statistics simultaneously account for beam displacement and beam deformation, and are specified by the second moment of beam displacement $\langle x_0^2 \rangle$ and the first two moments of the transmittance.

Since the beam size is strictly positive, its distribution must have positive support. Numerical simulations further show that its empirical distribution is well approximated by a lognormal distribution for all considered channels in [Section 2](#). This observation aligns with the treatment of turbulence-induced distortions as multiplicative, which often leads to lognormal statistics. Therefore, the beam size distribution is chosen as

$$P(S \mid \mu, \sigma) = \frac{1}{S\sigma\sqrt{2\pi}} \exp \left[-\frac{(\ln S - \mu)^2}{2\sigma^2} \right]. \quad (4.2)$$

[Figure 4.1](#) illustrates this agreement for a channel of moderate turbulence with $F_0 = z_{\text{ap}}$, which represents the worst-case scenario among all channels. The strong-turbulence channel exhibits slightly better but similar agreement, while weak-turbulence channels show much better correspondence. This agreement supports the use of the lognormal approximation for the beam size distribution across different turbulence regimes.

In principle, the parameters μ and σ could be inferred from the moments $\langle S \rangle$ and $\langle S^2 \rangle$. However, this choice leads to biased transmittance moments, as discussed above. Instead, the present approach applies transmittance moment matching to the Circular-beam model. The parameters μ and σ are therefore defined implicitly by

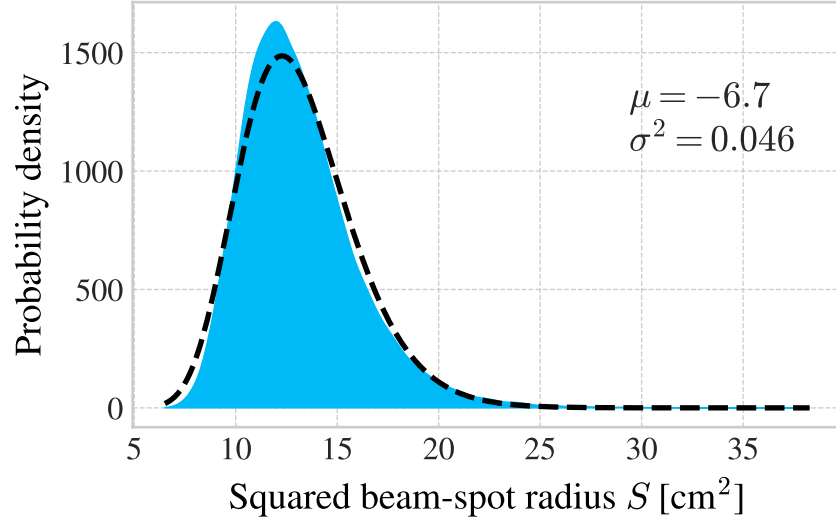


Figure 4.1 – Verification of the lognormal approximation for the effective beam size S . The plot compares the empirical probability density function obtained from $5 \cdot 10^5$ numerical beam-propagation simulations (blue histogram) against a fitted lognormal distribution (dashed line). The data corresponds to a moderate turbulence channel with a focused beam ($F_0 = z_{\text{ap}}$), representing the regime with the worst-case scenario.

computing the first two transmittance moments of the model (see [Eq. \(4.1\)](#)), which yields

$$\begin{cases} \langle \eta \rangle &= \int_0^\infty dS P(S | \mu, \sigma) \langle \eta \rangle_{\text{BW}} \\ \langle \eta^2 \rangle &= \int_0^\infty dS P(S | \mu, \sigma) \langle \eta^2 \rangle_{\text{BW}}. \end{cases} \quad (4.3)$$

Here $\langle \eta \rangle_{\text{BW}}$ and $\langle \eta^2 \rangle_{\text{BW}}$ denote the moments of the beam-wandering model evaluated at fixed S .

As derived in Ref. [\[95\]](#), these moments for the beam-wandering model take the form

$$\begin{aligned}
\langle \eta \rangle_{\text{BW}} &= 1 - \exp \left(-2 \frac{a^2}{4 \langle x_0^2 \rangle + S} \right), \\
\langle \eta^2 \rangle_{\text{BW}} &= 1 - 2 \exp \left(-2 \frac{a^2}{4 \langle x_0^2 \rangle + S} \right) \\
&\quad + \exp \left(-\frac{\alpha^2}{2} \right) \left[1 - Q \left(\frac{\alpha}{\sqrt{1 - \beta^2}}, \frac{\alpha \beta}{\sqrt{1 - \beta^2}} \right) \right. \\
&\quad \left. + Q \left(\frac{\alpha \beta}{\sqrt{1 - \beta^2}}, \frac{\alpha}{\sqrt{1 - \beta^2}} \right) \right],
\end{aligned} \tag{4.4}$$

where the function Q denotes the Marcum Q function of order one [96], and the auxiliary parameters are defined as

$$\begin{aligned}
\alpha &= \frac{2a}{\sqrt{S}} \left[\frac{2p(p+1)}{2p^2 + 3p + 1} \right]^{1/2}, \\
\beta &= (2p+1)^{-1}, \quad p = \frac{1}{8} \frac{S}{\langle x_0^2 \rangle}.
\end{aligned} \tag{4.5}$$

Because no closed-form solution exists for this system of equations, the parameters μ and σ are obtained numerically. When estimates of $\langle S \rangle$ and $\langle S^2 \rangle$ are available, they provide a convenient initial guess

$$\mu_0 = \ln \left(\frac{\langle S \rangle^2}{\sqrt{\langle S^2 \rangle}} \right), \quad \sigma_0^2 = \ln \left(\frac{\langle S^2 \rangle}{\langle S \rangle^2} \right). \tag{4.6}$$

After determining the parameters μ and σ , the PDT is evaluated by numerical integration over the beam size variable S .

Finally, the infinite support of the lognormal distribution requires truncation for numerical implementation. The upper limit is chosen as S_{max} such that the tail probability satisfies $P(S > S_{\text{max}}) < \delta$. This cutoff is obtained from the percentage point function (PPF) of the lognormal distribution as $S_{\text{max}} = \text{PPF}(1 - \delta)$. This

truncation bounds the neglected probability mass and has a negligible impact on the evaluated transmittance moments.

4.3 Validation

We apply the same validation procedure as in [Section 2](#). We compare the proposed model against existing physically based models and other well-performing models. The comparison is based on the Kolmogorov-Smirnov statistic between numerically obtained PDTs and the analytical models. The results are summarized in [Fig. 4.2](#).

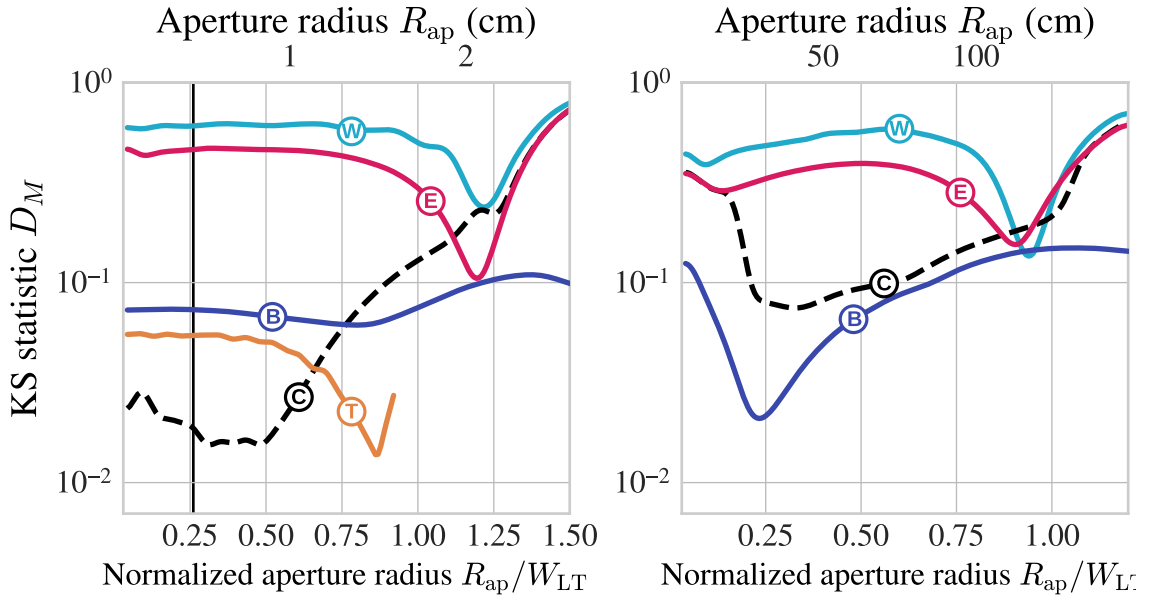


Figure 4.2 – Kolmogorov-Smirnov (KS) statistic comparing the proposed Circular-beam model with moment matching (C) against the beam wandering (W), elliptical beam (E), total probability (T) and Beta distribution (B) models. The left panel shows the weak turbulence channel with focused beams ($F_0 = z_{ap}$), where the proposed model achieves the lowest overall error in the region of small apertures. The right panel displays the strong turbulence regime, where the proposed model significantly outperforms other physical models despite the Beta distribution providing a closer fit.

The left panel of [Fig. 4.2](#) corresponds to the channel with weak turbulence and

$F_0 = z_{\text{ap}}$. This case yields the best overall performance for the proposed model. The improvement over traditional physically based models is pronounced, particularly for small aperture radii compared to the beam size W_{LT} . Moreover, in this region, the proposed model yields the smallest KS statistic among all considered analytical models. An explicit example of the PDT for $R_{\text{ap}} = 0.45$ cm is shown in Fig. 4.3.

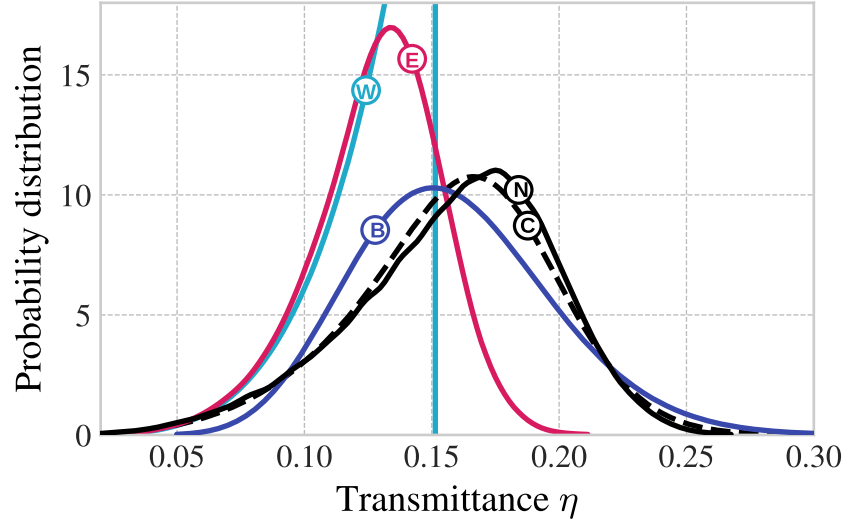


Figure 4.3 – Comparison of the PDT for a weak turbulence channel ($F_0 = z_{\text{ap}}$) at an aperture radius $R_{\text{ap}} = 0.45$ cm. While the Beta distribution (B) is constrained by the same first two moments as the proposed model, it fails to capture the precise shape of the distribution. In contrast, the Circular-beam model with the moment-matching technique (C) provides the best agreement with the numerical simulations (N). Traditional physically based models, such as beam wandering (W) and the elliptical-beam model (E), show completely mismatched PDTs due to misspecification bias.

We see that the Beta distribution model deviates in shape from the numerically simulated distribution, despite being defined through the same first two moments of transmittance. The Circular-beam model with moment matching shows almost perfect agreement in this specific case. This is because the skewness, given by the third moment of the transmittance, and the kurtosis are reproduced more accurately.

For apertures larger than the beam size, the agreement of the proposed model is reduced. A distinct discrepancy appears near the local minimum of the elliptical-beam model when $R_{\text{ap}}/W_{\text{LT}} \approx 1.2$. At this point, the elliptical-beam model

outperforms the proposed model because the statistical mode of its PDT coincides with the mode of the numerically obtained distribution. Mode matching, instead of moment matching, could in principle improve the agreement of the proposed model. However, such an approach is not practical because the transmittance mode cannot be reliably estimated in experiments and no closed-form analytical expression for the transmittance mode is available.

The right panel of [Fig. 4.2](#) shows the results for the strong turbulence channel, which exhibits the largest overall deviations. In this case, the Beta distribution model provides better agreement over the full aperture range. However, the Circular-beam model with moment matching still outperforms the other physically motivated models. Channels with weak turbulence and $F_0 = \infty$ and with moderate turbulence and $F_0 = \infty$ show similar behavior with slightly better performance. The channel with moderate turbulence and $F_0 = z_{\text{ap}}$ yields intermediate results.

4.4 Summary

We introduced a physically motivated PDT model complemented by transmittance moment matching. While the Circular-beam model provides an intermediate approximation of the beam shape between the beam-wandering and elliptical-beam approaches, our moment matching procedure ensures that its first two transmittance moments are imposed by design. This removes the model misspecification bias observed in traditional physically based models and directly targets the quantities most relevant for quantum protocol performance.

The model relies on two structural assumptions. First, we assume that fluctuations of the beam centroid x_0 and of the beam spot size S occur on distinct spatial scales of turbulence, allowing them to be treated as statistically independent. As shown in [Section 3](#), small correlations between x_0 and S exist but

remain negligible for weak and moderate turbulence. Second, beam ellipticity and higher-order deformations are not modeled explicitly. Their contributions are absorbed into effective beam size fluctuations through moment matching. Consequently, the inferred moments of S lose a direct physical interpretation but achieve consistency at the level of transmittance statistics.

Validation against numerical simulations demonstrates a substantial improvement over existing physically motivated models across most channels. In the weak turbulence regime with $F_0 = z_{\text{ap}}$ and small apertures, the model outperforms all existing analytical approaches. More generally, performance is better for $F_0 = z_{\text{ap}}$ compared to $F_0 = z_{\infty}$ and for aperture radii smaller than the average beam size.

Validation was performed using the first two transmittance moments, $\langle \eta \rangle$ and $\langle \eta^2 \rangle$, obtained directly from simulations. If analytical approximations of these moments are used, or if experimental noise and systematic errors affect their estimation, the performance of the model may degrade. This limitation motivates further work on improved analytical expressions for low-order transmittance moments.

Overall, the proposed application of moment matching to the Circular-beam model provides a robust, physically grounded description of the PDT. It requires only simple numerical integration and parameter optimization, resulting in substantially lower computational costs than full phase-screen simulations. Furthermore, it defines the PDT in terms of measurable quantities at the aperture plane— such as beam wandering $\langle x_0 \rangle$ and the first two transmittance moments $\langle \eta \rangle$ and $\langle \eta^2 \rangle$ —whereas the phase-screen method requires a detailed turbulence profile description. These features make it suitable for practical applications in quantum communication.

5 Time correlations in Atmospheric Quantum Channels

In the previous sections we treated the PDT as describing an ensemble of independent single-shot propagations of quantum states of light through a turbulent atmosphere. This can also be viewed as a sequence of quantum states transmitted with sufficiently large time intervals, such that each transmission is effectively independent and no temporal correlations exist between them. In practice, this idealization is overly simplistic. Modern quantum optical systems often operate at MHz repetition rates. At these repetition rates, consecutive pulses experience highly correlated atmospheric realizations. As a result, the transmittance η_t of consecutive pulses is correlated at different times t .

In this section we analyze the case of two consecutive pulses separated by a time interval τ . With the numerical model, we compute the joint statistics of two consecutive transmittances. In particular, we study how the temporal correlation of the transmittance depends on the time separation τ . We also describe the PDT in scenarios relevant for adaptive selection techniques [97], where the first signal is a strong classical pulse used to estimate the channel transmittance, and the second is a quantum signal whose transmittance is conditioned on the measured transmittance of the first. In [Section 6](#), we will demonstrate how these results guide continuous-variable and discrete-variable entanglement propagation protocols, and how they can be employed to enhance the preservation of nonclassicality through adaptive selection techniques. This chapter is based on results presented in our works [\[III\]](#) and [\[IV\]](#).

5.1 Two-time PDT

To describe the two-time PDT, we extend the PDT framework (see [Section 1.3](#)) to account for time-dependent fluctuations of the refractive index. In this approach,

the refractive index is represented as

$$n_t(\mathbf{r}, z) = 1 + \delta n_t(\mathbf{r}, z), \quad (5.1)$$

where $\delta n_t(\mathbf{r}, z)$ denotes the small, time-dependent, stochastic perturbation caused by atmospheric turbulence. The evolution of the complex field amplitude $u_t(\mathbf{r}, z)$ under these conditions is governed by the paraxial wave equation (see Eq. (1.22)), which, for a time-dependent refractive index, takes the form

$$2ik \frac{\partial u_t(\mathbf{r}, z)}{\partial z} + \Delta_{\mathbf{r}} u_t(\mathbf{r}, z) + 2k^2 \delta n_t(\mathbf{r}, z) u_t(\mathbf{r}, z) = 0. \quad (5.2)$$

To specify the temporal evolution of the refractive index we adopt the Taylor frozen-turbulence hypothesis (see Eq. (1.20)) described in Section 1.4.2. Under this assumption, time-dependent turbulence can be represented as a frozen spatial pattern advected by the wind.

The transmittance through a receiving aperture \mathcal{A} at time t is then given by the aperture-averaged intensity of the propagated field

$$\eta_t = \int_{\mathcal{A}} d^2\mathbf{r} |u_t(\mathbf{r}, z_{\text{ap}})|^2. \quad (5.3)$$

We consider two temporal modes at $t = 0$ and $t = \tau$. The two-mode input–output relation for the Glauber P function for channels with fixed linear losses η_0 and η_τ reads by analogy with the single-time relation (see Eq. (1.2))

$$P_{\text{out}}(\alpha_0, \alpha_\tau | \eta_0, \eta_\tau) = \frac{1}{\eta_0 \eta_\tau} P_{\text{in}} \left(\frac{\alpha_0}{\sqrt{\eta_0}}, \frac{\alpha_\tau}{\sqrt{\eta_\tau}} \right). \quad (5.4)$$

Averaging over the atmospheric realizations leads to the input-output relation for the

two-time channel

$$P_{\text{out}}(\alpha_0, \alpha_\tau) = \int_{\Xi} d\eta_0 d\eta_\tau \left[\frac{1}{\eta_0 \eta_\tau} P_{\text{in}} \left(\frac{\alpha_0}{\sqrt{\eta_0}}, \frac{\alpha_\tau}{\sqrt{\eta_\tau}} \right) \right] \mathcal{P}(\eta_0, \eta_\tau), \quad (5.5)$$

where $\Xi = [0, 1] \times [0, 1]$, and where the joint distribution $\mathcal{P}(\eta_0, \eta_\tau)$ is the two-time PDT.

The two-time PDT provides a complete description of such atmospheric quantum channels. The single-time PDT is obtained as its marginal

$$\mathcal{P}(\eta_0) = \int d\eta_\tau \mathcal{P}(\eta_0, \eta_\tau). \quad (5.6)$$

Adaptive selection protocols rely on conditional statistics. If the protocol keeps only those events for which the first classical probe pulse has transmittance $\eta_0 \geq \eta_{\min}$, then the conditional PDT describing the second quantum pulse at time $t = \tau$ is

$$\mathcal{P}(\eta_\tau | \eta_0 \geq \eta_{\min}) = \frac{1}{\overline{\mathcal{F}}(\eta_{\min})} \int_{\eta_{\min}}^1 d\eta_0 \mathcal{P}(\eta_\tau, \eta_0), \quad (5.7)$$

where

$$\overline{\mathcal{F}}(\eta_{\min}) = \int_{\eta_{\min}}^1 d\eta_0 \mathcal{P}(\eta_0) \quad (5.8)$$

is the exceedance. This conditional PDT directly determines the statistics of accepted pulses and therefore the performance of adaptive schemes. It also makes it possible to compute the moments that are required for the analysis of entanglement decay in continuous-variable and discrete-variable protocols. This formulation makes it possible to track how these quantities depend on the pulse separation time, which is crucial for quantifying the influence of temporal correlations in quantum communication protocols.

Numerical approach. For the numerical simulations we use the phase-screen method introduced in [Section 1.4](#). We extend this model to the time-dependent case by incorporating the Taylor frozen-flow hypothesis. First, we note that the wind-driven advection has a component in the longitudinal direction and a component in the transverse plane. The longitudinal component produces pattern shifts that are much smaller than the channel length for the timescales that are relevant for our analysis. Therefore, this component does not influence the temporal behavior in a measurable way and can be neglected in the simulations.

We also assume that the advected wind velocity v is constant at all points along the channel length. While in reality the wind exhibits spatial inhomogeneity across the propagation path, this simplification is necessary to maintain model identifiability and tractability. In principle, such inhomogeneity could be accounted for by assigning different velocities to each phase screen. However, this approach would lead to an over-parameterized system with limited explanatory power. By contrast, using a single velocity parameter v for all phase screens ensures that the model remains tractable and allows us to isolate the specific effect of the wind-driven advection on the channel transmittance.

The coordinate system is rotated such that the new x -axis is aligned with the transverse wind direction. Under this choice of coordinates, consider two optical pulses propagating through the channel, one at time $t = 0$ and another at $t = \tau$. The turbulence along the propagation path is represented by multiple phase screens, and for each screen, the realizations at these two times are related by

$$\varphi_\tau(x, y, z) = \varphi_0(x + v\tau, y, z), \quad (5.9)$$

where $s = v\tau$ represents the wind-driven shift of the turbulent pattern over the time interval τ .

For the given wind velocity, the displacement s and the time interval τ are

interchangeable. Accordingly, we will present the results mostly in terms of s . For interpretation, we assume a typical wind speed of $v = 10\text{m/s}$ unless stated otherwise, which implies that a spatial shift of 1 cm corresponds to 1 ms of the time interval τ . For any other desired wind speed v , the corresponding time interval can be obtained directly from the relation $\tau = s/v$.

We consider three atmospheric channels characterized by refractive index structure constants $C_n^2 = 1 \times 10^{-16} \text{ m}^{-2/3}$, $C_n^2 = 2 \times 10^{-16} \text{ m}^{-2/3}$, and $C_n^2 = 3 \times 10^{-16} \text{ m}^{-2/3}$. For all channels the propagation distance is fixed at $z_{\text{ap}} = 50 \text{ km}$. These values correspond to Rytov parameters $\sigma_R^2 = 5.5$, $\sigma_R^2 = 11$, and $\sigma_R^2 = 16.5$. The inner and outer turbulence scales are set to $\ell_0 = 1 \text{ mm}$ and $L_0 = 80 \text{ m}$. The source is a Gaussian beam of wavelength $\lambda = 808 \text{ nm}$ with initial beam width $W_0 = 8 \text{ cm}$ and curvature radius $F_0 = 50 \text{ km}$.

The numerical grid contains 2048 points in both transverse directions with a grid step of 1 mm. The sparse-spectrum phase-screen method (see [Section 1.4](#)) is used with 1024 spectral rings. The spectral bounds are defined as $K_{\min} = 1/15L_0$ and $K_{\max} = 2/\ell_0$. The propagation path is discretized into 15 phase screens (see [Section 1.4.5](#)). For each of the three channels, we generate 5×10^4 independent realizations for different values of the time interval τ and aperture radius R_{ap} .

5.2 Results

5.2.1 Two-time PDT

The joint distribution of the transmittance at two different times offers a direct view of the statistical dependence between consecutive pulses separated by the time interval $\tau = s/v$. In [Fig. 5.1](#), the two-dimensional kernel density estimates of the joint PDT are shown for short and long pulse separation times for $R_{\text{ap}} = 20 \text{ cm}$. For the smaller time interval $s = 3 \text{ cm}$ ($\tau = 3 \text{ ms}$), the distribution is sharply

concentrated along the diagonal. Because the refractive index pattern changes only slightly over such a short interval, the transmittance undergoes only minor variations. As a result, the two pulses show a high level of temporal correlation, implying a strong potential for entanglement preservation and effective use of adaptive protocols.

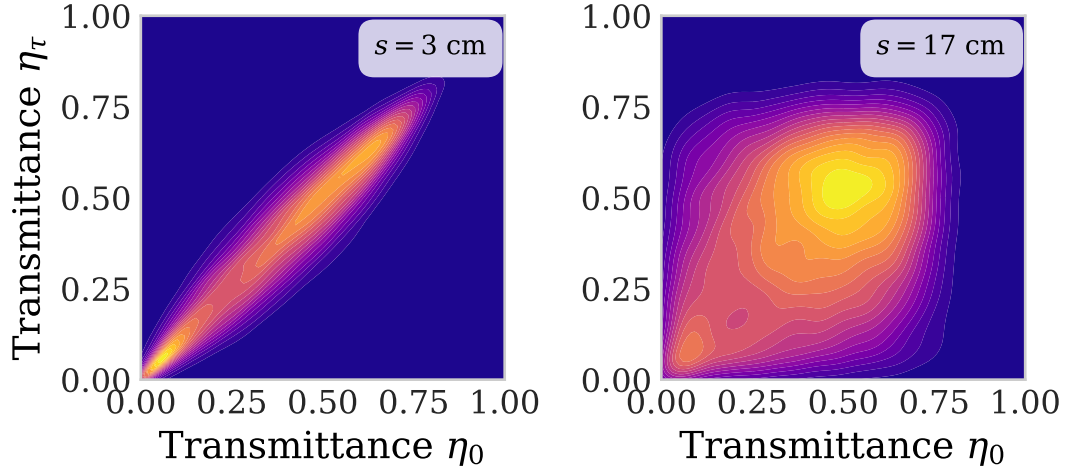


Figure 5.1 – Two-time PDT $\mathcal{P}(\eta_0, \eta_\tau)$ for the channel with $\sigma_R^2 = 5.5$ and $R_{\text{ap}} = 20$ cm. The left panel shows a short pulse separation, where the distribution is concentrated along the diagonal, indicating high temporal correlation. The right panel shows a longer separation, where the distribution spreads and approaches a product of marginals $\mathcal{P}(\eta_0)\mathcal{P}(\eta_\tau)$, signifying nearly independent transmittance events. Color intensity indicates density, transitioning from blue for zero values to yellow for peak values.

For the larger time interval $s = 17$ cm ($\tau = 17$ ms), the distribution spreads significantly. This behavior indicates that the turbulent pattern has moved a much greater transverse distance, hence, the two pulses experience nearly independent transmittance values. The joint PDT approaches the product of the two single-time distributions $\mathcal{P}(\eta)$, indicating that the channel can be effectively described using only the single-time PDT. In this regime, adaptive selection becomes less effective because the value of η_0 carries little information about η_τ . The comparison of these two situations demonstrates that the two-time PDT is the central object for such

channels. It directly reveals how the atmosphere preserves correlations between consecutive pulses.

5.2.2 Spatial coherence radius

Figure 5.2 presents the Pearson correlation between the aperture-averaged transmittances η_0 and η_τ as a function of the pulse separation time τ for two receiving apertures. The correlation exhibits a strictly monotonic decrease as s increases. This reflects the decorrelation caused by the transverse motion of refractive-index inhomogeneities.

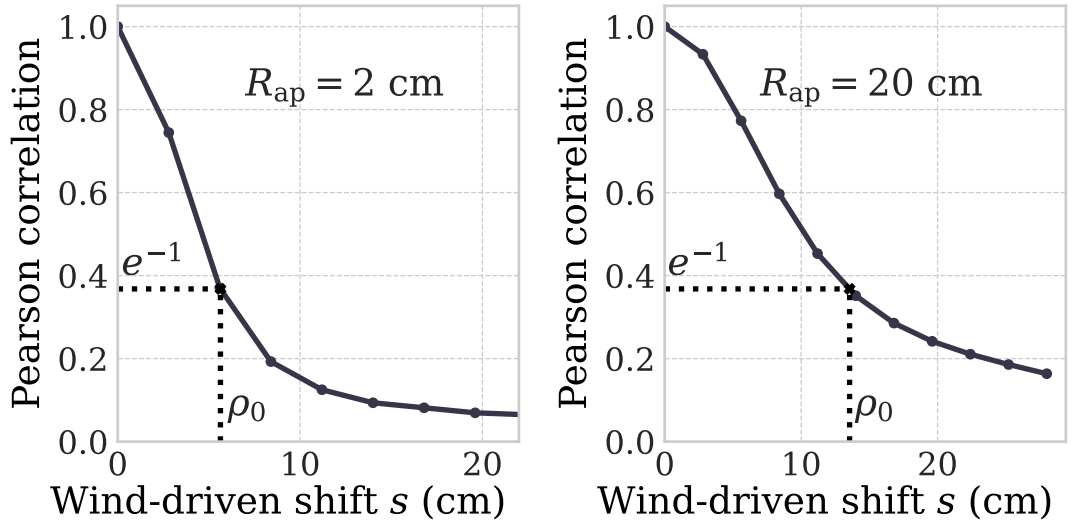


Figure 5.2 – Pearson correlation coefficient between transmittances η_0 and η_τ as a function of the wind-driven shift s for two different aperture radii R_{ap} . The horizontal dotted line indicates the e^{-1} threshold used to define the spatial coherence radius ρ_0 . Results are shown for the turbulence channel with $\sigma_R^2 = 5.5$.

To quantify this behaviour by a single physically interpretable measure, we introduce the aperture-averaged spatial coherence radius ρ_0 , defined as the value of the wind-driven shift s for which the Pearson correlation falls to e^{-1} [31]. This coherence radius captures the time interval τ (transverse wind-driven shift s) over which statistical correlations persist. In practical free-space quantum communication, this parameter quantifies the minimal pulse rate v/ρ_0 above which successive

quantum states experience non-negligible correlations.

For a channel with $C_n^2 = 1 \times 10^{-16} \text{ m}^{-2/3}$ and small receiving aperture $R_{\text{ap}} = 2 \text{ cm}$, the observed spatial coherence radius is $\rho_0 = 6 \text{ cm}$, which corresponds to $\tau = 6 \text{ ms}$. For the same channel but large aperture $R_{\text{ap}} = 20 \text{ cm}$, the coherence radius increases to $\rho_0 = 13 \text{ cm}$. This can be explained by noting that a larger aperture captures a broader region of the wavefront, which means that the turbulence-induced intensity pattern must be shifted much farther by the wind before the transmittance changes noticeably.

A more systematic view is provided in Fig. 5.3, which shows ρ_0 as a function of aperture radius across all simulated turbulence regimes. The figure indicates that the spatial coherence radius ρ_0 grows monotonically as the aperture radius R_{ap} becomes larger. This implies that a wider aperture allows the optical field to maintain its nonclassical features for a longer time. For a fixed aperture radius, the dependence on the Rytov variance σ_R^2 is weak within the analyzed interval from five to sixteen. This observation suggests that the aperture plays the primary role in setting the coherence properties of such channels.

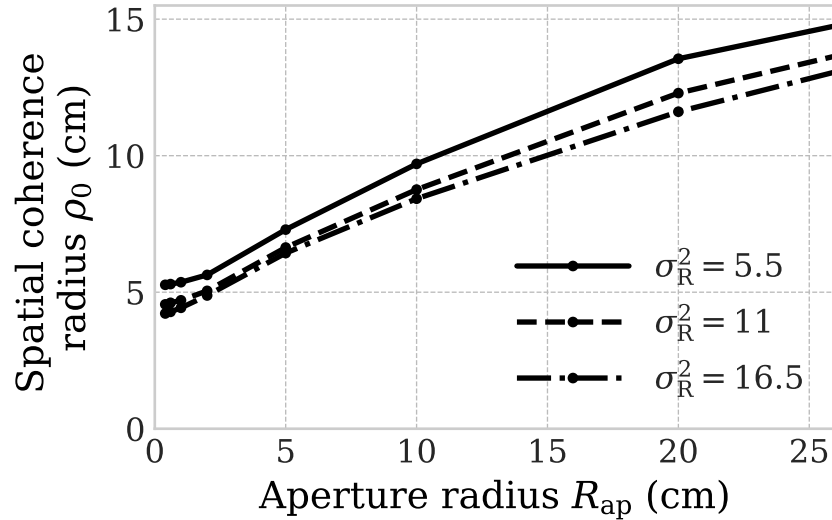


Figure 5.3 – Aperture-averaged spatial coherence radius ρ_0 as a function of the aperture radius R_{ap} for three turbulence regimes.

Summarizing this consideration, we note that the spatial coherence radius ρ_0 determines the temporal interval over which successive pulses remain statistically

correlated, directly influencing the decay of quantum correlations in turbulent atmospheric channels. The impact of turbulence strength on ρ_0 remains limited across the examined range, while the change produced by the receiver aperture size is noticeably larger. As a result, $\rho_0(R_{\text{ap}})$ provides guidance for selecting pulse repetition rates for which temporal correlations can be exploited (or can be safely neglected) in realistic atmospheric quantum channels.

5.2.3 Conditional PDT

Adaptive selection works by first sending a strong classical pulse through the channel at $t = 0$. If the measured transmittance of this pulse exceeds a threshold η_{min} , the subsequent quantum pulse is transmitted at $t = \tau$. If the transmittance is less than the threshold, the quantum pulse is discarded. By selectively transmitting only those quantum pulses that are likely to encounter high transmittance channel conditions, the protocol can enhance the preservation of nonclassical properties and increase the performance of quantum communication protocols. The conditional PDT provides the exact probability distribution of the transmittance of the second pulse under this selection procedure.

Figure 5.4 shows the conditional PDT of the second pulse for different spatial shifts s , corresponding to various time intervals τ between pulses, for $\eta_{\text{min}} = 0.45$. For small shifts, up to $s \sim 1$ cm ($\tau \sim 1$ ms), the conditional distribution closely resembles the ideal case with $s = 0$, indicating that the transmittance of the first pulse reliably predicts the second pulse. As s increases to several centimeters (several milliseconds), the probability of transmittance values below the threshold η_{min} becomes more significant. For tens of centimeters of wind-driven shifts s (tens of milliseconds of τ), the conditional PDT approaches the single-time PDT.

These results demonstrate that adaptive selection is most effective for short time intervals, on the order of a few centimeters of wind-driven shift or several milliseconds of time separation between pulses for $v = 10$ m/s. For longer

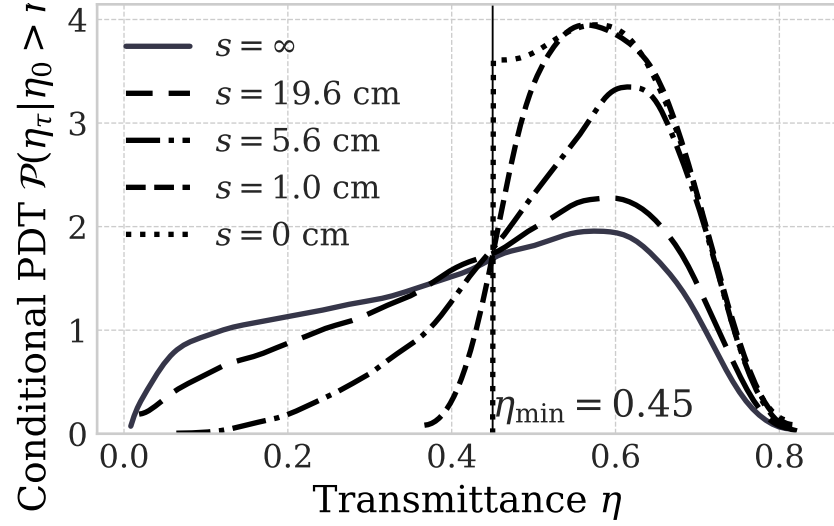


Figure 5.4 – Conditional PDT $\mathcal{P}(\eta_\tau | \eta_0 > \eta_{\min})$ for varying wind-driven shifts s . At small shifts (e.g., $s = 1$ cm), the distribution is located at high transmittance values, validating the predictive power of the probe pulse. As the shift increases, the distribution broadens and eventually converges to the unconditioned single-time PDT (grey solid line), marking the limit of adaptive selection effectiveness.

intervals, the predictive power of the classical probe decreases, and the channel can be accurately described using only the single-time PDT. This analysis provides a quantitative framework for designing adaptive protocols and predicting their performance in realistic quantum communication systems. The application of these results for preserving nonclassical properties will be demonstrated in [Section 6](#).

5.3 Summary

The analysis of time correlations in atmospheric quantum channels demonstrates that the transmittance of consecutive optical pulses cannot generally be treated as independent. The concept of the two-time PDT $\mathcal{P}(\eta_0, \eta_\tau)$ provides a complete and tractable framework to quantify these correlations. As temporal correlations decay monotonically with pulse separation, the spatial coherence radius ρ_0 emerges as the central parameter for characterizing the persistence of temporal

correlations between consecutive pulses. Its value depends primarily on the receiver aperture and only weakly on turbulence strength within the considered range. This implies that by selecting the aperture size appropriately, one can control the timescale over which successive quantum states remain statistically correlated, which is directly relevant for entanglement preservation in turbulent atmospheric channels. For the channels studied, these correlations persist over several milliseconds, corresponding to wind-driven shifts of a few centimeters.

The conditional PDT captures a complementary property relevant for adaptive selection protocols. By selecting quantum pulses based on the measured transmittance of a preceding classical probe, one can enhance the likelihood of transmitting through high-transmittance channel realizations. The conditional PDT provides a precise description of the second pulse PDT under such selection protocols, directly influencing the preservation of nonclassical properties and the performance of other quantum communication protocols.

Overall, the results show that the two-time PDT and derived quantities such as ρ_0 and the conditional PDT are complementary tools. The spatial coherence radius quantifies the timescale over which successive pulses remain statistically correlated and is essential for entanglement-based protocols, while the conditional PDT captures the potential for adaptive selection protocols, for example to enhance the preservation of nonclassicality. These findings provide a practical framework for designing and evaluating quantum communication systems. In [Section 6](#), these results will be applied to study the preservation of continuous-variable and discrete-variable entanglement as a function of pulse separation, as well as the enhancement of nonclassicality through adaptive selection.

6 Applications

This chapter investigates applications of the theory developed in previous sections to a description of quantum-light propagation through turbulent atmospheric channels. These results were presented in our work [III]. Understanding the limits of preservation of nonclassical properties under realistic conditions is essential for designing robust quantum communication protocols. We quantify the effects of channel properties, including temporal correlations, aperture size, and finite detector resolution, on different aspects of quantumness. This analysis provides a practical framework for assessing the feasibility of free-space quantum tasks.

We analyze three distinct manifestations of quantumness under these conditions. First, we investigate the preservation of Gaussian entanglement [98, 99] between continuous-variable pulses separated by a finite time delay. Second, we extend this analysis to discrete-variable systems [100], focusing on polarization-entangled states. In both entanglement scenarios, the first mode is sent through the atmospheric channel at time $t = 0$, while the second mode is stored in a quantum memory and released at a later time $t = \tau$. Finally, we consider adaptive selection strategies [97, 101] for single-mode nonclassicality, examining the impact of the temporal separation between a classical probe and the quantum state on squeezed vacuum and squeezed coherent states.

A central theme of this discussion is the role of temporal correlations in the channel. We build on time-dependent transmittance simulations described in the previous chapter (see Section 5). Our analysis accounts for realistic conditions, including parametric down-conversion states rather than single-photon Bell states, the interplay between turbulence and quantum memory delay, detector efficiency, and the finite dimensionality of photon-number-resolving detectors. The results provide a quantitative framework for assessing the feasibility of free-space quantum tasks under realistic atmospheric conditions.

6.1 Gaussian entanglement between pulses

Quantum entanglement describes correlations between distinct subsystems that cannot be explained by classical physics and that arise from the nonseparability of the joint quantum state [102, 103]. The conceptual origin of entanglement can be traced to the Einstein-Podolsky-Rosen (EPR) paradox. In its original formulation, the EPR argument [104] considers two spatially separated systems prepared in a correlated state. If the value of one observable of the first system can be predicted with certainty by measuring the second system, then this observable is considered an element of reality. If this holds simultaneously for non-commuting observables, then the quantum mechanical description appears incomplete. The EPR paradox was originally presented as a critique of quantum mechanics, but it later became a cornerstone for understanding nonclassical correlations.

In modern quantum information theory, entanglement is no longer viewed as a sign of incompleteness, but as a well-defined physical resource [103, 105, 106]. It is a central resource in quantum information science, where it enables tasks that are impossible or inefficient using classical correlations alone. In this section, the focus is on continuous-variable entanglement realized in optical systems.

Continuous variable systems are quantum systems whose observables have continuous spectra. In quantum optics, such systems arise naturally from bosonic modes of the electromagnetic field. Each optical mode can be modeled as a quantum harmonic oscillator, and its physical observables are given by field quadratures.

Continuous-variable entanglement appears as nonclassical correlations between the states and observables (e.g., field quadratures) of different optical modes. These correlations can be estimated using well-studied homodyne detection [107, 108]. As a result, such systems are widely used in optical implementations of quantum communication, quantum key distribution, and quantum-enhanced

metrology [109, 110].

The two-mode squeezed vacuum (TMSV) state $|\xi\rangle$ is an emblematic example of continuous-variable entangled states. In this state, the quantum noise of two optical modes is strongly correlated. Fluctuations of one quadrature in the first mode are correlated with the corresponding quadrature of the second mode, while the conjugate quadratures are anticorrelated. The strength of these correlations increases with the squeezing parameter ξ . In the limit of infinite squeezing, the TMSV approaches the idealized EPR state discussed in the original paradox [111, 112].

Two-mode squeezed vacuum states can be generated using nondegenerate optical parametric oscillators. Alternatively, they can be produced by interfering two single-mode squeezed states on a balanced beam splitter [113]. In the photon-number basis, the TMSV state can be written as

$$|\xi\rangle = \cosh^{-1} \xi \sum_{n=0}^{\infty} (-\tanh \xi)^n |n, n\rangle. \quad (6.1)$$

where $|n, n\rangle$ is the Fock state with n photons at each mode.

Simon certifier. Detecting entanglement in continuous-variable systems requires criteria that can distinguish separable states from entangled states. The fundamental conceptual basis for separability in bipartite quantum systems is given by the Peres-Horodecki criterion [114]. This criterion states that any separable quantum state must remain a valid physical state after partial transposition with respect to one subsystem. In general infinite-dimensional Hilbert spaces, this condition is necessary but not sufficient for separability. However, Simon showed that for two-mode Gaussian states such as the TMSV state the partial transposition criterion is both necessary and sufficient for separability [115, 116]. This makes the

Simon criterion a useful and complete tool for Gaussian entanglement detection for TMSV states.

The effect of atmospheric turbulence on continuous-variable entanglement depends on temporal correlations of the channel transmittance. The limiting cases of fully correlated transmittances, corresponding to time separation $\tau \rightarrow 0$, and fully anticorrelated transmittances, corresponding to large time separation $\tau \rightarrow \infty$, have been analyzed previously in Ref. [98]. We focus on the intermediate regime, where the time interval between subsequent pulses τ is finite.

We consider a two-mode squeezed vacuum state as the entangled source. The first mode is transmitted through the atmospheric channel at time $t = 0$. The second mode is stored in a quantum memory and transmitted at a later time $t = \tau$. As a result, the two modes experience different but temporally correlated realizations of the atmospheric channel.

For the simulations, we use the same atmospheric channels as defined in Section 5. Deterministic losses of 0.1 dB/km are additionally included in the effective transmittances η_0 and η_τ [117], together with losses of the optical system. When measurements are performed using homodyne detection, the local oscillator is transmitted in the same spatial mode as the signal with orthogonal polarization, ensuring a stable phase reference while experiencing the same atmospheric fluctuations [118–120].

To analyze entanglement preservation in this scenario, we apply the Simon criterion to the two-mode squeezed vacuum state after transmission through the atmospheric channels. For the considered model, the Simon certifier \mathcal{W} takes the form

$$\begin{aligned} \mathcal{W} = & \sinh^2 \xi \left[- \langle \sqrt{\eta_0 \eta_\tau} \rangle^2 \cosh^2 \xi + \langle \eta_0 \rangle \langle \eta_\tau \rangle \sinh^2 \xi \right] \\ & \times \left[1 - \frac{\langle \sqrt{\eta_0 \eta_\tau} \rangle^2}{4} \sinh^2 2\xi \right. \\ & \left. + \sinh^2 \xi \left(\langle \eta_0 \rangle + \langle \eta_\tau \rangle + \langle \eta_0 \rangle \langle \eta_\tau \rangle \sinh^2 \xi \right) \right]. \end{aligned} \quad (6.2)$$

According to the Simon criterion, the transmitted state manifests Gaussian entanglement if and only if $\mathcal{W} < 0$.

The expression for \mathcal{W} factorizes into two multiplicative factors. The second factor is strictly positive for all physically allowed values of the transmittances and the squeezing parameter. As a result, it cannot influence the sign of \mathcal{W} and can be omitted when determining the entanglement condition. Therefore, the sign of \mathcal{W} is fully determined by the first factor. Importantly, this factor is invariant under a global rescaling of the transmittances η_0 and η_τ . This implies that entanglement preservation is independent of deterministic losses, including losses introduced by the quantum memory and the optical system.

[Figure 6.1](#) shows the regions of entanglement preservation for a TMSV state transmitted through atmospheric channels. The horizontal axis represents the wind-driven shift s , which corresponds to the time separation between pulses $\tau = s/v$, where v is the transverse wind speed (see [Section 5](#)). The vertical axis shows the squeezing parameter ξ of the initial TMSV state. The shaded regions correspond to $\mathcal{W} < 0$, where the Simon criterion certifies that the received state remains entangled. The figure also renders a counterintuitive feature: increasing the squeezing parameter ξ reduces the maximum wind-driven shift for which entanglement is preserved [\[98\]](#). As a result, stronger squeezing does not improve entanglement robustness in atmospheric channels.

For a squeezing parameter of $\xi = 2$ and a turbulence strength of $\sigma_R^2 = 11$, Gaussian entanglement remains for wind-driven shifts up to $s = 6.4$ cm, corresponding to a time separation of $\tau = 6.4$ ms for a transverse wind speed of $v = 10$ m/s. This demonstrates that entanglement between light pulses is highly robust, persisting beyond millisecond time intervals. However, losses associated with the quantum memory can significantly reduce the absolute value of the Simon certifier.

In [Section 5](#), we introduced the spatial coherence radius ρ_0 , which

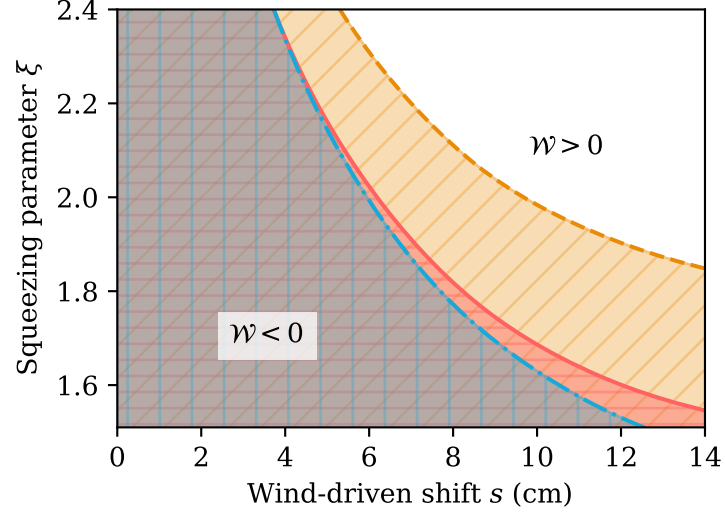


Figure 6.1 – Regions of entanglement preservation for a two-mode squeezed vacuum (TMSV) state as a function of the wind-driven shift s and the initial squeezing parameter ξ . Threshold boundaries ($\mathcal{W} = 0$) are shown for $\sigma_R^2 = 5.5$, $\sigma_R^2 = 11$, and $\sigma_R^2 = 16.5$ (dashed, solid, and dot-dashed lines, respectively). The shaded areas indicate the regime where the Simon certifier \mathcal{W} is negative, indicating that the state remains entangled after transmission. The aperture radius is $R_{\text{ap}} = 20$ cm.

characterizes the correlation of transmittances and depends on the receiver aperture radius R_{ap} . The threshold wind-driven shift s_{th} , defined as the maximum shift for which entanglement is preserved ($\mathcal{W} < 0$), also depends on R_{ap} . Figure 6.2 shows s_{th} as a function of the coherence radius ρ_0 . The figure shows that $s_{\text{th}}(\rho_0)$ is a monotonically increasing, nonlinear function. Larger coherence allows entanglement to survive larger wind-driven shifts. At the same time, the threshold decreases with increasing squeezing. The nonlinear behavior highlights the nontrivial interplay between initial squeezing, channel correlations, and receiver geometry in determining entanglement robustness.

In summary, we have introduced and quantified the time interval over which entanglement between pulses is preserved, and analyzed how it depends on channel aperture, coherence radius, and squeezing. Gaussian entanglement is robust against atmospheric turbulence, while stronger squeezing does not improve its survival. Deterministic losses affect only the absolute value of the certifier. These results provide a practical guideline for maintaining continuous-variable entanglement in

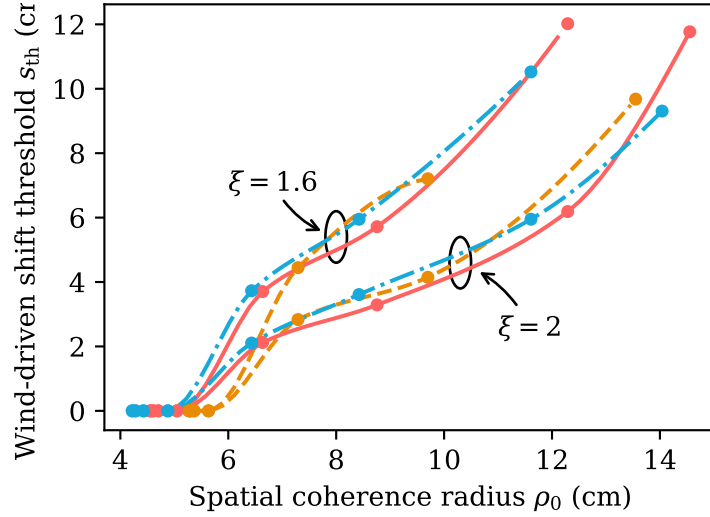


Figure 6.2 – The threshold wind-driven shift s_{th} at which entanglement is lost, against the spatial coherence radius ρ_0 for channels with $\sigma_R^2 = 5.5$, $\sigma_R^2 = 11$, and $\sigma_R^2 = 16.5$ (dashed, solid, and dot-dashed lines, respectively). The monotonic increase confirms that larger receiver apertures directly extend the time interval during which entanglement is preserved, however the dependence is nonlinear.

realistic free-space quantum channels.

6.2 Discrete-variable entanglement between pulses

In the previous section, entanglement was discussed in the continuous-variable regime. This description is natural for Gaussian states and homodyne measurements. However, many experimentally relevant sources and protocols operate in a finite-dimensional Hilbert space, where entanglement can be encoded in discrete degrees of freedom. This motivates a separate treatment of discrete-variable entanglement.

We consider a maximally entangled two-qubit system corresponding to a Bell state. Each qubit is encoded in the polarization degree of freedom of a single photon occupying a well-defined temporal mode. The horizontal polarization h defines the logical zero state, while the vertical polarization v defines the logical one. Using

two temporal modes $t = 0$ and $t = \tau$, the system spans four optical modes, namely $h0$, $v0$, $h\tau$, and $v\tau$. The corresponding Bell state is written as

$$\begin{aligned} |\mathcal{B}\rangle &= \frac{1}{\sqrt{2}} \left(|h\rangle_0 |v\rangle_\tau - |v\rangle_0 |h\rangle_\tau \right) \\ &= \frac{1}{\sqrt{2}} \left(|1\rangle_{h0} |0\rangle_{v0} |0\rangle_{h\tau} |1\rangle_{v\tau} - |0\rangle_{h0} |1\rangle_{v0} |1\rangle_{h\tau} |0\rangle_{v\tau} \right), \end{aligned} \quad (6.3)$$

where the terms $|1\rangle$ and $|0\rangle$ denote the presence or absence of a single photon within each respective polarization-temporal mode, and $|h\rangle$ and $|v\rangle$ are the single-photon states in the horizontally and vertically polarized modes.

In optical implementations, entangled photon pairs are often generated through a nonlinear light-matter interaction such as spontaneous parametric down-conversion (PDC) [113, 121]. A PDC source produces a superposition of photon-number states. In the relevant polarization and temporal modes, this superposition can be written as

$$|\text{PDC}\rangle = (\cosh \xi)^{-2} \sum_{n=0}^{+\infty} \sqrt{n+1} \tanh^n \xi |\Phi_n\rangle \quad (6.4)$$

with

$$|\Phi_n\rangle = \frac{1}{\sqrt{n+1}} \sum_{m=0}^n (-1)^m |n-m\rangle_{h0} |m\rangle_{v0} |m\rangle_{h\tau} |n-m\rangle_{v\tau}, \quad (6.5)$$

where the terms $|n\rangle$ denote the presence of n photons within the respective polarization-temporal modes, and the parameter ξ is determined by the pump power and the nonlinear coupling strength. The term with $n = 1$ corresponds to the polarization Bell state occupying the two temporal modes, while higher-order terms describe the simultaneous emission of multiple photon pairs. In this section, we analyze the entanglement between optical pulses separated by a time interval τ for both the ideal Bell state and the PDC state [122, 123].

To quantify discrete-variable entanglement, we use the Bell parameter \mathcal{B} , defined in the Clauser-Horne-Shimony-Holt form [124]. It is constructed from correlations between measurements on two parts in different bases. A value of $\mathcal{B} > 2$ signals a violation of local realism and confirms the presence of entanglement.

Several studies have investigated the distribution of discrete-variable entanglement through turbulent free-space channels. A theoretical framework describing the propagation of polarization entanglement through atmospheric turbulence was developed in Ref. [125] for both Bell states and PDC states. In that work, the entanglement degradation was described in terms of statistical moments of the transmittance.

The role of temporal correlations in the atmospheric channel was further analyzed in Ref. [126], where two limiting propagation scenarios were considered. The case of copropagation corresponds to perfectly correlated transmittance fluctuations and is observed in the limit $\tau \rightarrow 0$. The opposite limit of counterpropagation corresponds to statistically independent fluctuations and is obtained for $\tau \rightarrow \infty$. These two regimes provide useful benchmarks but do not describe intermediate situations where correlations are only partial.

Experimental feasibility of distributing polarization entanglement through strong turbulence channels was demonstrated in Ref. [127]. That experiment confirmed that polarization entanglement can survive high-loss free-space propagation. However, the temporal separation between consecutive pulses was on the order of 50ns, which is much shorter than the atmospheric correlation time. As a result, the corresponding transmittance fluctuations were almost perfectly correlated between the two pulses.

In realistic free-space quantum communication scenarios, the temporal separation between entangled pulses may become comparable to or larger than the atmospheric correlation time. In this regime, transmittance fluctuations are neither fully correlated nor fully independent. Consequently, the measured Bell parameter

becomes a nontrivial function of the pulse separation time τ . Determining this dependence is essential for understanding entanglement distribution under realistic channel conditions and for assessing the robustness of Bell inequality violations in random media.

For the numerical simulations, we employ the same atmospheric channel model as defined in [Section 5](#). The first mode is transmitted through the atmospheric channel at time $t = 0$. The second mode is stored in a quantum memory and is transmitted at a later time $t = \tau$ [[128](#), [129](#)].

In contrast to the continuous-variable case, the discrete-variable description requires an explicit account of all deterministic losses. Losses directly affect the detection probabilities and therefore enter the evaluation of the Bell parameters. As a result, each optical and detection component must be included in the channel model.

The total deterministic loss amounts to 9.42 dB and consists of:

- atmospheric attenuation of 0.1 dB/km over a propagation distance of 50 km, resulting in a loss of 5 dB
- a 50:50 beam splitter, introducing a loss of $10 \log_{10}(1/2) = 3$ dB
- detector efficiency of 0.85, corresponding to a loss of $10 \log_{10}(0.85) = 0.71$ dB
- quantum memory writing efficiency of 0.85, corresponding to a loss of 0.71 dB

In addition to these static contributions, the quantum memory readout exhibits a time-dependent loss. It is modeled as an effective attenuation of 3 dB/ms of storage time, which directly depends on the pulse separation time τ . Noise counts originating from detector dark counts and stray light are included in the simulation $\nu = 3 \times 10^{-4}$.

The dependence of the Bell parameter \mathcal{B} on the temporal separation between pulses τ is shown in [Fig. 6.3](#) for both the ideal Bell state and the parametric down-conversion state. For the PDC state, the Bell parameter additionally depends on the source parameter ξ . In the simulations, we optimize over ξ by choosing the

value that maximizes \mathcal{B} for each separation τ .

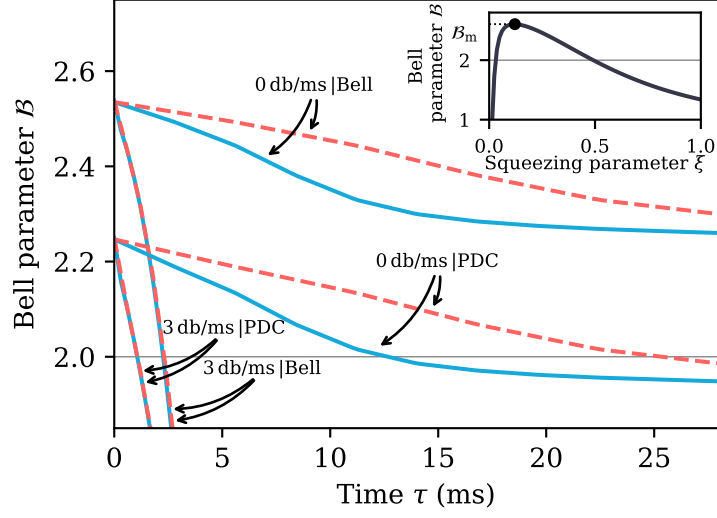


Figure 6.3 – Bell parameter \mathcal{B} as a function of the pulse separation time τ for polarization-entangled states. Results compare the ideal Bell state with the parametric down-conversion (PDC) state, optimized for the squeezing parameter ξ . The channel with $\sigma_R^2 = 11$ and $R_{\text{ap}} = 10$ cm with wind speeds $v = 5$ m/s (dashed line) and $v = 10$ m/s (solid lines) are analysed.

Because of time-dependent losses in the channel, the wind-driven shift s cannot be treated as interchangeable with the pulse time separation τ . To account for this effect, we consider two wind speeds, $v = 10$ and $v = 5$. To isolate the impact of time-dependent quantum memory losses from atmospheric effects, we also show results for an ideal quantum memory with perfect readout efficiency of 0 dB/ms.

From the results, it is apparent that atmospheric turbulence alone allows discrete-variable entanglement to survive over pulse separations of tens of milliseconds. Quantum correlations persisting over such long times indicate that using two or more time-separated quantum states makes it possible to increase the effective dimensionality of the Hilbert space for the transmitted states. However, the introduction of quantum memory losses strongly reduces the viable pulse separation to a few milliseconds. These findings indicate that the feasibility of the protocol is currently limited by hardware efficiency. They emphasize that developing high-performance quantum memories is important for practical implementation.

6.3 Threshold-based selection for nonclassical states

While entanglement fundamentally involves multipartite correlations, optical nonclassicality is an intrinsic property that can arise within a single-mode optical field. It characterizes quantum states whose statistical properties cannot be reproduced by classical electrodynamics. Coherent states form a prominent subset of the classical class [9]. They minimize the Heisenberg uncertainty relation

$$(\Delta X)^2(\Delta P)^2 \geq \frac{1}{4} \quad (6.6)$$

with equal variance in both quadratures, representing the minimum symmetric noise allowed by quantum mechanics. Despite this property, coherent states remain classical since their fluctuations can be reproduced by classical stochastic models.

A systematic characterization of nonclassicality is provided by the Glauber Sudarshan P function [19, 20] (see [Section 1.1](#)). If the P function is positive semidefinite, the state is considered classical. Otherwise, it is nonclassical, meaning the state exhibits negativity of the P function. These features indicate the failure of description in terms of classical electrodynamics. The absence of positive semidefiniteness of the P function provides a clear qualitative criterion, but it is not unique as a quantitative measure. Several nonclassicality measures have been proposed that capture different operational aspects of this property [130]. Their relevance depends on the task under consideration.

Historically, the first unambiguous experimental signature of nonclassical light was photon antibunching [8] (see [Section 1.1](#)). This effect cannot be explained by classical intensity fluctuations and directly contradicts classical field theories. Squeezed states represent another important class of nonclassical states. In these states, the noise of one quadrature is reduced below the vacuum level, while the noise of the conjugate quadrature increases to satisfy the uncertainty relation (see

Eq. (6.6)).

In this section, we study the propagation of squeezed states through an atmospheric channel. We consider the threshold selection of the transmittance as a method to improve the preservation of nonclassical properties in atmospheric channels [97, 101]. This approach exploits fluctuations of the channel transmittance η_t to conditionally enhance nonclassical features of the transmitted light.

We consider amplitude-squeezed coherent states and quantify nonclassicality using the Mandel parameter [9], the Binomial Q parameter [131], and the convex-geometry approach [132]. The Binomial Q parameter generalizes the Mandel parameter to account for realistic detectors, such as arrays of on/off detectors, while the convex-geometry approach enables testing nonclassicality in situations where standard approaches fail. Nonclassicality certifiers are studied as functions of the time interval between the classical probe pulse and the quantum pulse, τ , using the results of Section 5.

6.3.1 Amplitude-squeezed coherent state with adaptive selection

In this section, we study amplitude-squeezed coherent states, which is defined as a squeezed vacuum displaced by a real amplitude α_0 in phase space, $|\alpha_0, \xi\rangle = \hat{D}(\alpha_0)\hat{S}(\xi)|0\rangle$. Amplitude-squeezed coherent states exhibit reduced photon-number fluctuations compared to a classical coherent state with the same mean intensity. While a coherent state shows a Poissonian photon-number distribution, amplitude squeezing leads to a narrower distribution. This reduction of photon-number fluctuations is a direct signature of nonclassicality. This means that nonclassicality can be assessed using photon-number statistics, avoiding balanced homodyne detection with its requirement of phase-stable reference fields and complex measurement setups.

Nonclassicality in such situations is commonly characterized by the Mandel

parameter

$$Q = \frac{\langle \Delta \hat{n}^2 \rangle}{\langle \hat{n} \rangle} - 1. \quad (6.7)$$

Negative values of Q correspond to sub-Poissonian photon-number statistics and therefore to nonclassical light. This criterion relies on ideal photon-number-resolving detection and is therefore of limited applicability in realistic measurement scenarios.

A more realistic detection model is based on an array of N “on-off” detectors [133, 134]. In such a setup, the incoming beam is split into N separate modes using a balanced interferometer, where each mode is then incident on an independent detector. These detectors are “on-off” type, meaning they can only discriminate between the absence and the presence of photons, rather than resolving the exact photon number. For a classical coherent state with complex amplitude α , the resulting click statistics are binomial.

The corresponding probability distribution for click number m , given coherent state α , reads (see Ref. [135])

$$\Pi(m|\alpha) = \binom{N}{m} \left(1 - e^{-|\alpha|^2/N}\right)^m e^{-(N-m)|\alpha|^2/N}. \quad (6.8)$$

This measurement captures the finite resolution of practical photon counting devices and reduces to ideal photon-number-resolving detection in the limit $N \rightarrow \infty$. In this setting, nonclassicality can be detected via sub-binomial click statistics. The corresponding parameter for such measurement is [131]

$$Q_N = N \frac{\langle \Delta c^2 \rangle}{\langle c \rangle (N - \langle c \rangle)} - 1, \quad (6.9)$$

where c denotes the number of clicks. Negative values of Q_N indicate nonclassical light. The described criteria provide sufficient but not necessary conditions for

nonclassicality. There exist nonclassical states whose click statistics remain classical.

A more general method based on inequalities for detecting nonclassicality was introduced in Ref. [136]. If there exists such a function $\lambda(m)$ that the inequality

$$\sum_{m=0}^{N-1} \lambda(m) P(m) \leq \sup_{\alpha \in \mathbb{C}} \sum_{m=0}^{N-1} \lambda(m) \Pi(m|\alpha) \quad (6.10)$$

is violated, the statistics are necessarily nonclassical. Here $P(m)$ is the measured click distribution. We use the optimal sets of $\lambda(m)$ determined for array detectors with $N = 2, 3, 5$ [132], which provide a practical tool, based on convex geometry, for reliably detecting nonclassicality in realistic measurement setups.

Using the results of the channel simulations obtained in Section 5 for different values of time between classical probe and quantum pulse, we apply an adaptive selection strategy to preserve nonclassicality in atmospheric conditions. We study the maximal time interval for a given threshold transmittance η_{\min} during which the click statistics remain nonclassical.

Figure 6.4 shows the wind-driven spatial shift s , corresponding to a temporal delay $\tau = s/v$ between the classical probe and the quantum pulse, at which different nonclassicality criteria no longer indicate nonclassicality. The Mandel parameter Q reaches zero at $s = 7.2$ cm, indicating the limit of sub-Poissonian photon statistics for an ideal photon-number-resolving detector. For arrays of on-off detectors, the sub-binomial parameters Q_N reach zero at larger shifts: $Q_5 = 9.7$ cm, $Q_3 = 11.4$ cm, and $Q_2 = 14.2$ cm. While Q_N approaches Q as N increases, in the considered case smaller detector arrays detect nonclassicality for longer time intervals. However, for other state parameters ($\xi = 0.16$ and $\alpha_0 = 1.4$), the trend reverses, and larger detector arrays maintain nonclassicality over longer times.

The figure also shows the difference between the left- and right-hand sides of the inequalities (see Eq. (6.10)), which quantifies the distance of the click statistics from the convex hull of coherent state click statistics. When this difference reaches

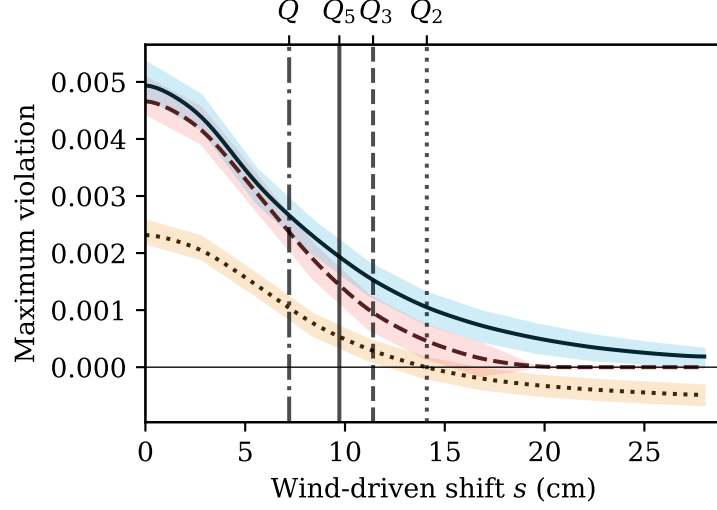


Figure 6.4 – Maximum wind-driven shift s for which nonclassicality remains detectable in an amplitude-squeezed coherent state ($\alpha_0 = 1.15, \xi = 0.59$). The simulation assumes a moderate turbulence regime ($\sigma_R^2 = 11$), a receiver aperture $R_{\text{ap}} = 30$ cm, and total deterministic losses of 6 dB. An adaptive selection strategy is applied with a threshold transmittance $\eta_{\text{min}} = 0.1$. The plot compares the ideal Mandel parameter Q against sub-binomial parameters Q_N and witnesses for detector arrays of size $N = 2, 3$, and 5. Confidence intervals are derived from 10^6 selected samples.

zero, the click statistics can no longer be considered nonclassical. The inequalities reach zero at $s = 14.2$ cm for $N = 2$, $s = 19.6$ cm for $N = 3$, and exceed $s = 28$ cm for $N = 5$, which is the maximal value covered by the simulations. Notably, for $N = 2$, the sub-binomial parameter Q_2 reaches zero at the same spatial shift as the inequality, indicating a deeper connection between these two nonclassicality criteria for small detector arrays. Overall, these results show that the convex-geometry witnessing provides a robust detection of nonclassicality over extended time delays.

6.4 Summary

The analysis presented in this section characterizes the robustness of quantum correlations and nonclassicality in atmospheric channels. We demonstrated that

Gaussian entanglement between light pulses persists over millisecond timescales. Its preservation increases monotonically with the spatial coherence radius, although nonlinear features are observed.

Discrete-variable entanglement exhibits a distinct behavior, depending on both temporal correlations and deterministic losses. Time-dependent losses in current quantum memories significantly restrict the viable pulse separation. Simulations indicate that atmospheric coherence alone allows delays of tens of milliseconds, whereas memory decay reduces this to a few milliseconds. This discrepancy highlights the need for high-efficiency storage components.

The study of single-mode nonclassicality emphasizes the utility of adaptive selection techniques. By monitoring a classical probe pulse, quantum transmission events can be conditionally selected during periods of high transmittance. The Beta-distribution PDT model accurately predicts the nonclassicality of squeezed states under postselection in the limit of instantaneous adaptive selection ($\tau \rightarrow 0$). For finite τ , two-time analytical PDT models are required, but such models are currently lacking. Numerical studies of amplitude-squeezed states show that adaptive selection improves nonclassicality even for pulse separations of tens of milliseconds. Nonclassicality witnessing based on the convex-geometry method provides a more sensitive measure of nonclassicality in this context.

In summary, temporal correlations in atmospheric quantum channels provide a window for effective quantum communication. Exploiting these correlations increases the effective Hilbert-space dimensionality and allows adaptive selection strategies to significantly improve nonclassicality preservation.

Conclusions

This thesis addressed the statistical modeling of quantum optical channels in the turbulent atmosphere, including a study of corresponding temporal correlations. We established a numerical framework based on the sparse-spectrum phase-screen method to simulate beam propagation through a turbulent atmosphere. This approach mitigates low-frequency undersampling inherent in standard techniques, thereby enabling comprehensive analysis of stochastic wave propagation dynamics. This framework allowed us to investigate transmittance statistics across weak, moderate, and strong turbulence regimes, including model validation and assessment of quantum entanglement preservation limits in a turbulent atmosphere. Its code is publicly available and has attracted interest from the community.

Systematic validation revealed that receiver aperture size relative to the average beam radius dictates model accuracy more strongly than turbulence strength alone. Small apertures induce positive skewness favoring the truncated lognormal model, whereas large apertures produce negative skewness described by beam-wandering or elliptical-beam approximations. The empirical Beta distribution generally outperformed analytical alternatives due to its bounded support on $[0, 1]$ and flexibility in capturing skewness transitions. This finding clarifies an important aspect of PDT statistical behavior and establishes the aperture-to-beam ratio as the primary design criterion for optical links.

Underlying assumptions. Numerical results indicate that while the beam centroid follows a two-dimensional Gaussian distribution in weak and moderate turbulence, it exhibits slightly platykurtic characteristics under strong conditions. Furthermore, the assumption of statistical independence between the beam centroid and shape fluctuations is violated, especially in strong turbulence regimes. Logarithms of the beam semi-axes also deviate from bivariate Gaussian distributions, showing suppression along the diagonal where axes are equal. These deviations indicate that analytical models relying on these simplified assumptions introduce

systematic errors in transmittance prediction. This necessitates explicit correction in subsequent analytical frameworks.

Transmittance-matching technique. We identified a fundamental flaw in beam-shape-based models such as beam-wandering and elliptical-beam approximations. Standard geometric assumptions about the beam shape cannot account for complex shape evolution after propagation through the turbulent atmosphere, leading to the misspecification bias inherent in such models. This deficiency manifests as systematic biases in predicted average transmittance moments. To resolve this issue, we introduced a Transmittance-Moment Matching technique applied specifically to the circular-beam approximation. The corrected model significantly improved agreement with numerical simulations compared to standard beam-based alternatives. Consequently, this correction represents a significant advancement in physically grounded modeling for atmospheric channels.

Temporal correlations. The existing framework of the PDT is insufficient for describing high-repetition-rate systems where temporal correlations persist between consecutive pulses. Therefore, we introduced a Two-Time PDT framework $\mathcal{P}(\eta_0, \eta_\tau)$ to capture the joint statistics of transmittance values at different times. A key parameter defined within this framework is the aperture-averaged spatial coherence radius ρ_0 , marking the wind-shift displacement where the Pearson correlation decays to e^{-1} . This spatial coherence radius scales linearly with aperture size, serving as a practical criterion for determining optimal pulse repetition rates.

Quantum properties. Applications to continuous-variable quantum protocols demonstrated that Gaussian entanglement persists over millisecond timescales. Discrete-variable entanglement survives atmospheric turbulence for tens of milliseconds, though practical limits reduce this to a few milliseconds due to quantum memory readout losses. Adaptive selection using classical probe pulses improves the preservation of nonclassicality over pulse separations of tens of milliseconds. These results quantify the temporal resources available for time-bin encoding and

correlation-aware communication strategies.

Limitations. Atmospheric quantum channels depend on numerous physical parameters, making a fully comprehensive description impractical. Consequently, we restricted our attention to a minimal set sufficient to isolate core effects, prioritizing physical understanding over system-specific details. For example, the transmitter optical field is modeled as a Gaussian beam without explicitly considering higher-order spatial modes, and the receiver aperture is assumed to be circular, rather than accounting for specific optical configurations (e.g., Cassegrain). Turbulence parameters are treated as constant along horizontal propagation paths. These constraints are necessary for the systematic analysis conducted in this work. For any subsequent developments, the simulation framework can be readily adapted to incorporate more intricate channel properties.

A second category of limitations arises from the intrinsic complexity of the real turbulent atmosphere. Unlike the stationary Kolmogorov-based descriptions employed here, actual atmospheric dynamics are non-stationary and exhibit intermittency, characterized by abrupt fluctuations separated by variable intervals. These features impose fundamental constraints on modeling accuracy that apply universally to all Kolmogorov-based theoretical frameworks.

Ultimately, this thesis establishes a rigorous framework for evaluating long-distance atmospheric communication under controlled conditions. While restricted to a minimal set of physical parameters, this approach isolates core stochastic effects critical for system design. This capability is essential for engineering robust quantum protocols where fiber transmission is prohibitive. Consequently, the work provides a theoretical foundation for designing robust atmospheric quantum channels under varying turbulence conditions.

Bibliography

- [1] M. Born and E. Wolf, *Principles of Optics: Electromagnetic Theory of Propagation, Interference and Diffraction of Light* (CUP Archive, Feb. 28, 2000), 996 pp.
- [2] J. Jackson, *Classical electrodynamics* (Wiley, 1998).
- [3] M. O. Scully and M. Sargent, “The concept of the photon”, [Physics Today](#) **25**, 38–47 (1972).
- [4] W. E. Lamb and M. O. Scully, “The photoelectric effect without photons”, in *Polarization, matter and radiation: Jubilee volume in honour of alfred kastler* (1969), pp. 363–369.
- [5] G. I. Taylor, “Interference fringes with feeble light”, *Proceedings of the Cambridge Philosophical Society* **15**, 114 (1909).
- [6] J. C. Slater, “A Quantum Theory of Optical Phenomena”, [Physical Review](#) **25**, 395–428 (1925).
- [7] H. J. Kimble and L. Mandel, “Theory of resonance fluorescence”, [Physical Review A](#) **13**, 2123–2144 (1976).
- [8] H. J. Kimble, M. Dagenais, and L. Mandel, “Photon Antibunching in Resonance Fluorescence”, [Physical Review Letters](#) **39**, 691–695 (1977).
- [9] L. Mandel and E. Wolf, eds., *Optical coherence and quantum optics* (Cambridge University Press, Cambridge, 1995).
- [10] R. E. Slusher, L. W. Hollberg, B. Yurke, J. C. Mertz, and J. F. Valley, “Observation of Squeezed States Generated by Four-Wave Mixing in an Optical Cavity”, [Physical Review Letters](#) **55**, 2409–2412 (1985).
- [11] C. K. Hong, Z. Y. Ou, and L. Mandel, “Measurement of subpicosecond time intervals between two photons by interference”, [Physical Review Letters](#) **59**, 2044–2046 (1987).
- [12] A. Aspect, P. Grangier, and G. Roger, “Experimental Tests of Realistic Local Theories via Bell’s Theorem”, [Physical Review Letters](#) **47**, 460–463 (1981).

- [13] W. Tittel, J. Brendel, B. Gisin, T. Herzog, H. Zbinden, and N. Gisin, “Experimental demonstration of quantum correlations over more than 10 km”, [Physical Review A **57**, 3229–3232 \(1998\)](#).
- [14] G. Weihs, T. Jennewein, C. Simon, H. Weinfurter, and A. Zeilinger, “Violation of Bell’s Inequality under Strict Einstein Locality Conditions”, [Physical Review Letters **81**, 5039–5043 \(1998\)](#).
- [15] B. Hensen, H. Bernien, A. E. Dréau, A. Reiserer, N. Kalb, M. S. Blok, J. Ruitenberg, R. F. L. Vermeulen, R. N. Schouten, C. Abellán, et al., “Loophole-free Bell inequality violation using electron spins separated by 1.3 kilometres”, [Nature **526**, 682–686 \(2015\)](#).
- [16] N. Brunner, D. Cavalcanti, S. Pironio, V. Scarani, and S. Wehner, “Bell nonlocality”, [Reviews of Modern Physics **86**, 419–478 \(2014\)](#).
- [17] R. J. Glauber, “The Quantum Theory of Optical Coherence”, [Physical Review **130**, 2529–2539 \(1963\)](#).
- [18] L. Mandel and E. Wolf, “Coherence Properties of Optical Fields”, [Reviews of Modern Physics **37**, 231–287 \(1965\)](#).
- [19] R. J. Glauber, “Photon Correlations”, [Physical Review Letters **10**, 84–86 \(1963\)](#).
- [20] E. C. G. Sudarshan, “Equivalence of Semiclassical and Quantum Mechanical Descriptions of Statistical Light Beams”, [Physical Review Letters **10**, 277–279 \(1963\)](#).
- [21] J. Klauder and B. Skagerstam, *Coherent States: Applications in Physics and Mathematical Physics* (WORLD SCIENTIFIC, Apr. 1985).
- [22] L. Mandel, “Non-Classical States of the Electromagnetic Field”, [Physica Scripta **T12**, 34–42 \(1986\)](#).
- [23] J. Sperling and W. Vogel, “Quasiprobability distributions for quantum-optical coherence and beyond”, [Physica Scripta **95**, 034007 \(2020\)](#).

- [24] L. Cohen, “Generalized Phase-Space Distribution Functions”, [Journal of Mathematical Physics](#) **7**, 781–786 (1966).
- [25] W. K. Wootters and W. H. Zurek, “A single quantum cannot be cloned”, [Nature](#) **299**, 802–803 (1982).
- [26] N. Gisin and R. Thew, “Quantum communication”, [Nature Photonics](#) **1**, 165–171 (2007).
- [27] G. B. Xavier, J.-Å. Larsson, P. Villoresi, G. Vallone, and A. Cabello, “Energy-time and time-bin entanglement: past, present and future”, [npj Quantum Information](#) **11**, 129 (2025).
- [28] L. Allen, M. W. Beijersbergen, R. J. C. Spreeuw, and J. P. Woerdman, “Orbital angular momentum of light and the transformation of Laguerre-Gaussian laser modes”, [Physical Review A](#) **45**, 8185–8189 (1992).
- [29] V. I. Tatarski, R. A. Silverman, and N. Chako, “*Wave Propagation in a Turbulent Medium*”, [Physics Today](#) **14**, 46–51 (1961).
- [30] R. Fante, “Electromagnetic beam propagation in turbulent media”, [Proceedings of the IEEE](#) **63**, 1669–1692 (1975).
- [31] L. C. Andrews and R. L. Phillips, *Laser Beam Propagation through Random Media* (SPIE, 1000 20th Street, Bellingham, WA 98227-0010 USA, Sept. 16, 2005).
- [32] W. T. Buttler, R. J. Hughes, P. G. Kwiat, S. K. Lamoreaux, G. G. Luther, G. L. Morgan, J. E. Nordholt, C. G. Peterson, and C. M. Simmons, “Practical Free-Space Quantum Key Distribution over 1 km”, [Physical Review Letters](#) **81**, 3283–3286 (1998).
- [33] R. J. Hughes, J. E. Nordholt, D. Derkacs, and C. G. Peterson, “Practical free-space quantum key distribution over 10 km in daylight and at night”, [New Journal of Physics](#) **4**, 43–43 (2002).
- [34] R. Ursin, F. Tiefenbacher, T. Schmitt-Manderbach, H. Weier, T. Scheidl, M. Lindenthal, B. Blauensteiner, T. Jennewein, J. Perdigues, P. Trojek, et al.,

- “Entanglement-based quantum communication over 144 km”, [Nature Physics](#) **3**, 481–486 (2007).
- [35] P. Villoresi, T. Jennewein, F. Tamburini, M. Aspelmeyer, C. Bonato, R. Ursin, C. Pernechele, V. Luceri, G. Bianco, A. Zeilinger, et al., “Experimental verification of the feasibility of a quantum channel between space and Earth”, [New Journal of Physics](#) **10**, 033038 (2008).
- [36] C. Bonato, A. Tomaello, V. Da Deppo, G. Naletto, and P. Villoresi, “Feasibility of satellite quantum key distribution”, [New Journal of Physics](#) **11**, 045017 (2009).
- [37] S.-K. Liao, W.-Q. Cai, J. Handsteiner, B. Liu, J. Yin, L. Zhang, D. Rauch, M. Fink, J.-G. Ren, W.-Y. Liu, et al., “Satellite-Relayed Intercontinental Quantum Network”, [Physical Review Letters](#) **120**, 030501 (2018).
- [38] H. J. Kimble, “The quantum internet”, [Nature](#) **453**, 1023–1030 (2008).
- [39] A. Kolmogorov, “The Local Structure of Turbulence in Incompressible Viscous Fluid for Very Large Reynolds’ Numbers”, [Akademiia Nauk SSSR Doklady](#) **30**, 301–305 (1941).
- [40] V. Tatarskii, *The Effect of the Turbulent Atmosphere on Wave Propagation* (Israel Program for Scientific Translations, Jerusalem, 1971).
- [41] V. A. Banakh and V. L. Mironov, “Phase approximation of the Huygens–Kirchhoff method in problems of laser-beam propagation in the turbulent atmosphere”, [Optics Letters](#) **1**, 172 (1977).
- [42] R. A. Baskov and O. O. Chumak, “Laser-beam scintillations for weak and moderate turbulence”, [Physical Review A](#) **97**, 043817 (2018).
- [43] R. F. Lutomirski and H. T. Yura, “Propagation of a Finite Optical Beam in an Inhomogeneous Medium”, [Applied Optics](#) **10**, 1652 (1971).
- [44] M. Charnotskii, “Extended Huygens–Fresnel principle and optical waves propagation in turbulence: discussion”, [Journal of the Optical Society of America A](#) **32**, 1357 (2015).

- [45] J. M. Martin and S. M. Flatté, “Intensity images and statistics from numerical simulation of wave propagation in 3-D random media”, [Applied Optics](#) **27**, 2111 (1988).
- [46] R. Frehlich, “Simulation of laser propagation in a turbulent atmosphere”, [Applied Optics](#) **39**, 393–397 (2000).
- [47] J. D. Schmidt, *Numerical Simulation of Optical Wave Propagation with Examples in MATLAB* (SPIE, 1000 20th Street, Bellingham, WA 98227-0010 USA, July 12, 2010).
- [48] S. O. Rice, “Mathematical Analysis of Random Noise”, [Bell System Technical Journal](#) **23**, 282–332 (1944).
- [49] J. W. Strohbehn, T.-i. Wang, and J. P. Speck, “On the probability distribution of line-of-sight fluctuations of optical signals”, [Radio Science](#) **10**, 59–70 (1975).
- [50] G. Parry and P. N. Puaey, “K distributions in atmospheric propagation of laser light”, [Journal of the Optical Society of America](#) **69**, 796 (1979).
- [51] E. Jakeman and P. N. Pusey, “Significance of K Distributions in Scattering Experiments”, [Physical Review Letters](#) **40**, 546–550 (1978).
- [52] J. H. Churnside and R. G. Frehlich, “Experimental evaluation of log-normally modulated Rician and IK models of optical scintillation in the atmosphere”, [Journal of the Optical Society of America A](#) **6**, 1760 (1989).
- [53] M. A. Al-Habash, “Mathematical model for the irradiance probability density function of a laser beam propagating through turbulent media”, [Optical Engineering](#) **40**, 1554 (2001).
- [54] P. Diamant and M. C. Teich, “Photodetection of Low-Level Radiation through the Turbulent Atmosphere*”, [Journal of the Optical Society of America](#) **60**, 1489 (1970).

- [55] P. W. Milonni, J. H. Carter, C. G. Peterson, and R. J. Hughes, “Effects of propagation through atmospheric turbulence on photon statistics”, [Journal of Optics B: Quantum and Semiclassical Optics](#) **6**, S742–S745 (2004).
- [56] P. Hallbjomer, “Modified Rice distribution for signals with limited available power”, [IEEE Antennas and Wireless Propagation Letters](#) **2**, 159–162 (2003).
- [57] A. A. Semenov and W. Vogel, “Quantum light in the turbulent atmosphere”, [Physical Review A](#) **80**, 021802 (2009).
- [58] R. J. Glauber, “Coherent and Incoherent States of the Radiation Field”, [Physical Review](#) **131**, 2766–2788 (1963).
- [59] I. Capraro, A. Tomaello, A. Dall’Arche, F. Gerlin, R. Ursin, G. Vallone, and P. Villoresi, “Impact of Turbulence in Long Range Quantum and Classical Communications”, [Physical Review Letters](#) **109**, 200502 (2012).
- [60] D. Vasylyev, A. A. Semenov, and W. Vogel, “Atmospheric quantum channels with weak and strong turbulence”, [Physical Review Letters](#) **117**, 090501 (2016).
- [61] N. L. Johnson, S. Kotz, and N. Balakrishnan, “Continuous univariate distributions. 2”, in, 2. ed (Wiley, New York, 1995).
- [62] D. Yu. Vasylyev, A. A. Semenov, and W. Vogel, “Toward Global Quantum Communication: Beam Wandering Preserves Nonclassicality”, [Physical Review Letters](#) **108**, 220501 (2012).
- [63] D. Vasylyev, W. Vogel, and A. A. Semenov, “Theory of Atmospheric Quantum Channels Based on the Law of Total Probability”, [Physical Review A](#) **97**, 063852 (2018).
- [64] N. G. Kampen, *Stochastic Processes in Physics and Chemistry*, 3rd ed, North-Holland Personal Library (Elsevier Science & Technology, Amsterdam, 2011), 1 p.
- [65] A. M. Yaglom, *An Introduction to the Theory of Stationary Random Functions* (Courier Corporation, Jan. 1, 2004), 258 pp.

- [66] N. Wiener, “Generalized harmonic analysis”, [Acta Mathematica **55**, 117–258 \(1930\).](#)
- [67] A. Khintchine, “Korrelationstheorie der stationären stochastischen prozesse”, [Mathematische Annalen **109**, 604–615 \(1934\).](#)
- [68] E. N. Lorenz, “Deterministic Nonperiodic Flow”, [Journal of the Atmospheric Sciences **20**, 130–141 \(1963\).](#)
- [69] U. Frisch, *Turbulence: The Legacy of A.N. Kolmogorov*, 1st ed. (Cambridge University Press, Nov. 30, 1995).
- [70] J. Jiménez, “The Contributions of A. N. Kolmogorov to the theory of turbulence”, [Arbor **178**, 589–606 \(2004\).](#)
- [71] C. E. Coulman, J. Vernin, Y. Coqueugniot, and J. L. Caccia, “Outer scale of turbulence appropriate to modeling refractive-index structure profiles”, [Applied Optics **27**, 155 \(1988\).](#)
- [72] F. Martin, R. Conan, A. Tokovinin, A. Ziad, H. Trinquet, J. Borgnino, A. Agabi, and M. Sarazin, “Optical parameters relevant for High Angular Resolution at Paranal from GSM instrument and surface layer contribution”, [Astronomy and Astrophysics Supplement Series **144**, 39–44 \(2000\).](#)
- [73] R. J. Hill, S. F. Clifford, and R. S. Lawrence, “Refractive-index and absorption fluctuations in the infrared caused by temperature, humidity, and pressure fluctuations”, [Journal of the Optical Society of America **70**, 1192 \(1980\).](#)
- [74] L. Andrews, “An Analytical Model for the Refractive Index Power Spectrum and Its Application to Optical Scintillations in the Atmosphere”, [Journal of Modern Optics **39**, 1849–1853 \(1992\).](#)
- [75] R. J. Hill and S. F. Clifford, “Modified spectrum of atmospheric temperature fluctuations and its application to optical propagation”, [Journal of the Optical Society of America **68**, 892 \(1978\).](#)

- [76] G. I. Taylor, “The Spectrum of Turbulence”, [Proceedings of the Royal Society of London. Series A - Mathematical and Physical Sciences](#) **164**, 476–490 (1938).
- [77] J. Strohbehn, “Line-of-sight wave propagation through the turbulent atmosphere”, [Proceedings of the IEEE](#) **56**, 1301–1318 (1968).
- [78] A. E. Siegman, *Lasers* (University Science Books, Mill Valley, California, 1986), 1283 pp.
- [79] J. W. Goodman, *Introduction to Fourier optics*, Fourth edition (W.H. Freeman, Macmillan Learning, New York, 2017).
- [80] J. A. Fleck, J. R. Morris, and M. D. Feit, “Time-dependent propagation of high energy laser beams through the atmosphere”, [Applied physics](#) **10**, 129–160 (1976).
- [81] G. Strang, “On the Construction and Comparison of Difference Schemes”, [SIAM Journal on Numerical Analysis](#) **5**, 506–517 (1968).
- [82] J. W. Cooley and J. W. Tukey, “An algorithm for the machine calculation of complex Fourier series”, [Mathematics of Computation](#) **19**, 297–301 (1965).
- [83] C. Shannon, “Communication in the Presence of Noise”, [Proceedings of the IRE](#) **37**, 10–21 (1949).
- [84] R. G. Lane, A. Glindemann, and J. C. Dainty, “Simulation of a Kolmogorov phase screen”, [Waves in Random Media](#) **2**, 209–224 (1992).
- [85] N. A. Roddier, “Atmospheric wavefront simulation using Zernike polynomials”, [Optical Engineering](#) **29**, 1174 (1990).
- [86] L. Zhu, Y. Li, D. H. Zheng, and J. Wu, “Performance comparison of subharnomic and Zernike polynomials method for compensation of low-frequency components in FFT-based Von Karman phase screen”, in [2015 International Conference on Wireless Communications & Signal Processing \(WCSP\)](#) (Oct. 2015), pp. 1–5.

- [87] M. Charnotskii, “Sparse spectrum model for a turbulent phase”, [JOSA A **30**, 479–488 \(2013\)](#).
- [88] M. Charnotskii, “Statistics of the sparse spectrum turbulent phase”, [JOSA A **30**, 2455–2465 \(2013\)](#).
- [89] W. J. Conover and W. J. Conover, *Practical nonparametric statistics*, 3. ed, Wiley Series in Probability and Statistics Applied Probability and Statistics Section (Wiley, New York, NY Weinheim, 1999), 584 pp.
- [90] C. Peuntinger, B. Heim, C. R. Müller, C. Gabriel, C. Marquardt, and G. Leuchs, “Distribution of Squeezed States through an Atmospheric Channel”, [Physical Review Letters **113**, 060502 \(2014\)](#).
- [91] V. C. Usenko, B. Heim, C. Peuntinger, C. Wittmann, C. Marquardt, G. Leuchs, and R. Filip, “Entanglement of Gaussian states and the applicability to quantum key distribution over fading channels”, [New Journal of Physics **14**, 093048 \(2012\)](#).
- [92] C. Luo, X. Qian, W. Zhu, Q. Liu, X. Chen, Z. Xing, Z. Xu, T. Yang, and T. Yang, “Experimental study on long-distance atmospheric propagation characteristics of supercontinuum laser”, [Optics Express **33**, 44240 \(2025\)](#).
- [93] D. N. Joanes and C. A. Gill, “Comparing measures of sample skewness and kurtosis”, [Journal of the Royal Statistical Society: Series D \(The Statistician\) **47**, 183–189 \(1998\)](#).
- [94] R. K. Tyson, *Principles of Adaptive Optics*, 0th ed. (CRC Press, Nov. 18, 2015).
- [95] R. Esposito, “Power scintillations due to the wandering of the laser beam”, [Proceedings of the IEEE **55**, 1533–1534 \(1967\)](#).
- [96] J. Marcum, “A statistical theory of target detection by pulsed radar”, [IEEE Transactions on Information Theory **6**, 59–267 \(1960\)](#).
- [97] G. Vallone, D. G. Marangon, M. Canale, I. Savorgnan, D. Bacco, M. Barbieri, S. Calimani, C. Barbieri, N. Laurenti, and P. Villoresi, “Adaptive real time

- selection for quantum key distribution in lossy and turbulent free-space channels”, [Physical Review A **91**, 042320 \(2015\)](#).
- [98] M. Bohmann, A. A. Semenov, J. Sperling, and W. Vogel, “Gaussian entanglement in the turbulent atmosphere”, [Physical Review A **94**, 010302 \(2016\)](#).
- [99] N. Hosseinidehaj, Z. Babar, R. Malaney, S. X. Ng, and L. Hanzo, “Satellite-Based Continuous-Variable Quantum Communications: State-of-the-Art and a Predictive Outlook”, [IEEE Communications Surveys & Tutorials **21**, 881–919 \(2019\)](#).
- [100] J. S. Sidhu, S. K. Joshi, M. Gündoğan, T. Brougham, D. Lowndes, L. Mazzarella, M. Krutzik, S. Mohapatra, D. Dequal, G. Vallone, et al., “Advances in space quantum communications”, [IET Quantum Communication **2**, 182–217 \(2021\)](#).
- [101] F. T. Feng Tang and B. Z. Bing Zhu, “Scintillation discriminator improves free-space quantum key distribution”, [Chinese Optics Letters **11**, 090101–90104 \(2013\)](#).
- [102] R. F. Werner, “Quantum states with Einstein-Podolsky-Rosen correlations admitting a hidden-variable model”, [Physical Review A **40**, 4277–4281 \(1989\)](#).
- [103] R. Horodecki, P. Horodecki, M. Horodecki, and K. Horodecki, “Quantum entanglement”, [Reviews of Modern Physics **81**, 865–942 \(2009\)](#).
- [104] A. Einstein, B. Podolsky, and N. Rosen, “Can Quantum-Mechanical Description of Physical Reality Be Considered Complete?”, [Physical Review **47**, 777–780 \(1935\)](#).
- [105] M. Plenio and S. Virmani, “An introduction to entanglement measures”, [Quantum Information and Computation **7**, 1–51 \(2007\)](#).
- [106] E. Chitambar and G. Gour, “Quantum resource theories”, [Reviews of Modern Physics **91**, 025001 \(2019\)](#).

- [107] H. P. Yuen and V. W. S. Chan, “Noise in homodyne and heterodyne detection”, *Optics Letters* **8**, 177 (1983).
- [108] A. I. Lvovsky and M. G. Raymer, “Continuous-variable optical quantum-state tomography”, *Reviews of Modern Physics* **81**, 299–332 (2009).
- [109] S. L. Braunstein and P. Van Loock, “Quantum information with continuous variables”, *Reviews of Modern Physics* **77**, 513–577 (2005).
- [110] C. Weedbrook, S. Pirandola, R. García-Patrón, N. J. Cerf, T. C. Ralph, J. H. Shapiro, and S. Lloyd, “Gaussian quantum information”, *Reviews of Modern Physics* **84**, 621–669 (2012).
- [111] X. Yun-Jie and G. Guang-Can, “Squeezing and Entanglement in Continuous Variable Systems”, *Chinese Physics Letters* **21**, 1877–1880 (2004).
- [112] Z. Y. Ou, S. F. Pereira, H. J. Kimble, and K. C. Peng, “Realization of the Einstein-Podolsky-Rosen paradox for continuous variables”, *Physical Review Letters* **68**, 3663–3666 (1992).
- [113] A. I. Lvovsky, *Squeezed light*, (July 28, 2016) <http://arxiv.org/abs/1401.4118>, pre-published.
- [114] A. Peres, “Separability Criterion for Density Matrices”, *Physical Review Letters* **77**, 1413–1415 (1996).
- [115] R. Simon, “Peres-Horodecki Separability Criterion for Continuous Variable Systems”, *Physical Review Letters* **84**, 2726–2729 (2000).
- [116] E. Shchukin and W. Vogel, “Inseparability Criteria for Continuous Bipartite Quantum States”, *Physical Review Letters* **95**, 230502 (2005).
- [117] L. J. Ippolito, *Satellite Communications Systems Engineering: Atmospheric Effects, Satellite Link Design and System Performance*, 1st ed, New York Academy of Sciences Series (John Wiley & Sons, Incorporated, Newark, 2017), 1 p.

- [118] D. Elser, T. Bartley, B. Heim, C. Wittmann, D. Sych, and G. Leuchs, “Feasibility of free space quantum key distribution with coherent polarization states”, [New Journal of Physics **11**, 045014 \(2009\)](#).
- [119] B. Heim, D. Elser, T. Bartley, M. Sabuncu, C. Wittmann, D. Sych, C. Marquardt, and G. Leuchs, “Atmospheric channel characteristics for quantum communication with continuous polarization variables”, [Applied Physics B **98**, 635–640 \(2010\)](#).
- [120] A. A. Semenov, F. Töppel, D. Yu. Vasylyev, H. V. Gomonay, and W. Vogel, “Homodyne detection for atmosphere channels”, [Physical Review A **85**, 013826 \(2012\)](#).
- [121] X. Ma, C.-H. F. Fung, and H.-K. Lo, “Quantum key distribution with entangled photon sources”, [Physical Review A **76**, 012307 \(2007\)](#).
- [122] N. J. Beaudry, T. Moroder, and N. Lütkenhaus, “Squashing Models for Optical Measurements in Quantum Communication”, [Physical Review Letters **101**, 093601 \(2008\)](#).
- [123] T. Moroder, O. Gühne, N. Beaudry, M. Piani, and N. Lütkenhaus, “Entanglement verification with realistic measurement devices via squashing operations”, [Physical Review A **81**, 052342 \(2010\)](#).
- [124] J. F. Clauser, M. A. Horne, A. Shimony, and R. A. Holt, “Proposed Experiment to Test Local Hidden-Variable Theories”, [Physical Review Letters **23**, 880–884 \(1969\)](#).
- [125] A. A. Semenov and W. Vogel, “Entanglement transfer through the turbulent atmosphere”, [Physical Review A **81**, 023835 \(2010\)](#).
- [126] M. O. Gumberidze, A. A. Semenov, D. Vasylyev, and W. Vogel, “Bell nonlocality in the turbulent atmosphere”, [Physical Review A **94**, 053801 \(2016\)](#).
- [127] A. Fedrizzi, R. Ursin, T. Herbst, M. Nespola, R. Prevedel, T. Scheidl, F. Tiefenbacher, T. Jennewein, and A. Zeilinger, “High-fidelity transmission of

- entanglement over a high-loss free-space channel”, [Nature Physics](#) **5**, 389–392 (2009).
- [128] Z. Yan, Y. Liu, J. Yan, and X. Jia, “Deterministically entangling multiple remote quantum memories inside an optical cavity”, [Physical Review A](#) **97**, 013856 (2018).
 - [129] L. Ma, X. Lei, J. Yan, R. Li, T. Chai, Z. Yan, X. Jia, C. Xie, and K. Peng, “High-performance cavity-enhanced quantum memory with warm atomic cell”, [Nature Communications](#) **13**, 2368 (2022).
 - [130] W. Ge, K. Jacobs, S. Asiri, M. Foss-Feig, and M. S. Zubairy, “Operational resource theory of nonclassicality via quantum metrology”, [Physical Review Research](#) **2**, 023400 (2020).
 - [131] J. Sperling, W. Vogel, and G. S. Agarwal, “Sub-Binomial Light”, [Physical Review Letters](#) **109**, 093601 (2012).
 - [132] V. S. Kovtoniuk, E. V. Stolyarov, O. V. Kliushnichenko, and A. A. Semenov, “Tight inequalities for nonclassicality of measurement statistics”, [Physical Review A](#) **109**, 053710 (2024).
 - [133] H. Paul, P. Törmä, T. Kiss, and I. Jex, “Photon Chopping: New Way to Measure the Quantum State of Light”, [Physical Review Letters](#) **76**, 2464–2467 (1996).
 - [134] S. A. Castelletto, I. P. Degiovanni, V. Schettini, and A. L. Migdall, “Reduced deadtime and higher rate photon-counting detection using a multiplexed detector array”, [Journal of Modern Optics](#) **54**, 337–352 (2007).
 - [135] J. Sperling, W. Vogel, and G. S. Agarwal, “True photocounting statistics of multiple on-off detectors”, [Physical Review A](#) **85**, 023820 (2012).
 - [136] A. A. Semenov and A. B. Klimov, “Dual form of the phase-space classical simulation problem in quantum optics”, [New Journal of Physics](#) **23**, 123046 (2021).

Appendix A. List of publications, conferences and scientific meetings

List of publications

- [I] M. Klen and A. A. Semenov, "Numerical simulations of atmospheric quantum channels", [Phys. Rev. A 108, 033718 \(2023\)](#). (Q1)
- [II] M. Klen, D. Vasylyev, W. Vogel, and A. A. Semenov, "Time correlations in atmospheric quantum channels", [Phys. Rev. A 109, 033712 \(2024\)](#). (Q1)
- [III] I. Pechonkin, M. Klen, and A. A. Semenov, "Circular-beam approximation for quantum channels in a turbulent atmosphere", [Phys. Rev. A 112, 063716 \(2025\)](#). (Q1)
- [IV] A. Semenov, M. Klen, and I. Pechonkin, "Quantum Optics in the Turbulent Atmosphere: Fundamental Issues and Applications", in Quantum Technologies for Defence and Security II, edited by V. Fernandez, G. Sorelli, and S. Schwartz (p. 38). [Proc. SPIE 13676, 136760H-13 \(2025\)](#).

Conferences and scientific meetings

1. M. Klen and A. A. Semenov, "Free-space quantum channels: Numerical simulations", US-Ukraine Quantum Forum 2023, August 28-31, 2023
2. M. Klen, "Quantum light in atmospheric turbulence", 25th Symposium on photonics and optics SPO 2024, Kyiv, (Ukraine), November 8, 2024
3. M. Klen, "Numerical simulations in free-space quantum channels", Poster session at Quantum 2025: From Foundations of Quantum Mechanics to Quantum Information and Quantum Metrology & Sensing, Turin, (Italy), May 18-24, 2025
4. A. Semenov, M. Klen, I. Pechonkin, "Quantum optics in the turbulent atmosphere: fundamental issues and applications": invited talk at the SPIE Sensors+Imaging Meeting. Quantum Technologies for Defense and Security II. Madrid, Spain. September 15–18, 2025.